Advanced Neutron Imaging and Sensing

JAROSLAV ŘEHÁČEK[a], ZDENEK HRADIL[a], JAN PEŘINA[a], SAVERIO PASCAZIO[b], PAOLO FACCHI[c], AND MICHAEL ZAWISKY[d]

[a]*Department of Optics, Palacky University, 17. listopadu 50, 77200 Olomouc, Czech Republic*

[b]*Dipartimento di Fisica, Università di Bari, and Istituto Nazionale di Fisica Nucleare, Sezione di Bari, I-70126 Bari, Italy*

[c]*Dipartimento di Matematica, Università di Bari, and Istituto Nazionale di Fisica Nucleare, Sezione di Bari, I-70126 Bari, Italy*

[d]*Atominstitut der Österreichischen Universitäten, Stadionallee 2, A-1020 Wien, Austria*

ISSN 1076-5670/05
DOI: 10.1016/S1076-5670(05)42002-9

I. INTRODUCTION

Various physical phenomena are similar to such an extent that their mathematical description is alike. This elementary truth is demonstrated in many fields of physical research, and cross-fertilization is a powerful tool of contemporary physics. Remarkably, quantum mechanics, developed at the beginning of the 20th century, has proven that particles may behave like waves. Electromagnetic waves associated with the propagation of light can be described by the wave equation, whereas matter waves, associated with moving particles,

are governed by Schrödinger wave equation. Therefore, both phenomena can be treated within a similar optical framework. This is also the case with neutrons—neutral particles discovered in 1932 by J. Chadwick. Although their internal structure is complicated, at a first approximation they can be seen as massive particles, almost noninteracting with their neighborhood at a distance. Often, the interaction of neutrons with matter can be described by effectively introducing some phenomenological parameters such as the indexes of refraction and absorption. This establishes a full analogy with geometric and wave optics, including polarization effects, provided the spin of the neutron is not neglected. The area of neutron physics in which such an "optical" approximation holds is called *neutron optics*. Concerning imaging and other precise measurements, neutrons have many advantages over light quanta—photons. For example, common neutron detectors have very high intrinsic quantum efficiencies—more than 99%. Moreover, neutrons can be literally counted one by one, something that is not possible with commercial single-photon detectors.

Unlike photons or electrons, neutrons interact with matter through all four basic physical interactions. In particular, they are subject to the strong interaction, thus making it possible to distinguish between different isotopes of the same element. In addition to possessing well-defined particle attributes such as a nonvanishing mass, "size," and magnetic moment, neutrons, as quantum theory predicts, also show wave behavior, governed by their de Broglie wavelength. For all these reasons, neutrons are suitable tools not only for imaging and precise measurements, but also for fundamental experiments aimed at testing the predictions of the quantum theory, such as the wave-particle duality, the projection postulates, topological phases, and other effects.

Compared with available light sources, neutrons have certain disadvantages. The absence of strong coherent sources of neutrons with intensities comparable to lasers in optics is the main distinction that should be mentioned. Coherent beams are usually generated by spectral filtering of thermal beams provided by fission reactors. Because intensities of thermal neutron beams are already rather low, the detected signals typically have a much worse signal-to-noise ratio than the corresponding optical signals. Therefore in neutron optics it is particularly important to propose methods capable of extracting as much information as possible from the detected noisy data.

The purpose of this chapter is twofold. One goal is to present some minimal theoretical tools necessary for the understanding of the subtle and fundamental effects associated with neutrons optics and reported in the recent literature. The second goal is to provide an up-to-date overview of the neutrons experiments that reveal the quantum mechanical nature of neutrons. For this reason, several neutron optical measurement techniques are discussed.

This chapter is composed of two parts. The first part is addressed to readers who are not familiar with the subject. Section II reviews some basic concepts of experimental interferometry, Section III introduces some notions of neutron optics. The second part is somewhat more specialized and deals with applications and measurement techniques. Section IV starts with the simple one-parameter phase measurement. Section V discusses transmission tomography, and phase tomography (at very low intensities) in the subject of Section VI. Three-beam interference and which-way information are analyzed in Section VII. Section VIII introduces a novel tomographic method based on the quantum Zeno effect, and Section IX investigates the sensitivity to fluctuation and the onset to decoherence. Section X concludes with a sophisticated full-quantum tomographic method for neutron wave packets. Section XI provides a summary. Throughout the entire chapter, attention is directed to the wave-particle duality and decoherence in neutron interferometry, as well as to the utilization of quantum effects for improving classical imaging.

II. Neutron Optics: Experimental Interferometry

Neutron optics covers a wide field of applications in which the full exploitation of beam coherence yields the high sensitivity of neutron optical devices. The following sections present a short introduction to neutron optics, focusing on thermal neutron beams and perfect-crystal interferometry. In addition, we include some preparatory details and close with an outlook of further improvements and future applications of this extremely sensitive technique.

A. Beam Preparation

Neutron beams are primarily produced in fission processes with an initial energy of approximately 2 MeV. Then they are successively slowed down by collision processes, and after about 20 collisions the neutrons reach thermal energies ($\approx$25 meV, which corresponds to a de Broglie wavelength of $\lambda = 0.18$ nm). Then, on average, they experience another 500 collisions until they leave the moderator and enter the beam guide. The energy distribution can be assumed to be Maxwellian until wavelength selection by the crystals. After Bragg reflection at the perfect-crystal monochromator, and Laue transmissions through the interferometer lamellas, the remaining quasi-monochromatic momentum distribution can be approximated by an overlap of Gaussian distributions with $\delta k/k \leq 10^{-2}$ (Rauch and Werner, 2000a; Baron, 2005).

B. Neutron Interactions in Matter and Fields

The dominant neutron interaction is the short-range ($R < 2$ fm) nuclear interaction, contributions of long-range interactions with nonmagnetic substances below 1%. In interferometry experiments, only forward scattering is relevant, which directly relates to the bound coherent scattering length b_c. It is a phenomenological constant that defines the strength of the optical potential,

$$\overline{V} = \frac{2\pi\hbar^2}{m} b_c N, \tag{1}$$

with N the number of nuclei per unit volume. Most isotopes have a positive coherent scattering length, but some are known with a negative b_c. It is defined positive for repulsive optical potentials $\overline{V} > 0$, with an index of refraction smaller than unity, and negative for weak attractive potentials without bound states. An important quantity in neutron optics is the index of refraction for neutrons moving through a mean optical potential $\overline{V}$ (Goldberger and Seitz, 1947):

$$n = \sqrt{1 - \frac{\overline{V}}{E}} \cong 1 - \frac{\lambda^2 N}{2\pi} \sqrt{{b_c}^2 - \left(\frac{\sigma_r}{2\lambda}\right)^2} + i\frac{\sigma_r N \lambda}{4\pi}, \tag{2}$$

where E and λ denote the neutron energy and wavelength, which are associated by the dispersion relation $k = \sqrt{\frac{2mE}{\hbar^2}}$, and σ_r is the reaction cross section, the sum of the absorption (σ_a) and scattering (σ_s) cross sections. The elements σ_a, σ_s, and b_c are well known for most isotopes (Sears, 1992). The reaction cross section determines the beam attenuation, which can be approximated by an exponential law, if it is assumed that a quasi-monochromatic well-collimated beam with intensity I_0 transmits a thin target of thickness d,

$$\bar{I} = \bar{I}_0 \exp\left(-\sum_i (\sigma_r N)_i d\right). \tag{3}$$

The product $\Sigma_i = (\sigma_r N)_i$ is called the macroscopic cross section of the i-th isotope. According to the definition of the index of refraction, the phase shift is a complex quantity:

$$\Phi = k(1-n)d = \Phi_r + i\Phi_i, \tag{4}$$

but for thermal neutrons ($E \gg \overline{V}$) and low-absorbing materials, the imaginary phase is negligible. In a mixture of m isotopes the total phase shift is as follows:

$$\Phi_{\text{nuc}} = -\sum_{i=1}^{m} \lambda (N b_c)_i d. \tag{5}$$

Due to their magnetic moment, neutrons experience a strong interaction in magnetic fields (Badurek *et al.*, 1976) which, for magnetic materials, is comparable with the nuclear interaction:

$$\Phi_{\text{mag}} = -\frac{\boldsymbol{\sigma} \cdot \boldsymbol{\alpha}}{2}, \quad \boldsymbol{\alpha} = -\frac{2\mu \widehat{B}}{\hbar v} \int B \, ds. \tag{6}$$

Here $\boldsymbol{\sigma}$ represents the Pauli spin vector, $\boldsymbol{\alpha}$ the spin rotation vector around the orientation of magnetic induction $\widehat{B}$, v the neutron velocity, and μ the magnetic neutron moment. A neutron moving in an electric field E along path l experiences a weak effective magnetic field, which creates a small phase shift (Cimmino *et al.*, 1989):

$$\Phi_{\text{el}} = \pm \frac{2\mu}{\hbar c} El. \tag{7}$$

The area A, enclosed by an interferometer loop, relates directly to the sensitivity for gravity investigations (Colella *et al.*, 1975):

$$\Phi_{\text{grav}} = -\frac{2\pi m_i m_g g A \lambda}{h^2} \sin \phi, \tag{8}$$

where m_i and m_g are the neutron inertial and gravitational mass and ϕ describes the crystal tilt from the horizontal plane.

C. *Perfect-Crystal Neutron Interferometry*

In a monolithic perfect-crystal interferometer, invented by Bonse and Hart (1965) for X-rays, and by Rauch *et al.* (1974) for neutrons, all silicon nuclei are perfectly aligned, leading to a well-defined potential in the whole interferometer (Windisch and Becker, 1990). The world's largest interferometer has the following characteristics (Zawisky *et al.*, 2002):

Path length	21 cm
Macroscopic beam separation	5 cm–15 cm
Number of unit cells	4.2×10^{24}

The dynamic diffraction of thermal neutrons in a perfect-crystal lattice is described within the Schrödinger theory (Sears, 1989; Rauch and Petraschek, 1976, 1978; Petraschek and Rauch, 1976), where the neutron energy E is a constant of motion:

$$\left[-\frac{\hbar^2}{2m} \Delta + V(\mathbf{r}) - E \right] \Psi(\mathbf{r}) = 0. \tag{9}$$

The lattice potential is given in first Born approximation by the Fermi pseudo-potential where $\mathbf{r}_j$'s describe the positions of the scattering nuclei:

$$V(\mathbf{r}) = \frac{2\pi\hbar^2 b_c}{m} \sum_j \delta(\mathbf{r} - \mathbf{r}_j). \tag{10}$$

In the reciprocal lattice, the potential reads:

$$V(\mathbf{q}) = \frac{2\pi\hbar^2 b_c}{m N_z V_z} \sum_j e^{-i\mathbf{q}\cdot\mathbf{R}_j} \sum_i e^{-i\mathbf{q}\cdot\mathbf{a}_i}, \tag{11}$$

where $\mathbf{R}_j$ denotes the position of cell j, $\mathbf{a}_i$ the position of nucleus i in the cell, N_z the number of unit cells, and V_z the volume of the unit cell. The first lattice factor is nonvanishing only if the momentum transfer $\mathbf{q}$ equals a reciprocal lattice vector $\mathbf{G} = h\mathbf{g}_1 + k\mathbf{g}_2 + l\mathbf{g}_3$ with Miller indexes (hkl)

$$\frac{1}{N_z} \sum_j e^{-i\mathbf{q}\cdot\mathbf{R}_j} = 1 \quad \text{if } \mathbf{q} = \mathbf{G} \quad (= 0 \text{ otherwise}). \tag{12}$$

The second factor in Eq. (11) is called a *structure factor* because it depends on the crystal structure:

$$F = \sum_i e^{-\mathbf{q}\cdot\mathbf{a}_i} = 8 \quad \text{for } h + k + l = 0, 4, 8, 12, \ldots. \tag{13}$$

The resulting optical potential is very weak compared to the neutron energy. For example,

$$V(\mathbf{220}) = 5.2 \times 10^{-8} \text{ eV}, \qquad \frac{V}{E} = 2 \times 10^{-6}. \tag{14}$$

If a crystal plate is rotated around so that the incident angle γ approaches the Bragg angle θ_B, then two diffracted beams $\Psi_{O,H}$ are observed (Figure 1). The partial states $\Psi_{I,O(H)}$ and $\Psi_{II,O(H)}$ in the interferometer are determined by the transmission and reflection amplitudes t, r and the accumulated phases (Figure 2):

$$\Psi_O = \Psi_{I,O} + \Psi_{II,O} = (trr + rrt) e^{-i\frac{2\pi y}{\Delta_0}(z_M - z_S)} \Psi_i. \tag{15}$$

Coefficients $r(y)$, $t(y)$ are in general different and depend on the deviation parameter, $y \propto (\theta_B - \gamma)$, of the incoming beam from the Bragg condition; Δ_0 is a characteristic parameter in crystal diffraction. The ideal crystal interferometer has to fulfill several criteria (Bauspiess *et al.*, 1978) as follow:

- Distortion-free crystal with constant lattice spacing

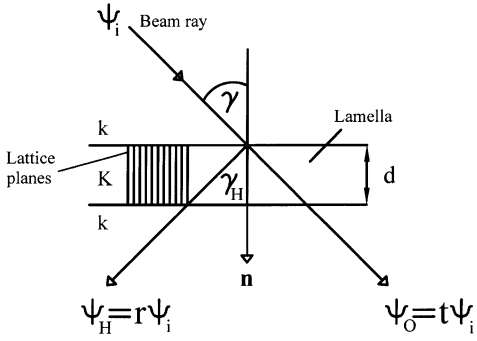

FIGURE 1. Generation of two coherent beams in a perfect-crystal beamsplitter when γ approaches the Bragg angle (Laue transmission).

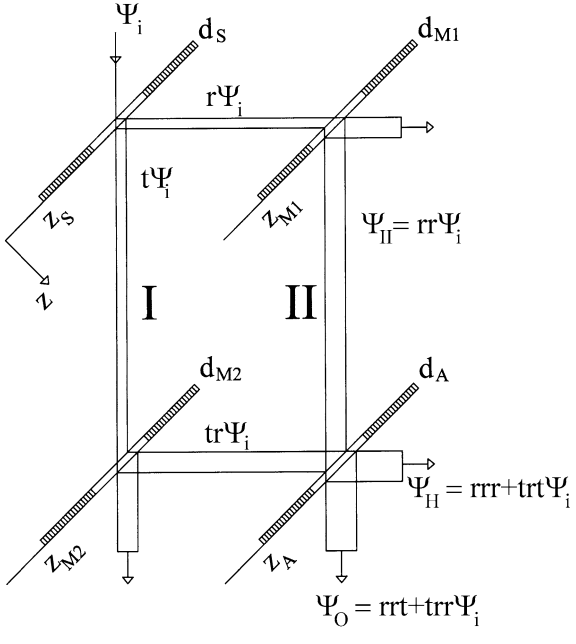

FIGURE 2. A one-loop perfect-crystal interferometer of the Mach–Zehnder type.

- $d_S = d_{M1} = d_{M2} = d_A$ (S = Splitter, M = Mirror, A = Analyzer), $z_A - z_{M2} = z_{M1} - z_S$
- Geometric tolerances ≤ 3 μm
- Position stability of the lattice about 0.01 nm; vibration level below 10^{-4} g
- Angular stability of the Bragg axis: $\delta\gamma \leq 10^{-3}$ arc sec

- Tilt of the lattice planes against each other: $\delta\rho \leq 10^{-3}$ arc sec
- Thermal gradients in the crystal of 10^{-3} K/cm cause a lattice inclination of 5×10^{-4} arc sec/cm.

In an ideal interferometer, after superposition of two monochromatic states with phase difference $\Phi = \Phi_I - \Phi_{II}$, the mean count number at output O reads:

$$\overline{N}_O(\Phi) = \overline{N}_i \left| trr\left(e^{-i\Phi_I} + e^{-i\Phi_{II}}\right)\right|^2 = \overline{N}_O(1 + \cos\Phi). \tag{16}$$

An auxiliary phase shifter creates discrete phase shifts Δ_j, $j = 1, \ldots, m$ ($m \geq 2$), which serve as reference for the measurement of the unknown phase Φ. The neutron number oscillates between the two output ports O and H as a function of Δ_j. In practice, perfect interference cannot be realized; thus, the model must be extended by an additional parameter, the visibility V:

$$\overline{N}_{j,O}(\Phi) = \overline{N}_O\left[1 + V_O \cos(\Delta_j + \Phi)\right], \tag{17}$$

$$\overline{N}_{j,H}(\Phi) = \overline{N}_H\left[1 - V_H \cos(\Delta_j + \Phi)\right], \tag{18}$$

$$\overline{N}_O V_O = \overline{N}_H V_H. \tag{19}$$

The reference phases can continuously be tuned by the rotation angle ε of the phase shifter. In the standard configuration, the phase plate is placed in both beams, nearly parallel to the interferometer lamellas:

$$\Delta_j(\varepsilon_j) = -\lambda N b_c d_{ps}\left(\frac{1}{\cos(\theta_B - \varepsilon_j)} - \frac{1}{\cos(\theta_B + \varepsilon_j)}\right) \cong \text{const} \times j, \tag{20}$$

where d_{ps} denotes the thickness of the phase shifter. Typical intensities at the Vienna Atominstitute interferometer instrument are $\overline{N}_O \approx 1$ n/s and $\overline{N}_H \approx 2$ n/s. The typical "passage time" through the interferometer is 0.05 ms, thus, in a mechanical picture, one would conclude that the interferometer is 99.99% of the measurement time "empty." But in the case of a stationary source $|\Psi|^2 > 0$ is always fulfilled and the interferometer is never empty. V_H is approximately half of V_O because $\Psi_{I,H}$ and $\Psi_{II,H}$ have different amplitudes. The visibility is affected by several factors, for example: temperature gradients in the crystal lattice, geometric errors, crystal strains, lattice vibrations, gradients in the lattice spacing caused by impurities, dephasing due to thickness (δd) and density (δN) fluctuations in the sample and due to the spectral width (δk), or caused by an asymmetric intensity ($\overline{N}_I \neq \overline{N}_{II}$) of the interfering beams. When considering only the beam and interferometer characteristics, and by assuming Gaussian approximations for the different effects, the following expression is obtained for the visibility

(Rauch and Werner, 2000a):

$$V = \frac{2\sqrt{\overline{N}_I \overline{N}_{II}}}{\overline{N}_I + \overline{N}_{II}} \exp\left\{ -\frac{(\Delta\delta k)^2}{2} - \left[\left(\frac{\delta d}{d_0} \right)^2 + \left(\frac{\delta N}{N_0} \right)^2 \right] \frac{(\Delta k_0)^2}{2} \right\}, \quad (21)$$

where Δ describes the translation of one partial wave relative to the other (e.g., induced by a phase shifter with thickness d):

$$\Delta = \frac{N b_c \lambda^2 d}{2\pi}. \quad (22)$$

D. Interferometer Design

Since 1974 several types of silicon perfect-crystal interferometers have been prepared at the Vienna Atominstitute, the first interferometers cut from 3-inch ingots (effective diameter 79 mm), but now 4-inch (effective 102 mm) dislocation-free ingots are available, which allowed for the preparation of larger crystals (Figure 3). A new 45-degree design, fabricated from a [100]-oriented 4-inch ingot, offers several advantages compared to conventional geometries (Zawisky *et al.*, 2002). Here the beams are traveling parallel to the crystal axis, which enables the preparation of arbitrarily large interferometers. The usable beam separation is larger than in previous designs, which offers ample interferometer space and increases its sensitivity. The manufacturing of perfect-crystal neutron interferometers requires several crucial preparatory measures as below:

- **Selecting the ingot**. Dislocation-free float-zone ingots with high purity, diameters between 10 and 20 cm, and lengths up to 100 cm, are actually available in interferometer quality. Silicon crystallizes in the cubic diamond lattice. Point-defects cannot be avoided during crystal growth, but they cause only small intrinsic dislocation loops without far-reaching lattice distortions.
- **Lattice orientation** with a Laue back-reflection camera (accuracy $\approx$ 0.1 degree) or an X-ray diffractometer ($\approx$2 arc sec).
- **Cutting the lamellas**. The interferometer lamellas are cut with a bronze-bonded diamond cutting wheel of a surface-grinding machine.
- **Etching**. The damaged crystal surface must be removed by etching in a $HF : HNO_3$ acid bath. An originally flat surface will show a slight convex shape after etching, which causes small phase variations across the illuminated crystal areas.
- **Geometric measuring**. The overall geometry must be determined at a coordinate measuring machine with a geometric resolution of about 0.1 μm (Figure 4). If the geometry does not fulfill the quality standards, the lamellas must be recut in a fine-grinding procedure.

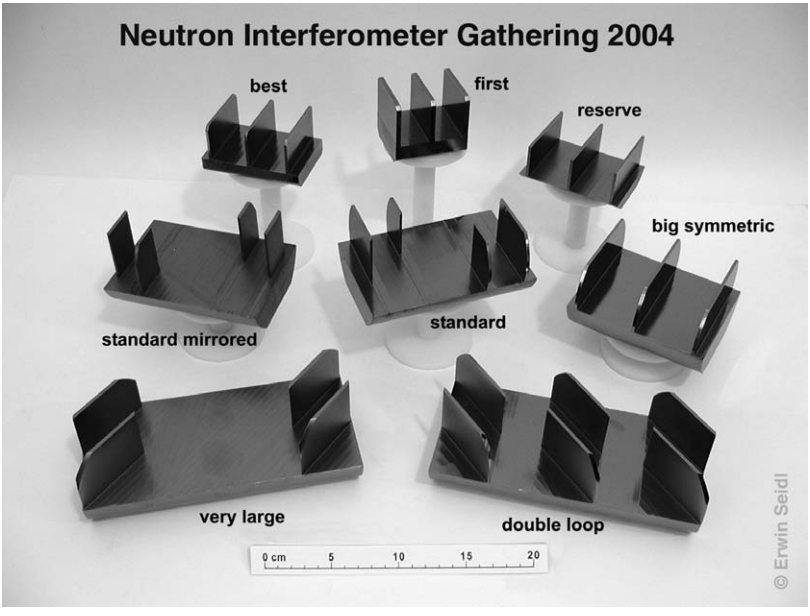

FIGURE 3. Set of perfect-crystal neutron interferometers prepared at the Vienna Atominstitute. The interferometers in the last row are machined from a 3-inch ingot; the others from 4-inch ingots. The two interferometers in front represent the new generation of large-scale 45-degree interferometers with greatly increased space and sensitivity. Photograph by Erwin Seidel.

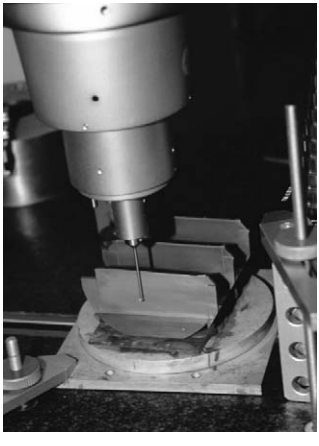

FIGURE 4. Geometric measuring on a large three-plate neutron interferometer.

E. Fundamental Aspects of Neutron Interferometry

We want to emphasize certain aspects of perfect-crystal neutron interferometry, which are to some extent exceptional in matter-wave interferometry and/or in light optics:

- Neutrons possess well-defined elementary *particle properties* (quark structure with internal charge distribution and magnetic moment, mass, spin, limited lifetime), but as long as interference is observed, they must be described as "nonlocal" states (*wave property*).
- The phase space density, the mean occupation number in the coherence volume, is of the order of 10^{-18} at the Vienna Atominstitute. The typical coherence volume in neutron interferometry is 5 nm (vertical) $\times$ 10 nm (longitudinal) $\times$ 5000 nm (transversal), where the large transverse coherence length, parallel to the reciprocal lattice vector, is caused by strong wavelength filtering in the crystal lamellas. Quantum statistical effects such as anti-bunching are completely negligible at such low occupation numbers. This supports the interpretation of our experiments as *one-particle self-interference*.
- The independent stochastic detection events have been proven to follow *Poissonian statistics*.
- The very low energy of thermal neutrons enables a completely *nonrelativistic description* using Schrödinger's equation.
- Perfect-crystal beamsplitters create large angular beam separations. The coherence is conserved over macroscopic distances in the monolithic interferometer. The ratio of maximum beam separation (15 cm) and de Broglie wavelength actually reaches 10^9.
- In the pure-silicon crystal and phase shifters, no essential absorption exists. The neutron numbers are conserved because the neutron decay of about 15 min is completely negligible compared to the "passage time" of 50 μs. Thus, the neutron's evolution through the interferometer is determined by controlled *unitary transformations* until detection behind the interferometer.
- Single neutrons are detectable with probability better than 0.98 using gas detectors. Because the typical count rates are of the order of a few neutrons per second, and considering the detector's time resolution of a few microseconds, the *probability that two neutrons are detected simultaneously is practically zero*.
- All phase shifts can smoothly and to arbitrary accuracy be varied by rotating a phase-shifter plate. The phase shifter(s), when operating in the near-parallel position in both beams, introduce *no essential dephasing* to the experiments.

- Neutrons can easily be shielded from parasitic environmental interactions.
- With a two-loop interferometer, the *wave-particle duality can simultaneously be measured* without disturbing the neutron state.

F. Further Instrumental Improvements and Future Topics in Perfect-Crystal Neutron Interferometry

Since the prices for hyperpure distortion-free silicon ingots are quite reasonable (≈1 Eur/g), this allows considerable freedom to optimally adapt the interferometer geometry to the experimental demands. Recently a thin-plate interferometer optimized for neutron phase-contrast tomography has been machined with only 0.5 mm thick lamellas, and even thinner interferometer plates can be prepared if a tomographic resolution beyond 50 μm is desired. Here not the crystal preparation but the weak intensity of coherent neutron beams is the ultimate limiting factor for the full exploitation of interferometric phase tomography (Zawisky *et al.*, 2004a).

Another main topic of the Vienna institute is the preparation of large-scale interferometers to extend the applications of thermal neutron interferometry. With the new 45-degree design (Figure 5), we can use much larger samples and more beam manipulators, and the dramatically increased interferometer area makes the instrument extremely sensitive to gravitational effects on single-quantum states. Due to the large beam separation the neutrons will be the lightest quantum objects for fundamental studies on gravitation-induced phases.

The recently developed large-scale two-loop interferometer offers completely new measurement techniques, for example, the simultaneous and

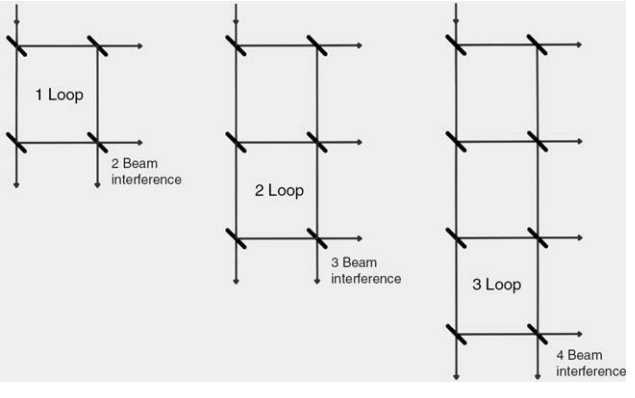

FIGURE 5. Design of *n*-loop neutron interferometers using 45-degree beamsplitters.

distortion-free measurement of duality (Zawisky, 2004), the complete measurement of the coherence features of the neutron beam, and geometric phase experiments (Rauch, 2004). Interestingly, the interference of nonlocal neutron states can also be used in the two-loop interferometer for the measurement of the neutron's intrinsic charge radius, which certainly is a pure-particle property (Ioffe and Vrana, 2002). In principle, the number of loops can further be extended be inserting more beamsplitters (see Figure 5), thereby increasing the interfering intensity and the phase sensitivity.

III. Neutron Optics: Basic Concepts

A. *Wave Equations and Quantization*

Let us briefly review some basic notions of quantum mechanics, which provides the mathematical basis for neutron optics. The time evolution of the wave function $\psi(x)$ for a free massive particle is governed by the Schrödinger equation:

$$i\hbar\frac{\partial}{\partial t}\psi(\mathbf{x},t) = -\frac{\hbar^2}{2m}\Delta\psi(\mathbf{x},t). \tag{23}$$

The modulus of the wave function $|\psi(\mathbf{x},t)|^2$ represents the probability density of finding a particle at a given position and time, and Δ is the Laplace operator. Analogously, in scalar wave optics, the propagating wave is described by the complex amplitude $U(\mathbf{x},t)$ and the wave equation

$$\Delta U(\mathbf{x},t) - \frac{1}{c^2}\frac{\partial^2}{\partial t^2}U(\mathbf{x},t) = 0, \tag{24}$$

where c denotes the phase speed of the light. Resorting to the Fourier components in the time domain, both equations will yield the same generic form of Helmholtz wave equation:

$$\Delta A(\mathbf{x}) + k^2 A(\mathbf{x}) = 0, \tag{25}$$

where the signal A equals ψ or U, respectively. In the former case of matter waves, $k^2 = \frac{2m\omega}{\hbar}$, whereas in the latter case of light field, $k^2 = \frac{\omega^2}{c^2}$. This establishes the full analogy between matter-wave and light optics. In the case of propagation of a signal in a medium with refractive index n, the wave vector k^2 should be replaced by k^2n^2.

Besides the Schrödinger picture based on the wave functions (quantum states), quantum mechanics allows formulation of all laws in a fashion closely related to classical mechanics. Such framework is known as the *Heisenberg picture*. All the measurable quantities are associated with operators, namely,

the Hamiltonian $\widehat{H}$, which represents energy, and the position $\hat{x}$ and impulse $\hat{p}$ operators. In the language of quantum mechanics, the wave equations can be treated as an operator form of the nonrelativistic dispersion relation for massive particles $E = \frac{p^2}{2m}$ and (relativistic) massless photons $E = pc$, under the correspondence $E \rightarrow i\hbar\frac{\partial}{\partial t}$ and $\mathbf{p} \rightarrow \hat{p} = -i\hbar\nabla$. The operators $\hat{x}$ and $\hat{p}$ are well defined in nonrelativistic quantum mechanics describing the position and impulse of the particle, whose state is described by the wave function. Particularly, the case of free propagation is governed by the same law as classical mechanics since

$$\hat{x}(t) = e^{-i\widehat{H}t/\hbar}\hat{x}(t=0)e^{-i\widehat{H}t/\hbar} = \hat{x}(0) + \frac{t}{m}\hat{p}(0). \tag{26}$$

Notice, however, that such a formulation is merely formal for light, since due to the special theory of relativity the particles moving with the speed of light cannot be localized.

The formalism of quantum mechanics is very efficient for description of interference experiments. The notion of *wave* is associated with complex amplitude-carrying information about *phase*. For this purpose, the non-Hermitian annihilation operator may be introduced as the combination of position and impulse operators:

$$\hat{a} = \hat{x} + i\,\hat{p}. \tag{27}$$

Indeed, the eigenvectors of this operator are known as *coherent states*, the closest analogues of classical states with well-defined amplitude and phase. Although the annihilation operator may always be defined according to the formal relation in Eq. (27), the physical meaning differs for light and neutrons. In the former case, operators $\hat{x}$ and $\hat{p}$ usually represent the quadrature components of the electromagnetic field. The corresponding annihilation operator $\hat{a}$ defines the operator of photon number $\hat{n} = \hat{a}^\dagger\hat{a}$, whose eigenvalues can be literally interpreted as the number of photons. This is, of course, a conserved quantity in the free electromagnetic field. The situation is diametrically different in the case of the neutron, where the operators $\hat{x}$, $\hat{p}$ represent the position and impulse of the neutron as a moving particle. In that case, the operator $\hat{a}^\dagger\hat{a}$ does not represent the number operator (there is always one neutron interfering with itself), but rather an operator characterizing the space distribution of neutron in the phase space. This description is analogous to, for example, the mode index of Laguerre–Gauss beams in optics.

B. Phase Measurements

Phases associated with wave aspect of neutrons play an important role in neutron optics. Phase measurements are among the most sensitive measure-

ments available. Many other physical quantities, for example, the distance of propagation, strength of magnetic fields, or density, alter phase and can thus be accurately determined by measuring the phase. This can be done by placing the sample in one arm of an interferometer whose other arm serves as a reference. The difference of phases accumulated in the two arms can then be inferred from the intensity changes at the interferometer outputs. Since neutron interferometers are typically operated with low-intensity beams, attention must be paid to the correct interpretation of the phase at a single-particle level. Let us first recall the concept of quantum phase in optics.

1. *Quantum Phase*

The phase of optical fields plays a decisive role in many optical phenomena, particularly in interference and diffraction of light. However, when the intensity of light is decreased at a quantum level, the classical notion of phase loses its meaning and complications occur in order to provide a sensible definition at a quantum level.

The phase operator $\hat{\varphi}$ has been introduced by Dirac (see Heitler, 1954; Akhiezer and Berestetsky, 1965) in analogy to the classical procedure of introducing the phase by the polar decomposition of the annihilation operator,

$$\hat{a} = \exp(i\hat{\varphi})\hat{n}^{1/2}, \tag{28}$$

where $\hat{n}$ is the number operator $\hat{a}^{\dagger}\hat{a}$. Assuming that $\hat{\varphi}$ may be a Hermitian operator (then $\exp(i\hat{\varphi})$ is unitary) and using the commutation rules

$$\left[\exp(i\hat{\varphi}), \hat{n}\right] = \exp(i\hat{\varphi}),$$

and

$$[\hat{\varphi}, \hat{n}] = -i\hat{1},$$

it follows that

$$\left\langle (\Delta\hat{n})^2 \right\rangle \left\langle (\Delta\hat{\varphi})^2 \right\rangle \geq \frac{1}{4}. \tag{29}$$

However, a difficulty arises from the fact that the operator $\widehat{U} = \exp(i\hat{\varphi})$ is not unitary, since $\widehat{U}\hat{n}\widehat{U}^{\dagger} = \hat{n} + \hat{1}$. To avoid this difficulty, Susskind and Glogower defined, see example review (Carruthers and Nieto, 1968), two Hermitian operators:

$$\widehat{C} = \frac{1}{2}\left(\widehat{U} + \widehat{U}^{\dagger}\right) \quad \text{and} \quad \widehat{S} = \frac{1}{2i}\left(\widehat{U} - \widehat{U}^{\dagger}\right) \tag{30}$$

fulfilling the commutation rules

$$[\widehat{C}, \hat{n}] = i\widehat{S} \quad \text{and} \quad [\widehat{S}, \hat{n}] = -i\widehat{C}, \tag{31}$$

and consequently

$$\left\langle (\Delta\hat{n})^2 \right\rangle \left\langle (\Delta\widehat{C})^2 \right\rangle \geq \frac{\langle \widehat{S} \rangle^2}{4},$$
$$\left\langle (\Delta\hat{n})^2 \right\rangle \left\langle (\Delta\widehat{S})^2 \right\rangle \geq \frac{\langle \widehat{C} \rangle^2}{4}. \tag{32}$$

It is more convenient to define

$$\widehat{U} = (\hat{n}+1)^{-1/2}\hat{a}, \qquad \widehat{U}^{\dagger} = \hat{a}^{\dagger}(\hat{n}+1)^{-1/2}, \tag{33}$$

for which

$$\widehat{U}\widehat{U}^{\dagger} = \hat{1}, \qquad \widehat{U}^{\dagger}\widehat{U} = \hat{1} - |0\rangle\langle 0|, \tag{34}$$

which means that the unitary properties can be satisfied by antinormal ordering of the operators $\widehat{U}$ and $\widehat{U}^{\dagger}$.

From Eq. (32), a more general uncertainty relation is obtained (see the review in Lukš and Peřinová, 1994 and references therein):

$$\left[\left\langle (\Delta\hat{n})^2 \right\rangle + \frac{1}{4} \right] V \geq \frac{1}{4}, \tag{35}$$

where the phase dispersion equals $V = D^2 = 1 - \langle \widehat{C} \rangle^2 - \langle \widehat{S} \rangle^2 = 1 - |\langle \exp(i\hat{\varphi}) \rangle|^2$. It should be noted that the inequality in Eq. (35) is more fundamental and replaces the inequality in Eq. (29), which is valid in most practical cases, but not without exception. Inequality in Eq. (35) has important physical consequences. The operator representation of physical quantities in quantum theory necessary for the discussion of spontaneous effects leads to the occurrence of (1) statistics and (2) inequalities leading to the complementarity of the observation of ideal-wave or particle phenomena as exhibitions of wave-particle duality, experimentally well verified for photons, electrons, neutrons, atoms, and ions. Consider an interferometer with single photons where one cannot distinguish to which arm of the interferometer a photon belongs. Then there is uncertainty in the photon number n and ideal interference fringes (with maximum visibility) may be observed if the phase is quite certain (i.e., $V = 0$), which means that the phase has a certain value $\bar{\varphi}$ with the phase probability distribution $P(\varphi) = \delta(\varphi - \bar{\varphi})$. Therefore Eq. (35) demands $\langle (\Delta\hat{n})^2 \rangle \to \infty$. Next, we try to determine during the measurement to which arm the photon belongs. If we are successful, we specify the Fock state $|1\rangle$ and $\langle (\Delta\hat{n})^2 \rangle = 0$. In this case, Eq. (35) leads to $V \geq 1$ and hence $V = 1$, $P(\varphi) = 1/2\pi$, that is, the phase is quite uncertain over the interval $(0, 2\pi)$ and $\langle \exp(i\hat{\varphi}) \rangle = 0$. Thus, at the level of ideal phenomena, either particle or wave effects can be observed, as stated by the complementarity principle. However, if one is not in the idealized situation, both particle

and wave aspects appear simultaneously (Mizobuchi and Ohtaké, 1992; Ghose *et al.*, 1992).

The normalized minimum uncertainty states for the photon numbers and phase were constructed by Jackiw (1968) as a solution of the eigenvalue problem

$$(\Delta\hat{n} + i\xi\Delta\widehat{S})|\psi\rangle = 0, \tag{36}$$

with ξ being a complex parameter. Then the phase operator can be defined with the help of the relation

$$\widehat{\exp}(i\varphi) = \exp(i\bar{\varphi})\sum_{n=0}^{\infty}|n\rangle\langle n+1|, \tag{37}$$

where $\bar{\varphi}$ is obtained as a dominant phase $\arg\langle\widehat{\exp}(i\varphi)\rangle$. The Jackiw states are also called the crescent states as they have the uncertainty (noise) area in the form of a crescent.

Pegg and Barnett (1989) succeeded in constructing a Hermitian phase operator defined in a finite dimensional Hilbert space,

$$|\theta_m, s\rangle = \frac{1}{\sqrt{s+1}}\sum_{n=0}^{s}\exp(in\theta_m)|n\rangle, \tag{38}$$

where

$$\theta_m = \theta + 2\pi\frac{m}{s+1}, \quad m = 0, 1, \ldots, s, \tag{39}$$

with θ being a chosen value, which uses Loudon's (1973) definition of phase states. These states form an orthogonal system, and a phase operator is defined as

$$\widehat{\Phi}_{\theta,s} = \sum_{m=0}^{s}\theta_m|\theta_m, s\rangle\langle\theta_m, s|. \tag{40}$$

Any phase function can be represented by the operator

$$\widehat{M}_{\theta,s} = \sum_{m=0}^{s}M(\theta_m)|\theta_m, s\rangle\langle\theta_m, s|. \tag{41}$$

The values of the phase available by measurements are then obtained in the limit $s \to \infty$.

A phase distribution $P(\varphi)$ is obtained as

$$P(\varphi) = \lim_{s\to\infty}\frac{s+1}{2\pi}\langle\theta_m, s|\hat{\varrho}|\theta_m, s\rangle$$

$$= \frac{1}{2\pi} \sum_{m,n=0}^{\infty} \exp\left[-i(m-n)\varphi\right] \varrho_{nm}. \tag{42}$$

With the help of $P(\varphi)$ we can define the phase variance $\langle (\Delta \widehat{\Phi}_\theta)^2 \rangle = \langle \widehat{\Phi}_\theta^2 \rangle - \langle \widehat{\Phi}_\theta \rangle^2$, $\langle \Phi_\theta^k \rangle = \int_\theta^{\theta+2\pi} \varphi^k P(\varphi)\, d\varphi$, fulfilling the uncertainty relation:

$$\left\langle (\Delta \hat{n})^2 \right\rangle \left\langle (\Delta \widehat{\Phi}_\theta)^2 \right\rangle \geq \frac{1}{4}. \tag{43}$$

The use of the definition in Eq. (33) makes it possible to represent any function $M(\varphi)$ by the operator

$$\widehat{M} = \frac{1}{2\pi} \int_\theta^{\theta+2\pi} M(\varphi) |\varphi\rangle\langle\varphi|\, d^2\varphi, \tag{44}$$

where the phase states

$$|\varphi\rangle = \sum_{n=0}^{\infty} \exp(in\varphi)|n\rangle \tag{45}$$

fulfill an approximate orthogonal relation

$$\langle \varphi | \varphi' \rangle = \pi \delta(\varphi - \varphi') + \frac{1}{1 - \exp[-i(\varphi - \varphi')]}. \tag{46}$$

The cosine and sine phase operators in Eq. (30) can then be written as

$$\begin{aligned} \widehat{C} &= \frac{1}{2\pi} \int_\theta^{\theta+2\pi} \cos(\varphi) |\varphi\rangle\langle\varphi|\, d\varphi, \\ \widehat{S} &= \frac{1}{2\pi} \int_\theta^{\theta+2\pi} \sin(\varphi) |\varphi\rangle\langle\varphi|\, d\varphi, \end{aligned} \tag{47}$$

with the phase distribution being

$$P(\varphi) = \langle \varphi | \hat{\varrho} | \varphi \rangle / 2\pi. \tag{48}$$

It seems that different quantum phase concepts are related to different experimental arrangements used for phase measurements. Recently Noh *et al.* (1992a, 1992b) suggested an operational definition of quantum phase. Superposing two beams at a beamsplitter (see Figure 6), the integrated intensities measured by the photodetectors placed at the two outputs of a

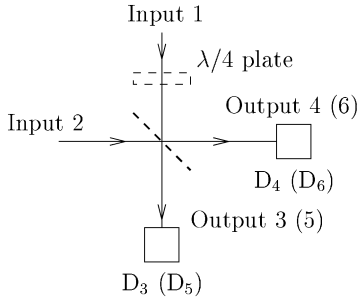

FIGURE 6. A scheme of measurements of the sine and cosine of the phase difference of two beams.

beamsplitter in terms of input signals read

$$W_{3,4} = \frac{1}{2}\big[W_1 + W_2 \mp 2W_{12}\sin(\phi)\big], \tag{49}$$

when $\phi = \phi_1 - \phi_2$ is the difference of the phases of the single beams if a symmetric beam splitter is adopted. Performing a second measurement with a $\lambda/4$-plate, as indicated in Figure 6, we can similarly determine

$$W_{5,6} = \frac{1}{2}\big[W_1 + W_2 \pm 2W_{12}\cos(\phi)\big]. \tag{50}$$

Here

$$W_j = \eta \int_t^{t+T} I_j(t')\,dt' \quad \text{and} \quad W_{12} = \eta \int_t^{t+T} \big[I_1(t')I_2(t')\big]^{1/2}\,dt'. \tag{51}$$

The mutual quantity W_{12} need not be directly measured. Squaring and adding Eqs. (49) and (50), we obtain for W_{12}^2

$$4W_{12}^2 = (W_4 - W_3)^2 + (W_6 - W_5)^2, \tag{52}$$

and so the sine and cosine of the phase difference of both beams can be operationally defined and measured as follows:

$$\begin{aligned} \sin(\phi) &= \frac{W_4 - W_3}{[(W_4 - W_3)^2 + (W_6 - W_5)^2]^{1/2}}, \\ \cos(\phi) &= \frac{W_5 - W_6}{[(W_4 - W_3)^2 + (W_6 - W_5)^2]^{1/2}}. \end{aligned} \tag{53}$$

Merging the two setups of Figure 6 to an eight-port interferometer, $S = \sin(\phi)$ and $C = \cos(\phi)$ can be measured simultaneously. Noh *et al.* (1992a, 1992b)

also analyzed higher-order moments $\langle S^r \rangle$ and $\langle C^r \rangle$ and demonstrated that the $\widehat{S}$- and $\widehat{C}$-operators corresponding to the sine and cosine of the quantum-phase difference between the two input beams in terms of the annihilation and creation operators read

$$\begin{aligned} \widehat{S} &= iK_2\left[\exp(i\varphi)\hat{a}_2^\dagger\hat{a}_1 - \exp(-i\varphi)\hat{a}_1^\dagger\hat{a}_2\right], \\ \widehat{C} &= K_1\left[\exp(i\varphi)\hat{a}_2^\dagger\hat{a}_1 + \exp(-i\varphi)\hat{a}_1^\dagger\hat{a}_2\right], \end{aligned} \tag{54}$$

where K_1 and K_2 are constants and φ is the phase difference. It holds that $[\widehat{C}, \widehat{S}] = 2iK_1K_2(\hat{n}_2 - \hat{n}_1)$ and $[\widehat{S}, \hat{n}_1 + \hat{n}_2] = [\widehat{C}, \hat{n}_1 + \hat{n}_2] = \hat{0}$. If one of the beams were strong enough to be described classically, then the operators in Eq. (54) would have been reduced to a definition of quadratures. Such quadrature measurement is called *optical homodyne measurement*. Let us mention in passing that its generalization to neutron optics is not straightforward due to the fermionic nature of neutrons (see also Section X.A) and thus the lack of strong coherent local oscillators for neutrons. Formulas in Eq. (54) are then operator generalizations of quadrature measurements.

The theoretical as well as experimental analysis of Noh *et al.* (1993) and Fougères *et al.* (1994a, 1994b) demonstrated that there is agreement with the conclusion that the phase difference is well defined only when there is a large uncertainty in photon numbers. Conversely, the moments of the sine and cosine operators correspond to completely uncertain phase difference when the photon numbers are certain. Furthermore, these authors found that when the fluctuations of phases and amplitudes are correlated, it is difficult to measure the phase difference of weak quantum as well as classical fields. It seems that a phase operator should be introduced with a definite measurement scheme in mind. This leads to different phase operators. As a universal principle, the correspondence with classical phase concept in the limit of high intensities should be followed since in classical optics the phase is uniquely defined. Conversely, it is impossible to find a unique quantum phase operator representing the phase or phase difference between two quantum fields.

2. *Phase Estimation*

As discussed previously, phase measurements differ from conventional measurements such as the measurements of position and momentum in that a Hermitian phase operator does not exist in the canonical sense (Nieto, 1993; Royer, 1996; Lynch, 1995; Peřinová and Lukš, 1998; Luis and Sánchez-Soto, 2000). However, this does not mean that the phase of weak signals cannot be described and measured.

From the point of view of estimation theory (Helstrom, 1976), the phase is a c-number parameter appearing in the transformation describing the action

of a phase shifter on the input state $|\Psi\rangle$

$$\left|\Psi(\bar{\theta})\right\rangle = e^{-i\bar{\theta}\hat{n}}|\Psi\rangle, \tag{55}$$

where $\hat{n} = \hat{a}^{\dagger}\hat{a}$ is the photon-number operator. Any phase measurement is completely described by the statistics $p(\theta|\bar{\theta})$ of its outcomes θ conditioned to the true value $\bar{\theta}$ of the phase shift. Basically, two strategies may arise. One can either look for the *ideal measurement* (Yurke *et al.*, 1986; Lane *et al.*, 1993; Holland and Burnett, 1993; Sanders and Milburn, 1995; Chizhov *et al.*, 1998), that is, a measurement that is optimal from some point of view, or, if a measurement cannot be chosen at our will, one should choose the statistical data analysis extracting as much information as possible about the parameter of interest.

It is known from Helstrom (1976) that the statistics of the ideal phase measurement are just the statistics of the Susskind–Glogower phase operator (Susskind and Glogower, 1964):

$$p(\theta|\bar{\theta}) = \frac{1}{2\pi}\left|\langle\theta|\Psi(\bar{\theta})\rangle\right|^2, \qquad \widehat{U}|\theta\rangle = e^{i\theta}|\theta\rangle \tag{56}$$

[see definitions in Eqs. (33), (45), and (48)]. Although the eigenstates of these operators are not orthogonal, [Eq. (46)], they are overcomplete, and thus generate a probability operator valued measure (POVM), $\Pi(\theta) = \{|\theta\rangle\langle\theta|\}$, $\int |\theta\rangle\langle\theta|\, d\theta = 1$, that defines the ideal phase measurement in the sense of generalized measurements.

Although there are ways to simulate the measurement in Eq. (56) by means of post selection (Barnett and Pegg, 1996), this does not seem to be a practical solution. What is usually measured in practice is energy, and interferometers are used to transform phase shifts into variations of output energies. Due to the statistical nature of quantum theory, the resulting relationship between the measured quantities and the parameters of interest is not deterministic. Such an indirect inference is usually called *quantum estimation*, and its scheme is the following:

$$\rho \rightarrow \boxed{\begin{array}{l}\text{True phase}\\ \text{shift } \theta\end{array}} \rightarrow \rho(\bar{\theta}) \rightarrow \boxed{\text{Detection}} \rightarrow \mathbf{D}(\bar{\theta})$$
$$\rightarrow \boxed{\text{Estimation}} \rightarrow \theta(\mathbf{D}).$$

An interferometer provides the input–output transformation of the known initial state ρ. The subsequent measurement yields phase-sensitive data $\mathbf{D}$ that are processed to yield a phase estimate θ. The true phase shift $\bar{\theta}$ inside the interferometer, which is a nonfluctuating parameter controlled by the experimentalist, should carefully be distinguished from the phase estimate θ, which is generally a random quantity.

The performance of the estimation depends on the choice of the estimator. The point estimators of phase corresponding to the maximum-likelihood (ML) estimation are used here (Lane *et al.*, 1993; Hradil, 1997). In accordance with the ML approach (Kendall and Stuart, 1961), the sought-after phase shift is given by the value that maximizes the likelihood function

$$\mathcal{L} \equiv p(\theta|\mathbf{D}) \propto p(\mathbf{D}|\theta). \tag{57}$$

C. Transmission Tomography

Classical tomography is a nondestructive method of determining the distribution of the index of absorption (or scattering cross section) within an object. From the theoretical point of view, tomography is a typical indirect measurement. The absorption in a given point inside the object is not directly accessible to measurement but can be estimated from the "shadows" cast by the object when it is illuminated from many different angles. In contrast to phase measurement, tomography represents a high-dimensional estimation problem.

The basic notions and the geometry of typical tomographic experiments are as follows. Let us assume that the sample is illuminated by parallel monochromatic pencil beams (Figure 7). The data consist of the number of particles counted behind the sample for M different scans—each scan is characterized by its horizontal position h and rotation angle φ. Alternatively, a broad illuminating beam combined with a position-sensitive detector, for instance; a charged coupled device (CCD) camera placed behind the sample can be used. In that case, h labels the pixels of the camera. For the sake of simplicity, a collective index $j \equiv \{h, \varphi\}$ will be used hereafter to label the scans.

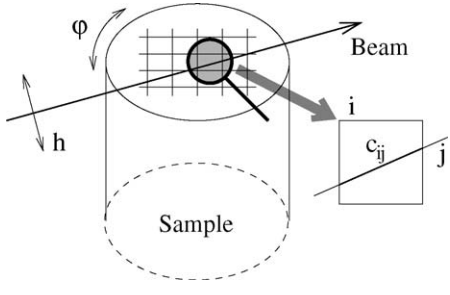

FIGURE 7. Geometry of the experimental setup and the definition of coefficients c_{ij}.

The mean number $\bar{n}_j$ of particles (intensity) registered in the j-th scan is given by the exponential attenuation law

$$\bar{n}_j = \bar{n}_0 \exp\left(-\int \mu(x, y)\, ds_j\right), \tag{58}$$

where $\bar{n}_0$ is the intensity of the incoming beam, $\mu(x, y)$ is the absorption index of the sample in position $\{x, y\}$, and the integration is the path integration along the pencil beam. This exponential attenuation law is a good approximation if multiple scattering can be neglected. The beam-hardening artifacts would also modify Eq. (58), but this complication can be avoided experimentally by the use of monochromatic beams (Dubus *et al.*, 2002).

Using neutron beams instead of X-ray photons has several advantages. Neutrons interact with the matter in a different way than photons do. Since neutrons are subject to the strong interaction, they can "see" and distinguish among different isotopes of the same element. Neutrons can also penetrate deeper into some materials such as metal surfaces, and many other objects such as those made from plastic materials often show considerably more detail when illuminated with neutrons rather than photons.

The absorption index for thermal neutron beams can be expressed as

$$\mu(x, y) = \Sigma_{th}(x, y)\lambda/\lambda_{th}, \tag{59}$$

where Σ_{th} is the macroscopic thermal cross section, λ is the wavelength of the illuminating beam, and $\lambda_{th} \approx 0.18$ nm is the thermal wavelength. Equation (59) presumes a linear dependence of the involved cross sections on λ (Sears, 1989).

For practical purposes, it is convenient to discretize Eq. (58) as follows:

$$\bar{n}_j = \bar{n}_0 \exp\left(-\sum_{i=0}^{N} \mu_i c_{ij}\right). \tag{60}$$

The sample is now represented by a two-dimensional (2D) mesh whose cells are assumed to be homogeneous. The variables are now N numbers μ_i specifying absorption in those elementary cells. The matrix $\{c_{ij}\}$ defines the overlaps of beams and cells (see Figure 7).

Standard Filtered Back-Projection Method

For now let us ignore the statistics of the illuminating beam and assume that the counted numbers of particles $\{n_j\}$ do not fluctuate, $n_j = \bar{n}_j, \forall j$. Taking the logarithms of both sides of Eq. (60), one obtains a system of M linear

algebraic equations for the N unknown absorption coefficients μ_i:

$$f_j = p_j, \quad j = 1, \ldots, M, \tag{61}$$

where we defined

$$f_j = -\ln \frac{n_j}{n_0}, \qquad p_j = \sum_i \mu_i c_{ij}. \tag{62}$$

Notice that the problem in Eq. (61) is a linear and positive (LinPos) problem. Its linearity is obvious, and positivity follows from the fact that no new particles are created in the sample. The importance of LinPos problems in experimental physics stems from the fact that many physical quantities, for instance mass, density, intensity, and so on, are intrinsically positive quantities that very often depend on the parameters of interest in a linear way. Linearized absorption tomography [Eq. (61)] is just one typical example taken from this wide family of problems including, among others, the measurement of focal intensity distribution for polarized input fields (Quabis *et al.*, 2001), or the characterization of the photon content of light pulses (Řeháček *et al.*, 2003) as some examples.

The standard reconstruction method in present computed tomographic (CT) imaging is the filtered back-projection (FBP) algorithm based on the inverse Radon transformation (Kak and Slaney, 1987),

$$\boldsymbol{\mu} \propto \sum_{\varphi} \mathbf{f} \star \mathbf{g}, \tag{63}$$

where $\star$ denotes a discrete convolution of data with the regularized singular transformation kernel (Janicke and Wilkens, 1995). Technically, this transformation is implemented using fast Fourier transformation routines, which makes the reconstruction process fast and highly efficient. However, by the linearity of Eq. (63), the positivity of the reconstructed absorption index is not guaranteed when the data are noisy. A negative value of a reconstructed μ_i would then suggest that particles were being created in the i-th cell in the course of the experiment, which would obviously be a wrong conjecture. Another problem arises when there are only a few projections available. In such a case, the summation in Eq. (63) no longer approximates the original integral and unwanted artifacts appear in the reconstructions. As will be shown later in Section V, all of these problems can be addressed by estimation theory.

D. Phase-Contrast Tomography

The absorption tomography discussed previously provides only partial information about the object of interest. The optical properties of objects are more

thoroughly described by the distribution of the complex index of refraction $n(x, y)$, whose real part is simply called *index of refraction*, and whose imaginary part, called *index of absorption*, are responsible for the phase shift and absorption of the illuminating beam, respectively. It is clear that some kind of interferometric technique is needed for the 3D visualization of the index of refraction. In a sense, phase tomography is a combination of both the previously mentioned inverse problems—the phase estimation introduced in Section III.B and tomographic imaging discussed in Section III.C.

As already mentioned, in neutron optics one is often confronted with low count numbers because the phase space density of present neutron beams is 30 orders of magnitude below that of laser beams and many orders below that of X-ray sources. This intensity problem has dramatically arisen in the recently developed neutron phase-contrast tomography (nPCT) (Zawisky *et al.*, 2004a; Dubus *et al.*, 2005). PCT was originally invented in X-ray tomography with much higher coherent intensities available (Momose, 1995; Momose *et al.*, 1996; Beckmann *et al.*, 1997). In order to use nPCT it is necessary to develop an advanced reconstruction technique, which can be applied to very low count numbers. For instance, the typical count number in present nPCT setups is around 200 n/2 h in a 50×50 μm^2 pixel. In principle, focusing techniques (e.g., asymmetric Bragg reflections), can enhance the density of quasi-monochromatic neutron beams, but such hypothetic gains are used to reduce the measurement time rather than to raise the count numbers. Therefore the low numbers of detected neutrons must be accepted as the limiting factor of nPCT.

A strong motivation for developing nPCT is its extreme sensitivity, which is at least three orders of magnitude higher than in the conventional absorption tomography. The nPCT method proves its strength in extreme applications where other methods fail: (1) 3D investigation of non- or weak-absorbing substances, (2) analysis of isotope distributions with high sensitivity, (3) investigation of magnetic domains in bulk materials (Badurek *et al.*, 2000a), and (4) energy and momentum exchange free analysis of magnetic (axial) and scalar potentials.

The experimental setup of nPCT is schematically shown in Figure 8. The sample is inserted into one arm of a perfect-crystal interferometer while an object of known characteristics placed in the other arm compensates the large overall phase shift introduced by the thick sample. The output beam is then registered by a CCD camera with the spatial resolution of 50 μm. As with absorption tomography, the sample is rotated around the vertical axes and up to several tens of scans are registered. The angle φ together with the position h of a CCD pixel specify the path of the particles registered by that pixel through the sample (see Figure 7). For the sake of brevity, they are represented by a single collective index j.

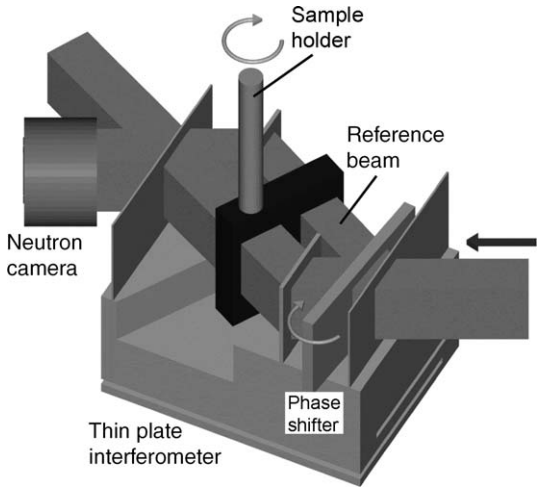

FIGURE 8. Scheme of an nPCT experiment.

To derive an unambiguous value of the reconstructed phase, a set of auxiliary phases δ_j, controlled by the experimenter, is needed for the estimation. They are provided by an auxiliary phase shifter (see Figure 8), and the resulting interferograms are simply called *scans* or *phase projections* (Rauch and Werner, 2000a). In nPCT their number should be chosen as low as possible to minimize the measurement time. As in transmission tomography, a correct statistical treatment of an nPCT experiment is crucial for obtaining good reconstructions. This is discussed in Section VI.

E. Wave Particle Duality

The concept of duality is an advancement of that of complementarity, first introduced by Bohr (1983) in his famous series of Gedankenexperiments. Bohr's original double-slit Gedankenexperiment was completely based on the Heisenberg uncertainty relation. It demonstrates that the access to path information requires the detection of momentum transfer, which necessarily destroys the visibility of interference fringes. Since those early years, path information has been interpreted as a "particle property," whereas the visibility is viewed as a "wave property." In the previous sections, the visibility was introduced as a quality parameter of the instrumental performance and the purity of the quantum state, but visibility can additionally be affected by which-way information. Duality goes beyond the Heisenberg uncertainty relations because the access to path information does not necessarily require

energy and/or momentum transfer. According to the duality principle, the more information one gains about the neutron's path, the less the visibility of interference. Let us start with a simple one-loop interferometer. As soon as some knowledge exists that the detected neutrons preferably stem either from path I or II, the two quantum alternatives become partly distinguishable, and interference is partly destroyed. Visibility (V) and Predictability (P) are therefore dual features and obey a duality relation (Englert, 1996; Scully *et al.*, 1991):

$$P = \left| \frac{\bar{I}_I - \bar{I}_{II}}{\bar{I}_I + \bar{I}_{II}} \right| = |w_I - w_{II}|, \tag{64}$$

$$V = \frac{2\sqrt{w_I w_{II}}}{w_I + w_{II}} V_i, \tag{65}$$

$$P^2 + V^2 \leq 1. \tag{66}$$

A strict duality ($P = 0$ if $V = 1$ and vice versa) is only fulfilled in the ideal interferometer where $V_i = 1$. From Eq. (65) it is obvious that not the which-way knowledge itself, but the asymmetry of which-way probabilities, $w_I \neq w_{II}$, is sufficient to affect visibility. An interesting extension of these ideas, together with a proposal that leads to a saturation of the inequality in Eq. (66), is detailed in Jakob and Bergou (2003), where other quantum features of the interfering system are also considered.

A simple example of how to access path information is outlined in Figure 9. The use of a partial absorber with transmission probability $0 < a < 1$ allows a smooth manipulation of the neutrons' which-way information and their duality properties. This simple arrangement demonstrates that quantum objects simultaneously assume both duality features, accessible in neutron interferometry experiments (Summhammer *et al.*, 1987; Rauch *et al.*, 1990). But here the duality is measured via energy-momentum exchange because some neutrons will be absorbed. A more sophisticated example of "interaction-free" duality measurements is presented in Section VII.

F. Interaction-Free Measurement

The idea of interaction-free measurement was proposed by Elitzur and Vaidman (1993) several years ago. Previous work by Renninger (1960) and Dicke (1981, 1986) is relevant. The former discussed a situation in which a detector does not detect anything, yet there is a change in the state of the measured system. Such a situation is now known as a "negative result measurement." The latter looked at a similar situation and focused on the

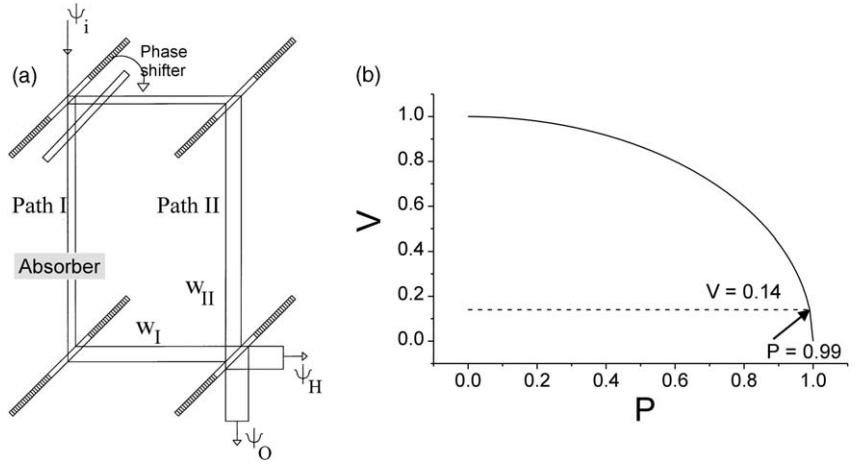

FIGURE 9. Accessing path information by inserting a partial absorber in path I (a). The visibility can be smoothly tuned by changing the transmission probability a: $V = \frac{2\sqrt{a}}{a+1} V_i$. In the ideal case $V_i = 1$, it follows $P^2 + V^2 = 1$ (b). Even in the case of large path information, a remarkable visibility can be maintained.

peculiar fact that although no interaction seemingly takes place, the wave function and the physical features of the system are different after a negative result measurement. This has observable consequences.

Elitzur and Vaidman (1993) showed that the existence of an absorbing object can be inferred without seemingly interacting with the probe particle. We refer again to the Mach–Zehnder interferometer in Figure 9. Assume that the transmission and reflection coefficients of the two beamsplitters are $1/2$, and no phase shifters or absorber are present, so that a neutron incident in state ψ_i exits from the lower port (ordinary beam O) in state ψ_O, with probability 1. However, if an absorber is placed in one of the two (say the left) paths, there is a 25% probability that the neutron will exit from the right lower port (extraordinary beam H). This reveals the presence of the absorbing object even though the probe particle is not absorbed (hence, the idea of "interaction-free measurement"). An interesting account of this phenomenon is provided by Hafner and Summhammer (1997). We notice that an "interaction" does take place (so the term "interaction-free" is somewhat misleading), as a quantum system is indivisible and one of its branch waves is affected by the absorber.

The efficiency of the above-mentioned scheme is rather low, because there is a 50% probability that the probe particle will be absorbed. However, the performance can be dramatically increased by making use of the so-called *quantum Zeno effect*, which is discussed in depth in the following subsection.

In principle, by making use of the quantum Zeno effect, the efficiency of an interaction-free measurement can be made arbitrarily close to unity (Peres, 1980; Pascazio *et al.*, 1993). This was shown experimentally a few years later (Kwiat *et al.*, 1995). We will scrutinize this and related ideas in Section VIII.

G. *Quantum Zeno Effect*

Frequent measurements can slow the time evolution of a quantum system, hindering transitions to states different from the measured one (Misra and Sudarshan, 1977; Pascazio *et al.*, 1993; Nakazato *et al.*, 1996; Home and Whitaker, 1997; Facchi and Pascazio, 2001). This is, in a few words, the *quantum Zeno effect* (*QZE*), which has been experimentally tested both on oscillating systems (Cook, 1988; Itano *et al.*, 1990, 1991; Nagels *et al.*, 1997; Balzer *et al.*, 2000; Toschek and Wunderlich, 2001; Wunderlich *et al.*, 2001; Petrosky *et al.*, 1990, 1991; Peres and Ron, 1990; Inagaki *et al.*, 1992; Blanchard and Jadczyk, 1993; Altenmüller and Schenzle, 1994; Pascazio and Namiki, 1994; Berry, 1995; Luis and Peřina, 1996; Beige and Hegerfeldt, 1996; Schulman, 1998; Thun and Peřina, 1998; Facchi *et al.*, 2001b; Řeháček *et al.*, 2000a) and unstable ones (Wilkinson *et al.*, 1997; Fischer *et al.*, 2001). The same physical effects can be obtained by very strongly coupling the system to an external apparatus, whose action can be viewed as a "measurement" of some sort. However, here follow the usual approach to QZE, which uses "pulsed" observations of the quantum state (Figure 10).

Let $\widehat{H}$ be the total Hamiltonian of the quantum system and ψ_0 its initial state. The survival amplitude and probability of the system in state $|\psi_0\rangle$ are

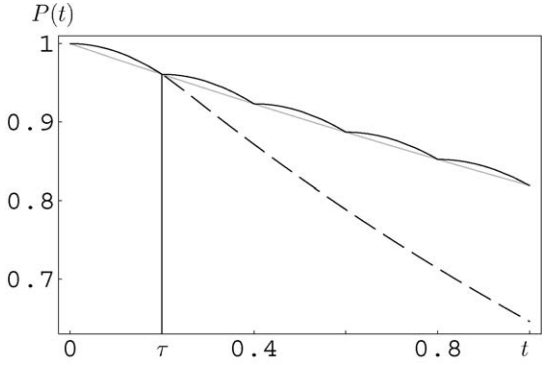

FIGURE 10. Quantum Zeno effect due to frequent measurements. The dashed line is the survival probability without measurements; the solid line represents the survival probability with measurements. (Time t in arbitrary units.)

expressed as

$$A(t) = \langle \psi_0 | \psi_t \rangle = \langle \psi_0 | e^{-i\widehat{H}t} | \psi_0 \rangle, \quad \text{and} \tag{67}$$

$$P(t) = \left| A(t) \right|^2 = \left| \langle \psi_0 | e^{-i\widehat{H}t} | \psi_0 \rangle \right|^2, \tag{68}$$

respectively. An elementary expansion yields a quadratic behavior at short times

$$P(t) \sim 1 - t^2/\tau_Z^2 \sim e^{-t^2/\tau_Z^2}, \qquad \tau_Z^{-2} \equiv \langle \psi_0 | \widehat{H}^2 | \psi_0 \rangle - \langle \psi_0 | \widehat{H} | \psi_0 \rangle^2. \tag{69}$$

The quantity τ_Z is the so-called Zeno time and is the convexity of $P(t)$ in the origin. For oscillating systems, τ_Z yields a good estimate of the short time evolution. (Warning: For *bona fide* unstable systems the asymptotic expansion in Eq. (69) can be valid only for extremely short times, which are generally much shorter than τ_Z. In such a case, it is misleading to view the Zeno time as yielding an accurate estimate of the short time behavior.)

It is often convenient to divide the total Hamiltonian into free and an interaction parts, H_0 and H_I, respectively:

$$\widehat{H} = \widehat{H}_0 + \widehat{H}_I. \tag{70}$$

By requiring

$$\widehat{H}_0 | \psi_0 \rangle = E_0 | \psi_0 \rangle, \qquad \langle \psi_0 | \widehat{H}_I | \psi_0 \rangle = 0, \tag{71}$$

the Zeno time is expressed as

$$\tau_Z^{-2} = \langle \psi_0 | \widehat{H}_I^2 | \psi_0 \rangle \tag{72}$$

and depends only on the interaction Hamiltonian. Notice that, even if the conditions in Eq. (71) do not define a unique splitting [Eq. (70)], the expression [Eq. (72)] is always valid and depends only on the block off-diagonal part of the Hamiltonian with respect to the decomposition $\widehat{P} + \widehat{Q} = 1$, with $\widehat{P} = |\psi_0\rangle\langle\psi_0|$.

To determine the QZE, we perform N measurements at short time intervals τ, to check whether the system is still in its initial state. The survival probability after the measurements is

$$P^{(N)}(t) = P(\tau)^N = P(t/N)^N \overset{N \text{ large}}{\longrightarrow} \exp\left(-t^2/N\tau_Z^2\right) \overset{N\to\infty}{\longrightarrow} 1, \tag{73}$$

where $t = N\tau$ is the total duration of the experiment. The Zeno evolution is pictorially represented in Figure 10.

The QZE is a direct consequence of the Schrödinger equation, which yields quadratic behavior of the survival probability at short times: in a short time $\delta\tau \sim 1/N$, the phase of the wave function evolves like $O(\delta\tau)$, while the

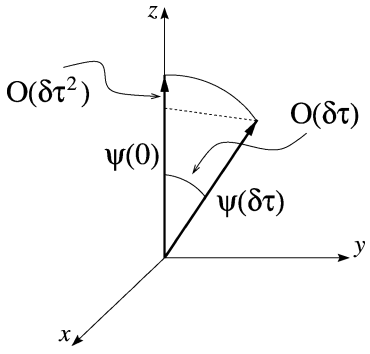

FIGURE 11. Short-time evolution of phase and probability.

probability changes by $O(\delta\tau^2)$, so that

$$P^{(N)}(t) \sim \left[1 - O\left(1/N^2\right)\right]^N \overset{N\to\infty}{\longrightarrow} 1. \tag{74}$$

This is sketched in Figure 11 and is a very general feature of the Schrödinger equation. In fact, many other fundamental physical equations share the same property.

New phenomena occur when one considers unstable systems. In particular, other regimes become possible, in which measurement *accelerates* the dynamic evolution, giving rise to an *inverse* QZE (Lane, 1983; Schieve *et al.*, 1989; Facchi and Pascazio, 2000; Elattari and Gurvitz, 2000; Kofman and Kurizki, 2000; Luis and Sánchez-Soto, 1998; Řeháček *et al.*, 2000b; Facchi *et al.*, 2001c; Koshino and Shimizu, 2003). This is not discussed in detail here; we mention only a few important facts. Equation (73) can be rewritten as

$$P^{(N)}(t) = \exp\left(N \log P(\tau)\right) = \exp\left(-\gamma_{\text{eff}}(\tau)t\right), \tag{75}$$

by introducing the effective decay rate

$$\gamma_{\text{eff}}(\tau) \equiv -\frac{1}{\tau} \log P(\tau). \tag{76}$$

For instance, for times τ such that the quadratic behavior in Eq. (69) is valid with good approximation [but see the "warning" after Eq. (69)], one easily checks that

$$\gamma_{\text{eff}}(\tau) \sim \tau/\tau_Z^2 \quad (\tau \to 0) \tag{77}$$

is a linear function of τ. If it is possible to find a finite time τ^* such that

$$\gamma_{\text{eff}}(\tau^*) = \gamma, \tag{78}$$

then, by performing measurements at time intervals τ^*, the system decays according to its "natural" lifetime, as if no measurements were performed. However, in general, when measurements are performed at generic time intervals τ, the effective decay rate $\gamma_{\text{eff}}(\tau)$ is derived. Under general hypotheses, if $\tau = \tau_1 < \tau^*$, one obtains QZE; conversely, if $\tau = \tau_2 > \tau^*$, one obtains an inverse Zeno effect.

The recent interest on the QZE and its inverse are due to the possibility of controlling and eventually partially suppressing decoherence (Facchi *et al.*, 2005). These applications can be relevant, for example, in quantum information and macroscopic quantum phenomena.

H. Wigner Function

The Wigner quasi-distribution (function) $W(\alpha)$ is defined in terms of the coherent states as the complex Fourier transformation of the symmetrically ordered quantum characteristic function $C(\beta) = \text{Tr}\{\hat{\rho}\widehat{D}(\beta)\}$, where $\widehat{D}(\beta) = \exp(\beta\hat{a}^\dagger - \beta^*\hat{a})$ is the displacement operator expressed in terms of boson annihilation and creation operators $\hat{a}$ and $\hat{a}^\dagger$, respectively, and $\hat{\rho}$ is the density matrix:

$$W(\alpha) = \frac{1}{\pi^2}\int C(\beta)\exp(\alpha\beta^* - \alpha^*\beta)\,d^2\beta, \tag{79}$$

where the integration is taken over the whole complex plane β.

By defining the quadrature operators

$$\hat{x}(\theta) = \frac{\hat{a}\exp(-i\theta) + \hat{a}^\dagger\exp(i\theta)}{2}, \qquad \hat{p}(\theta) = \frac{\hat{a}\exp(-i\theta) - \hat{a}^\dagger\exp(i\theta)}{2i}, \tag{80}$$

where θ represents an angle of the coherent local oscillator, we can write the Wigner function in terms of the quadratures as

$$W(x, p) = \frac{1}{\pi}\int \langle x + x'|\hat{\rho}|x - x'\rangle \exp(-2ipx')\,dx'. \tag{81}$$

If a quantum state is pure and described by the wave function ψ, we obtain the following:

$$W(x, p) = \frac{1}{\pi}\int \psi^*(x + x')\psi(x - x')\exp(-2ipx')\,dx'. \tag{82}$$

The Wigner function is bounded, compared to, for example, the Glauber–Sudarshan quasi-distribution; however, it may take on negative values, expressing the quantum behavior of physical systems.

I. Nonclassical States of Neutrons

The Wigner function can be regarded as a quantum generalization of the Louisville distribution function of a classical ensemble. As in classical mechanics, the marginal integrals of the Wigner function yield the probability densities of position and momentum:

$$\int_{-\infty}^{\infty} W(x, p)\, dx = P(p), \qquad \int_{-\infty}^{\infty} W(x, p)\, dp = P(x). \tag{83}$$

Clearly,

$$\int W(x, p)\, dx\, dp = \mathrm{Tr}\ \hat{\rho} = 1. \tag{84}$$

Quantum states can be divided into two groups. Some states have nonnegative Wigner functions. In this case, the state of the quantum system is fully specified by the joint probability distribution $W(x, p)$, which also provides its realistic hidden variable model. Such states are said to be *semi-classical*. The second group consists of states whose Wigner functions exhibit negative regions. Here the probabilistic interpretation of Wigner function fails and consequently a *nonclassical behavior* might be observed.

A simple example of a semi-classical state is a Gaussian wave packet,

$$\psi(x) = \frac{1}{(2\pi\delta^2)^{1/4}} \exp\left[-\frac{(x - x_0)^2}{4\delta^2} + ip_0 x\right], \tag{85}$$

where δ is proportional to the uncertainty in position. Its Wigner function is positive and has a Gaussian expression

$$W(x, p) = \frac{1}{\pi} \exp\left[-\frac{(x - x_0)^2}{2\delta^2}\right] \exp\left[-2\delta^2 (p - p_0)^2\right] \tag{86}$$

(see Figure 12(a)). Note that Gaussian states minimize the Heisenberg uncertainty product $\Delta x \Delta p$. From this point of view, they represent the closest quantum approximation of a classical center-of-mass motion.

Interesting examples of nonclassical states can be obtained by superposing two spatially separated Gaussian states,

$$\psi(x) \propto e^{-(x-\Delta)^2/4\delta^2} + e^{-(x+\Delta)^2/4\delta^2}. \tag{87}$$

These states can be obtained by splitting and then recombining a neutron wave packet in an interferometer or a polarized neutron wave packet in a magnetic field (Badurek *et al.*, 2000b). The corresponding Wigner function is readily

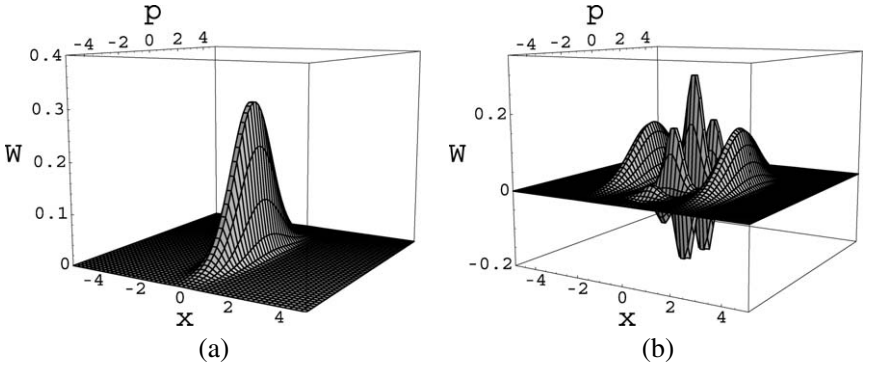

FIGURE 12. Wigner representation of a Gaussian state (a) and superposition of two spatially separated Gaussian states (b); $x_0 = p_0 = 0$ and $\delta = 1/4$, $\Delta = 2$ in arbitrary units.

computed:

$$W_{\mathrm{O}}(x, p, \Delta) = \frac{1}{4\pi} \exp\left[-2\delta^2 (p - p_0)^2\right] \left[\exp\left(-\frac{(x - x_0 + \Delta)^2}{2\delta^2} \right) + \exp\left(-\frac{(x - x_0 - \Delta)^2}{2\delta^2} \right) + 2 \exp\left(-\frac{(x - x_0)^2}{2\delta^2} \right) \cos(2k\Delta) \right]. \tag{88}$$

Notice that, for $\Delta \neq 0$, it is not normalized to unity (some neutrons end up in other output channels) and that for $\Delta = 0$ one recovers Eq. (86).

States with large separations $\Delta \gg \delta$ are often called *Schrödinger cat states*, despite the complexity of the one-particle system here it is obviously far below that of the systems Schrödinger had in mind. The Wigner function of a cat state is shown in Figure 12(b). The strong oscillations in momentum, which are a sign of the nonclassical interference of the spatially separated wave packets, are clearly seen between the two Gaussian lobes representing the individual components of Eq. (87). The significant negative parts of the Wigner function also manifest the nonclassical nature of the cat state. The preparation of cat states in neutron optics is provided by the possibility of using large phase shifts in neutron interferometers. Wave packets taking the longer path can be delayed with respect to the other component to such an extent that, at the output, the two components no longer overlap. The interference fringes observable for small shifts Δ disappear—they are coherently replaced by a nonclassical interference in momentum distribution.

J. Quantum State Tomography

Tomography is an advanced technique, which helps visualize the cross-sectional images of 3D objects by measuring their projections. Today it is used routinely in medicine in X-ray or nuclear magnetic resonance (NMR) imaging methods. The mathematical background of this sophisticated technique is given by the Radon theorem, showing the unique relationship between the volume and its projections—shadows. This technique may be further generalized and adopted for the reconstruction of more abstract objects such as the Wigner function and so on.

Let us briefly explain the main features of standard Radon transformation in the 2D case. Assume a generic distribution $f(x, y)$ in the plane, which should be reconstructed by using the projections along the parallel lines in the fixed coordinate system. Using the parametrization of the lines

$$x \cos\theta + y \sin\theta - t = 0, \tag{89}$$

they all have the normal vector $(\cos\theta, \sin\theta)$. The parameter t determines the distance between the line and origin of the coordinate system. The projection along the line is simply given by

$$g(t, \theta) = \int_{-\infty}^{\infty} \int_{-\infty}^{\infty} dx\, dy f(x, y) \delta(x \cos\theta + y \sin\theta - t). \tag{90}$$

The integration over the Dirac delta function may be performed using a suitable substitution yielding the explicit form of Radon transformation for the projections

$$g(t, \theta) = \int_{-\infty}^{\infty} f(t \cos\theta - u \sin\theta, t \sin\theta + u \cos\theta)\, du. \tag{91}$$

The image reconstruction from the projections may be formulated as the inverse Radon transformation. This can be easily achieved by Fourier transformation. Elementary calculations show the relationship between the 1D Fourier transformation of the measured projection and 2D Fourier transformation of the object

$$G_\theta(\xi) = F(\xi \cos\theta, \xi \sin\theta). \tag{92}$$

Here the Fourier images are defined as

$$G_\theta(\xi) = \int_{-\infty}^{\infty} g(s,\theta)\exp[-2\pi i\xi s]\,ds,$$
$$F(f_x, f_y) = \int_{-\infty}^{\infty}\int_{-\infty}^{\infty} dx\,dy\exp\bigl[-2\pi i(f_x x + f_y y)\bigr]. \tag{93}$$

The inverse Radon transformation then reads

$$f(x,y) = \int_0^{\infty}\int_0^{\pi}\int_{-\infty}^{\infty} ds\,d\xi|\xi|\,d\theta g(s,\theta)e^{2\pi i(x|\xi|\cos\theta + y|\xi|\sin\theta - \xi s)}. \tag{94}$$

Notice that the reconstructed image is fully determined by the measured projections for all angles $\theta \in (0,\pi)$. Although the reconstruction procedure is simple, the kernel of the integral transformation is strongly singular. This causes various artifacts if the reconstruction is applied to realistic data. This problem will be treated from the statistical point of view in Section X.

Let us show how the Radon transformation manifests itself in the quantum domain. The analogy between the classical and quantum Radon transformation may be easily established for the detection of quadrature operator rotated by an angle θ and Wigner function,

$$w(x,\theta) \equiv \langle x_\theta|\hat{\rho}|x_\theta\rangle = \int W(x\cos\theta - v\sin\theta, x\sin\theta + v\cos\theta)\,dv. \tag{95}$$

As follows from quantum mechanics, Wigner function W plays the role of a 2D object, whereas the detected probabilities w represent the corresponding projections. Notice, however, that the Wigner function may attain negative values as a signature of the nonclassical behavior of the object; this is to be contrasted to the classical situation. The explicit form inverse Radon transformation for Wigner quasi-distribution is

$$W(\alpha_r,\alpha_i) = \frac{1}{4\pi^2}\int_{-\infty}^{\infty}\int_{-\infty}^{\infty}\int_0^{\pi} w(x,\theta)|\eta|e^{i\eta(x-\alpha_r\cos\theta-\alpha_i\sin\theta)}\,dx\,d\eta\,d\theta. \tag{96}$$

IV. Testing Quantum Phase in Matter-Wave Optics

This section shows that the operational phase concepts discussed in Section III.B can naturally be embedded in the general scheme of quantum estimation theory (Helstrom, 1976; Jones, 1991) as was done by Hradil *et al.*

(1996), Zawisky *et al.* (1998), and Řeháček *et al.* (1999, 2000c). Following this link, a more general description of phase measurements will be given yielding measurable improvements on the standard semi-classical theory.

Let us consider a neutron interferometer (or optical Mach–Zehnder interferometer), where the measurement is performed without/with $\lambda/4$ ($\pi/2$) auxiliary phase shifters. The auxiliary shifter is needed to provide a unique phase estimate. Such a two-step measurement is equivalent to the eight-port homodyne detection scheme (Noh *et al.*, 1991) shown in Figure 6 with the four output channels numbered by indexes 3, 4, 5, and 6, where the numbers of particles are registered in each run. Assume that these quantities fluctuate in accordance with some statistics. According to Eqs. (49) and (50), the mean detected numbers of particles (mean intensities) are modulated by a phase parameter $\bar{\theta}$

$$\bar{n}_{3,4} = \frac{N}{2}(1 \pm V\cos\bar{\theta}), \qquad \bar{n}_{5,6} = \frac{N}{2}(1 \pm V\sin\bar{\theta}), \tag{97}$$

where N is the total intensity and V is the visibility of the interference fringes. Provided that a particular combination of outputs $\{n_3, n_4, n_5, n_6\}$ has been registered, the phase shift can be inferred.

Now, for a while, assume that the phase-sensitive device operates with a Gaussian signal with phase-insensitive noise. This is only an approximation of the real situation, since realistic signals are discrete. Under such an approximation, the likelihood function corresponding to the detection of given data is

$$\mathcal{L} \propto \exp\left\{-\frac{1}{2\sigma^2}\sum_{i=3}^{6}[n_i - \bar{n}_i]^2\right\}. \tag{98}$$

Here the variance σ^2 represents the phase-insensitive noise of each channel. The sampling of intensities may serve for the estimation of the phase shift and visibility simultaneously. The likelihood function in Eq. (98) is maximized on the physically allowed space of parameters $V \leq 1$ by the following phase and visibility:

$$e^{i\theta} = \frac{n_3 - n_4 + i(n_5 - n_6)}{\sqrt{(n_3 - n_4)^2 + (n_5 - n_6)^2}}, \tag{99}$$

$$V = \min\left(2\frac{\sqrt{(n_3 - n_4)^2 + (n_5 - n_6)^2}}{\sum_{i=3}^{6} n_i}, 1\right). \tag{100}$$

Notice that the prediction of this semi-classical theory [Eq. (99)] coincides with the operational quantum phase of Eq. (53) introduced by Noh, Fougères, and Mandel (NFM) (1993). This means that operational phase concepts can

be thought of as special cases of ML phase estimation—ML estimation for Gaussian signals. Such predictions are optimal only for signals represented by a continuous Gaussian signal with phase-independent and symmetrical noises. Note that a generalization of this concept to a larger number of detected auxiliary phase shifts (Walkup and Goodman, 1973) is known as the phase of the discrete Fourier transformation.

Since realistic signals are discrete, the theory can be refined by considering the actual statistics of the experiment. This can be demonstrated on Poissonian signals. These are frequently encountered in laboratories as ideal lasers, or thermal sources of particles, such as neutron beams. ML estimation based on the Poissonian likelihood function

$$\mathcal{L} \propto \prod_{i=3}^{6} \frac{\bar{n}_i^{n_i}}{n_i!} e^{-\bar{n}_i} \tag{101}$$

gives optimum values for the phase shift and visibility

$$e^{i\theta} = \frac{1}{V}\left[\frac{n_4 - n_3}{n_4 + n_3} + i\frac{n_6 - n_5}{n_6 + n_5}\right], \tag{102}$$

$$V = \sqrt{\left(\frac{n_4 - n_3}{n_4 + n_3}\right)^2 + \left(\frac{n_6 - n_5}{n_6 + n_5}\right)^2} \leq 1, \tag{103}$$

provided that the estimated visibility in Eq. (103) is smaller than unity. If not, it is necessary to maximize the likelihood function in Eq. (101) numerically on the boundary ($V = 1$) of the physically allowed region of parameters.

Equations (102) and (103) provide a correction of the semi-classical Gaussian theory with respect to the discrete Poissonian signals. The principle of inference, together with the two different assumptions about the nature of the signal, have given rise to two different phase estimates [Eqs. (99) and (102)]. One may wonder whether the improvement of phase inference gained by taking the correct statistics of the experiment into account is worth giving up the simple NFM formalism and resorting to numerical methods. Could the optimization of the information yield from the measured data lead to a significant increase of the accuracy of the phase fitting?

The difference between Eqs. (99) and (102) can be tested in a controlled phase measurement. The phase difference is adjusted to a certain value and estimated independently using both methods in Eqs. (99) and (102) in repeated experiments. The efficiency of both methods can then be compared.

Of course, some measure of the estimation error is needed for this. The dispersion defined by the relation

$$\sigma^2 = 1 - \left|\langle \mathrm{e}^{i\theta} \rangle\right|^2 \tag{104}$$

is one such reasonable measure. Here, the average is taken over the posterior phase distribution of the corresponding phase estimator.

The evaluation of the average quadratic cost [Eq. (104)] is not the only way to compare the efficiencies of different estimation procedures. Another possibility is to use the rectangular cost function

$$C(\theta-\bar{\theta})=\begin{cases}-1, & |\theta-\bar{\theta}|\le \Delta\theta,\\ 0, & |\theta-\bar{\theta}|>\Delta\theta.\end{cases} \tag{105}$$

The averaged rectangular cost $\langle C(\theta-\bar{\theta})\rangle$ measures how many times the estimate θ falls within the chosen window $\Delta\theta$ spanning around the true phase $\bar{\theta}$. The difference

$$\Delta E=\left\langle C(\theta-\bar{\theta})\right\rangle_{\text{Gauss}}-\left\langle C(\theta-\bar{\theta})\right\rangle_{\text{Poiss}} \tag{106}$$

then measures how much the Poissonian prediction is better than the Gaussian one. If this quantity is found to be positive, the ML estimation is better than its NFM counterpart.

Although the dispersion [Eq. (104)], and ΔE cannot be calculated explicitly for an arbitrary input intensity N, it is possible to analyze the limit cases (Řeháček *et al.*, 2000c). Obviously, both the predictions in Eqs. (99) and (102) will coincide provided that there is almost no information available in the low-intensity limit, $N\to 0$. Not so obvious is the fact that both predictions will also coincide in the high-intensity limit, $N\gg 1$, provided the visibility is low $V\to 0$. To determine this, let us compare the asymptotic dispersion of the NFM estimator,

$$\sigma_G^2\approx\frac{1}{V^2}N^{-1}+O\left(\frac{1}{N^2}\right), \tag{107}$$

with the asymptotic expression for the Cramér–Rao lower bound (CRLB) on the dispersion of any estimator,

$$\sigma_{\text{CRLB}}^2=\frac{V^2-1-\frac{1}{4}V^4\sin^2 2\bar{\theta}}{V^2-1-\frac{1}{2}V^2\sin^2 2\bar{\theta}}V^{-2}N^{-1}+O\left(\frac{1}{N^2}\right). \tag{108}$$

If the visibility is low, both expressions will become identical. Therefore the semi-classical theory is optimal in this limit case (Walkup and Goodman, 1973).

Asymptotic expressions for various phase estimators in the opposite limit of high visibility $V\approx 1$ are given in Table 1. Estimator ML′ is the phase prediction given by Eq. (102), that is, one accepts the possible unphysical inferred visibilities $V>1$, and ML_1 is the single-parameter estimation obtained by setting $V=1$ in the likelihood function as shown in Eq. (101) and maximizing it only with respect to phase.

TABLE 1
ASYMPTOTIC DISPERSIONS AND OVERALL QUADRATIC COSTS OF VARIOUS PHASE ESTIMATORS

Estimator	σ^2	$\overline{C} \equiv \int \sigma^2 \, d\bar{\theta}$
NFM	$1/N$	$2\pi/N$
ML′	$(1+\cos^2 2\bar{\theta})/2N$	$\frac{3}{2}\pi/N$
ML	$\approx(1+0.5\cos^2 2\bar{\theta})/2N$	$\approx\frac{5}{4}\pi/N$
ML_1	$1/2N$	π/N
CRLB	$1/2N$	π/N

ML′, unconstrained ML estimation; ML_1, single-parameter ML estimation. For comparison, CRLB is also shown.

Notice that the uncertainties of all estimators scale as $1/\sqrt{N}$. This is to be expected in accordance with the standard quantum limit. However, the constant of proportionality depends on the estimator used. The accuracy of phase fitting is improved by taking physical constraints into account.

The single-parameter ML_1 estimator provide the best phase predictions. It attains the CRLB and hence is optimum. It yields a phase prediction whose uncertainty is reduced by the factor of $\sqrt{2}$, that is, by approximately 30%, compared with the semi-classical theory. However, estimating phase alone implicitly presumes good *a priori* knowledge of the visibility. If the actual value of the visibility is not known or fluctuates during the experiment, the single-parameter estimator may lead to biased phase predictions. For large intensities the bias might completely spoil the estimation (Řeháček *et al.*, 2000c).

The performance of the semi-classical NFM and ML phase estimators have been determined in a series of experiments using two principal sources of particles—beams of thermal neutrons (Řeháček *et al.*, 1999) and laser light (Řeháček *et al.*, 2000c). The main goal of these experiments was to compare the optimum phase prediction with the semi-classical theory in the regime of only a few input particles. As a side result, the theoretical asymptotic uncertainties given in Table 1 were tested experimentally.

The dispersions [Eq. (104)] of the NFM (or equivalently Gaussian) and ML phase estimators found in experiments with light are shown in Figure 13. The true phase was fixed at $\bar{\theta} = \pi/3$. The number of detected quadruples $\{n_3, n_4, n_5, n_6\}$ used for the calculation of the dispersions varied from 1000 samples for the input mean number of photons $N = 60$ to more than 100,000 samples for $N = 0.1$. The error bars corresponding to these finite numbers of samples are the result of numerical simulation. The visibility during the experiments was better than 99.6%.

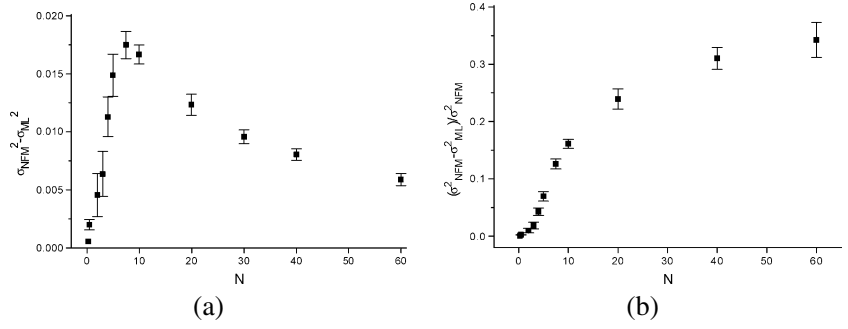

FIGURE 13. The experimentally observed absolute (a) and relative (b) difference between the dispersions of the Noh *et al.* (1993) and ML estimators as a function of the input mean number of photons N for fixed true phase $\bar{\theta} = \pi/3$. Error bars corresponding to 68% confidence intervals are also shown.

The ML estimator was significantly more accurate (by many standard deviations) than its NFM semi-classical counterpart. This was confirmed by evaluating the difference of the rectangular costs [Eq. (106)] (see Figure 14(a)). Here, the chosen input total energy roughly fits the maximum, $N \approx 7.5$, of the curve seen in Figure 13.

A significant difference between the effectiveness of semi-classical and optimal treatments is apparent in Figure 14. The optimal treatment provides

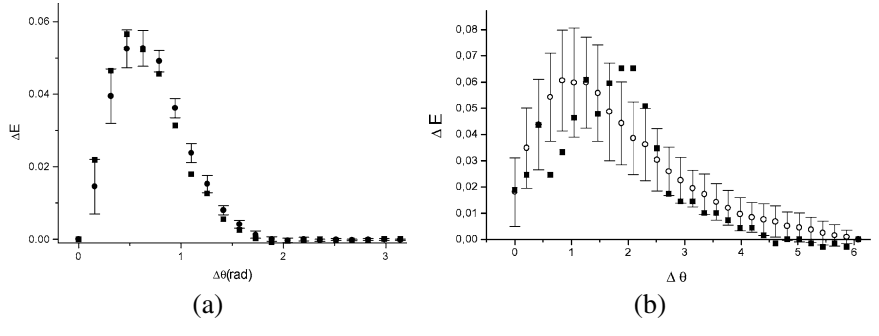

FIGURE 14. Experimentally obtained ΔE (squares) compared to theoretical values (circles). (a) Experiment with photons, $N = 10$ photons. The visibility was better than 99.5%; error bars correspond to 7500 measured samples. (b) Experiment with neutrons. The mean number of $N = 8.54$ incoming neutrons was asymmetrically split between the ordinary ($N_o = 2.21$) and extraordinary ($N_h = 6.33$) channels. The average visibility was about 31%; error bars correspond to 690 registered samples.

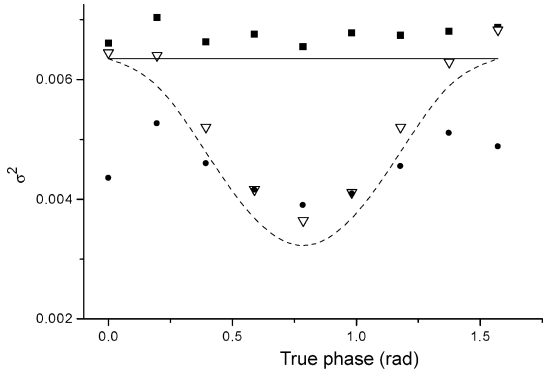

FIGURE 15. Asymptotic dispersions of the semi-classical Noh *et al.* (1993) estimator; theory (solid line) and experimentally obtained values (squares). Asymptotic dispersions of the unconstrained ML estimator; theory (dashed line) and experimentally obtained values (triangles). Experimentally obtained dispersions of the ML estimation on the physical space of parameters (circles). The corresponding input mean number of photons and the estimated visibility were $N = 160$ and $V = 99.2\%$, respectively.

an improvement in estimation procedure, and the difference is more than 10 standard deviations beyond the statistical error. High stability and visibility of interference fringes in the optical interferometer along with a high repetition rate of pulsed lasers made the improvement of the semi-classical phase prediction more evident than in a similar comparison that had been done with thermal neutrons (Řeháček *et al.*, 1999) (see the Figure 14(b)).

An experimental comparison of three different phase estimations—NFM, ML′, and ML estimators—in the asymptotic regime is shown in Figure 15. The experiment was done with photons. For comparison, the theoretical values of dispersions given in Table 1 are also shown. Several important conclusions can be drawn from Figure 15. (1) The uncertainty of the constrained ML estimation is definitely below the uncertainty of the unconstrained estimation in agreement with theory presented in Table 1. It means that insisting on the physical constraints (here the nonnegativity of the intensity) is important not only for the sake of interpretation, but it also makes the estimation more efficient. Of course, both ML estimations beat the phase resolution of the semi-classical NFM theory. (2) The observed values of dispersions exhibit a systematic error. The additional noise above the theoretical uncertainty is caused by inherent phase fluctuations in the experimental setup. Hence, our statistically motivated evaluation of experimental data also can be used for inferring the amount of fluctuations providing an independent and nontrivial calibration of the interferometer.

V. Neutron Transmission Tomography

Tomography is a very efficient imaging method with many applications. This subsection demonstrates how the standard inversion based on Radon transformation reviewed in Section III.J can be improved by means of ML estimation.

FBP gives satisfactory results in applications where (1) the intensity of the illuminating beam is so large that its statistics can safely be ignored, and (2) the sample can be scanned over the entire 180-degree angular interval in small steps. These two conditions are usually met in X-ray medical CT imaging.

Unfortunately, FBP fails in case of missing projections and/or if strong statistical fluctuations of the counting numbers are present in the small detector pixels. The latter situation occurs (e.g., in neutron tomography; Schillinger *et al.*, 1998, 2000; Koerner *et al.*, 2001; McMahon *et al.*, 2001), if monochromatic neutron beams are applied in order to avoid beam artifacts (Dubus *et al.*, 2002) or at the investigation of strong absorbing materials (Zawisky *et al.*, 2004b). Because present neutron sources are thermal in nature, they generate weak beams. Particles that have passed through the studied object are counted one by one and their statistical fluctuations have strong influence on the reconstructed images.

The case of missing projections or incomplete data sets is another important issue. If technical problems arise during the tomographic scan, FBP algorithm requires repeating the whole measurement. Partial or incomplete data cannot be inverted using this method. Sometimes it may be necessary to keep the sample in a cryostat during the measurement. The construction of such a cryostat may not allow turning it upside down, so part of the measured angles may be missing, or there may not be enough space to rotate the sample in the full 180-degree interval. This was investigated in the past in detail by means of algebraic reconstruction techniques (Treimer *et al.*, 1991; Maaß *et al.*, 1992; Treimer and Feye-Treimer, 1998).

A. *Advanced Statistical Inversion*

The ML reconstruction method described in this section can improve several tomographic applications in neutron optics that in many cases are limited by the weak intensity and the poor detector resolution (Allman *et al.*, 2000; Bonse *et al.*, 1991). Generally, it achieves better reconstruction results or reduces the scanning time in neutron optics and in medical and biological CT imaging.

The above-mentioned drawbacks of the FBP algorithm can be avoided if the problem in Eq. (61) is solved in the sense of ML on the space of physically

allowed absorption coefficients. In this approach, the data **f** and the prediction of the theory **p** are considered as two probability distributions. One looks for absorption coefficients $\{\mu_i\}$ minimizing the Kullback–Leibler "distance"

$$D(\mathbf{f}, \mathbf{p}) = -\sum_j f_j \ln \frac{p_j}{f_j} \tag{109}$$

between the data **f** and theory **p**. Here, more care is needed since **p** and **f** are generally not normalized to unity. The minimum of the Kullback–Leibler distance corresponds to the maximum of the likelihood functional (Kendall and Stuart, 1961)

$$\mathcal{L} = \prod_j \left(\frac{p_j}{\sum_k p_k} \right)^{f_j}, \tag{110}$$

that quantifies the likelihood of the given distribution $\{\mu_i\}$ in view of the registered data. We seek the maximum-likely distribution of the absorption indexes. A convenient way to find it is the *expectation–maximization* (EM) iterative algorithm (Dempster *et al.*, 1977; Vardi and Lee, 1993):

$$\boldsymbol{\mu}^{n+1} = \boldsymbol{R}\left(\boldsymbol{\mu}^n\right) \cdot \boldsymbol{\mu}^n, \tag{111}$$

where

$$R_i = \frac{1}{\sum_{j'} c_{ij'}} \sum_j \frac{f_j c_{ij}}{p_j(\boldsymbol{\mu})}, \tag{112}$$

and $\boldsymbol{\mu}^0$ is some initial strictly positive distribution $\mu_i^{(0)} > 0$, $i = 1, \ldots, N$. A nice feature of EM algorithm is that its convergence is guaranteed for any input data f_j (Shepp and Vardi, 1982). For this reason, it became a valuable tool in many inverse problems that can be reduced to the form of Eq. (61) (e.g., in positron emission tomography (Shepp and Vardi, 1982; Vardi *et al.*, 1985; Mair *et al.*, 1996)). The original derivation of EM algorithm is based on alternating projections on specially chosen convex sets of vectors. However, one could directly use the calculus of variations to derive the necessary condition for the extreme of the functional Eq. (110). Iterating these, one eventually arrives at the EM algorithm again. An advantage of this alternative derivation is that it can also be applied to more realistic physical models of the actual absorption experiment. One such possible generalization is shown in the next section.

B. Tomography with Poissonian Neutron Beams

Real signals are not composed of a sharp number of particles. For instance, two kinds of signals often used in experiments—beams of thermal neu-

trons and laser light—both exhibit Poissonian fluctuations of the number of particles. Monochromatic neutron beams also are correctly described by the Poissonian statistics if the detected count events occur in a mutually independent manner (Rauch *et al.*, 1990). The knowledge of the true character of the signal illuminating the sample is a useful piece of prior information, which can be use for improving the performance of the tomographic imaging.

Because the Poissonian character of the signal is preserved during the attenuation, the counted numbers of particles behind the sample are random Poissonian variables. The corresponding likelihood functional is

$$\mathcal{L} = \prod_j \frac{\bar{n}_j^{n_j}}{n_j!} e^{-\bar{n}_j}. \tag{113}$$

This is the joint probability of counting $\{n_j\}$ particles. Their mean values $\{\bar{n}_j\}$ obey the exponential law [Eq. (58)] as before. They depend on the absorption in the sample $\{\mu_j\}$ that is to be inferred from the data. The necessary condition for the maximum of the likelihood in Eq. (113) can be derived using the calculus of variations. The extremal equation can be shown to have the same vector form as the extremal equation of the LinPos problem [Eq. (111)] with the vector $\mathbf{R}$ replaced by

$$R_i^{(\text{Poisson})} = \frac{\bar{n}_0}{\sum_{j'} c_{ij'} n_{j'}} \sum_j c_{ij} \exp\left(- \sum_{i'} \mu_{i'} c_{i'j} \right). \tag{114}$$

When the input intensity $\bar{n}_0$ is not known, it should be estimated, too:

$$\bar{n}_0 = \sum_j n_j \Big/ \sum_j \exp\left(- \sum_i \mu_i c_{ij} \right). \tag{115}$$

As seen, the Poissonian tomography is intrinsically a nonlinear problem. This has serious consequences for the convergence properties of the iterative algorithm [Eqs. (111) and (114)]. Instead of converging to a stationary point, it might end up in oscillations. Typically, such convergence problems arise in the presence of very noisy data. When this happens, it is necessary to decrease the size of the iteration step as follows: $R_i \to R_i^\alpha$, $i = 1, \ldots, M$, $0 < \alpha < 1$. Of course, any solution to the regularized problem is also a solution to the original problem.

C. Comparison with Standard Methods

In real experiments, many factors could influence the quality of the measured data and therefore also the result of the tomography. Misalignments present

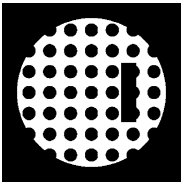

FIGURE 16. The object.

in the experimental setup, instability of the illuminating beam, white spots, and damaged detector pixels can be such factors, to name a few. To avoid this problem, let us first show a few simulations. The data were generated on a computer from the artificial object shown in Figure 16. It is a circle composed of a homogeneous material with many small round holes drilled through it. One additional rectangular piece of material was removed from the circle to make it less symmetric. The absorption index of the material was chosen in such a way that the maximum attenuation along a beam was close to 50% of the input intensity.

In the simulations, the object was subject to five different experiments. Their parameters are summarized in Table 2. The first four experiments (a–d) correspond to the ideal situation of a very high beam intensity where the Poissonian detection noise can safely be ignored. The last reconstruction simulates more realistic conditions with 2000 counts per pixel in the open beam. Notice that a relatively small number of rotations is chosen for all five experiments. In this regime the inverse Radon transformation is expected to yield bad results, and the improvement of the ML tomography on the standard technique should be most prominent. This regime is also important from the practical point of view. Doing more rotations implies a longer measurement time and more radiation absorbed by a sample. The latter may be an important factor if the imaging of biological samples is considered.

TABLE 2
QUALITY OF THE INPUT DATA*

Reconstruction	Angles	Pixels	Intensity
a	13	161	∞
b	19	101	∞
c	20	101	∞
d	7	301	∞
e	15	161	2000

* The last column shows the mean number of counted particles per pixel in the incident beam.

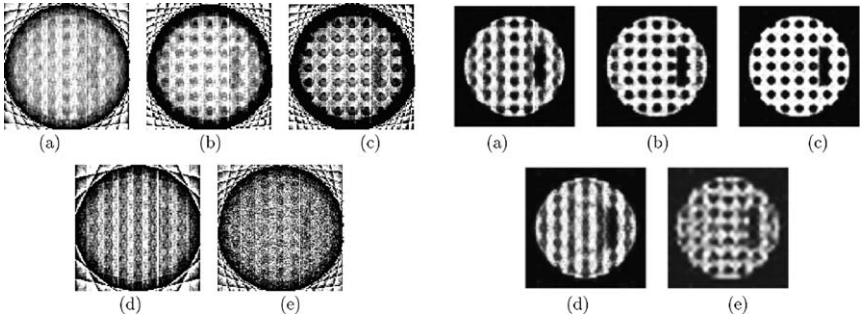

FIGURE 17. Left panel: IDL reconstructions from the simulated data (for parameters see Table 2). Right panel: ML reconstructions from the same data; the iterative algorithm Eqs. (111) and (114) has been used for reconstruction.

Provided the improvement of the reconstruction technique gives comparable resolution with less data, imaging costs and damage done to a sample due to radiation might be reduced.

Reconstructions from the simulated data are shown in Figure 17 (Řeháček *et al.*, 2002). The simulated data were first processed using the IDL imaging software (Research Systems Inc.), which implements the standard FBP algorithm (inverse Radon transformation) (see the left panel in Figure 17). This software is one of the industrial standards in computer-assisted tomography. The same data were then processed using the iterative algorithm based on the maximization of the Poissonian likelihood function (see the right panel Figure 17). In the absence of noise (see cases [a]–[d]), the fidelity of a reconstruction depends on two main factors—the spatial resolution of the detector, and the number of rotations used. It is apparent from Figure 17 that the latter factor is the more important of the two. Very small number of angles cannot be compensated by an increased spatial resolution of the detector (for example, compare cases (c) and (d)), and reconstruction (d) is by far the worst one. However, ML tomography is much less sensitive to the number of angles than the standard filtered back-projection. Even the large rectangular hole in the object is barely perceptible in the IDL reconstruction (d) in Figure 17, whereas it shows nicely in the ML reconstruction from the same data. ML reconstructions also are superior to the standard ones in cases (a)–(c); notice that the ML reconstruction (c) that is based on as few as 20 different angles is nearly perfect.

Benefits of ML tomography are fully revealed when the detected data are noisy (case (e) in Table 2). Standard filtered back-projection applied to noisy data faces serious difficulties. This is due to ill-posedness of the Radon transformation where data are integrated with a singular filter function.

Obviously such deconvolution greatly amplifies any noise present in the data. With little or no prior information available about the object, it is difficult to tell true details of the object from artifacts. ML tomography provides much better results. Since noises are incorporated into the algorithm in a natural and statistically correct way, artificial smoothing is not needed. Notice in simulation Figure 17(e) that the noisy data yield a slightly distorted but otherwise clear image through the ML algorithm, unlike the corresponding very noisy standard reconstruction. This is a nice feature of the intrinsically nonlinear ML algorithm, which, in the course of reconstruction, self-adapts to the registered data and always selects the most likely configuration.

D. Imaging of Strongly Absorbing Materials

One specific application of neutron CT imaging is the quantitative analysis and 3D visualization of the ^{10}B isotope distribution in boron alloyed steel. Boron alloyed steel is used in nuclear engineering as neutron shielding for the radioactive waste disposal equipment, such as components for the compact fuel storage racks and transportation baskets. The main demand on the sheets for these applications is, besides mechanical stability and corrosion resistance, the largest possible thermal neutron attenuation, which must be uniform over the whole volume. The attenuation in the steel depends mainly on the ^{10}B isotope, which has a large attenuation cross section for thermal neutrons $\sigma_{th}(^{10}B) = 3838.1(10) \times 10^{-24}$ cm^2 (Sears, 1992).

Imaging of strongly absorbing samples suffers from the beam hardening effect. The wavelength dependence of scattering cross section [Eq. (59)] causes a spectral change of the neutron flux in the sample, where preferably low-energy neutrons are absorbed so that the remaining beam becomes richer in high-energy neutrons. In addition to this effect, the following specific difficulties occur with strong absorbing materials:

- The exposure time for one projection is several minutes and the total measurement time for one tomographic data set lasts several hours. If the data are analyzed with the FBP algorithm, one depends on a stable operation of the neutron source and CCD detector.
- The low count numbers lead to increased statistical fluctuations, which become amplified in the FBP reconstruction.
- The imaging quality depends strongly on low background conditions. The contribution of scattered thermal neutrons, fast neutrons, gammas, and light penetration in the detector box must be suppressed as must as possible.
- The stronger the attenuation in the sample, the more the result will interfere with the choice of input parameters in the FBP routine.

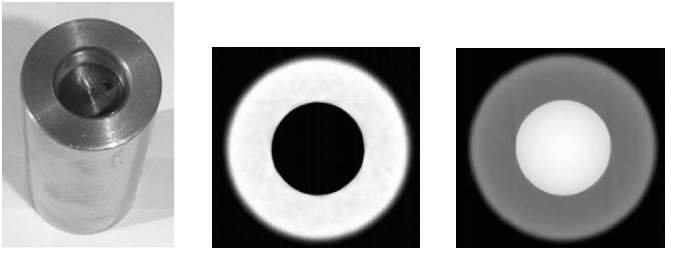

(a) (b) (c)

FIGURE 18. Measured steel sample. This is a two-component system, which consists of an outer ring (Ø = 2 cm), partly filled with a second rod with 68% enlarged boron content (Ø = 1 cm). Expected distribution of the absorption index in the upper hollow (b) and lower filled (c) regions are also shown (Zawisky *et al.*, 2004b).

All these reasons clearly favor ML statistical inversion over the deterministic FBP algorithm.

Let us show some examples of the tomographic investigations of strong absorbers that were performed at the 250 kW TRIGA reactor of the Vienna Atominstitute, where at a well-thermalized beamline, a neutron-tomography facility had been implemented (Koerner *et al.*, 2001). Surprisingly, neutron tomography of strong absorbers is still possible with weak beam intensities of about 10^5 n/cm^{2}s. High-resolution camera optics with the nominal resolution of 80 μm was used (Koerner *et al.*, 2001). During the experiment, only a few neutrons per second per pixel were registered. Naturally, the discrete character of the quantum signal plays an important role at such low intensities.

The measured sample (Figure 18) was a two-component system consisting of a ring with an outer diameter of 2 cm and a hole of 1 cm diameter. The hole was partially filled with a second rod of 1 cm diameter with somewhat larger ^{10}B content.

First we will show some typical results obtained with the standard FBP algorithm (Figure 19). Notice that despite a large number of projections (angles) that were used for the inversion, the reconstructions are still rather noisy. Also, the reconstructed absorption profiles are far from those expected. This is caused partly by the previously mentioned beam-hardening effect that was not taken into account here.

Figure 20 illustrates the usefulness of the ML technique in cases where only a few projections are available. The reconstructions are based on the same experimental data as the corresponding Figures 19(a) and 19(b). However, the number of projections was reduced from 50 to just 10 (!) projections. In this extreme case the filtered back-projection fails completely. It is interesting to notice that although no correction of the beam-hardening effect was done during the ML reconstruction, the reconstructed density profiles resemble

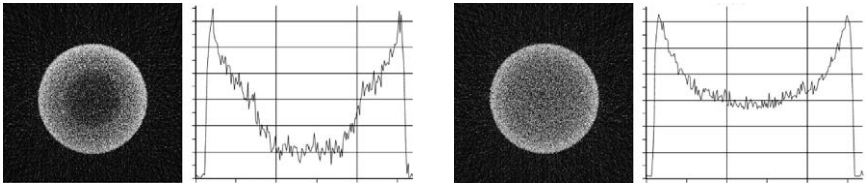

FIGURE 19. FBP reconstructions of the sample shown in Fig. 18. Fifty different projections were used. (a) A typical reconstructed cut through the upper region, where instead of the second rod only an air hole is inside the ring. (b) A typical reconstructed cut through the middle region, where the second steel rod with higher boron content is inside the ring. The noise in the profile plots was suppressed by averaging over several tens of reconstructed slices.

the true density profiles more closely than the corresponding FBP profiles shown in Figure 19. In addition, the quality of the ML reconstruction from 10 projections is not inferior to FBP results obtained from data sets that are five times larger. A proper statistical treatment extracts more information from the measured data than do the standard reconstruction methods. In this way, the measurement time can be significantly reduced without loss of resolution. Still better results can be expected provided the beam hardening is incorporated into the physical model.

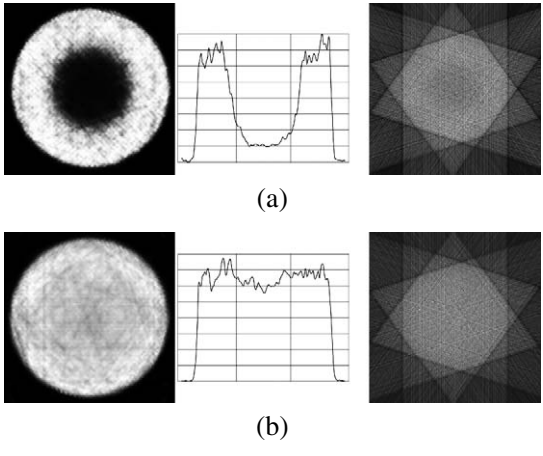

FIGURE 20. Reconstructions of the sample of Figure 18 from only 10 (!) projections; panels (a) and (b) correspond to slices shown in Figures 18(b) and 18(c), respectively. Left: ML reconstructions; middle: ML profiles; right: standard FBP interpretation of the same data is shown for comparison.

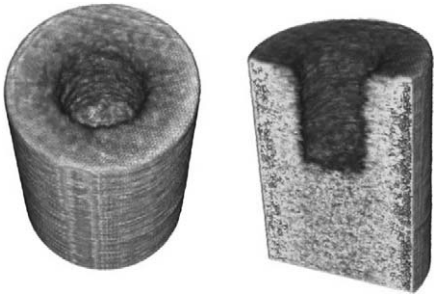

FIGURE 21. ML reconstruction from only 10 projections and 3D rendering of the boron alloyed steel composite shown in Figure 18. The result is even better than the FBP reconstruction from 50 projections (Figure 19), but without beam-hardening correction, the inner rod with higher ^{10}B content cannot be extracted from the surrounding steel.

VI. PHASE TOMOGRAPHY WITH LOW-INTENSITY NEUTRON BEAMS

This section adapts the ML estimation to more sophisticated tomographic schemes. The conceptual difference between the standard deterministic and ML statistical inversions can be nicely illustrated on the example of nPCT. Standard nPCT consist of two separate steps. First, each set of interferograms is processed to obtain the distribution of the total phase accumulated in the j-th scan; this total phase is an integral of the unknown index of refraction along the j-th beam path. In this way, the original problem is reduced to the conventional tomographic imaging, and hence the inverse Radon transformation of the accumulated phase yields the distribution of the index of refraction within the object.

This straightforward procedure suffers from all known shortcomings of the standard FBP routine, which are further accentuated in nPCT by still smaller measured intensities and thus increased fluctuations. Additional problems arising in the standard nPCT are caused by using the accumulated phases as the starting point for tomographic reconstruction. Due to the high phase sensitivity it is very likely that some of the projected (accumulated) phases will exceed 2π phase interval. The correction of these "phase jumps" becomes virtually impossible if the data are very noisy.

Most of these problems can be avoided when the ML statistical inversion is adopted. Here, the object is decomposed into many elementary cells, each of which shifts the phase of the overlapping beam by only a fraction of the 2π phase window. Thus, the phase value of each cell is uniquely defined. Then we look for such distribution of those elementary phases that is most likely

from the point of view of registered data. In this way, phase estimation and tomographic reconstruction are done simultaneously.

A. *Phase Estimation*

Let us first discuss phase estimation in the context of nPCT. Consider an interferometric measurement with mean intensity N and amplitude V. The interference pattern,

$$\bar{n}_\alpha = N + V\cos(\theta + \delta_\alpha), \tag{116}$$

will be scanned with L different settings of the auxiliary phase shifter uniformly distributed over the 2π phase window,

$$\delta_\alpha = \alpha\frac{2\pi}{L}, \quad \alpha = 0, 1, \ldots, L-1. \tag{117}$$

Interference pattern Eq. (97) is just a special case of Eq. (117) corresponding to $L = 4$ phase shifts.

When the measurement is completed, all the accumulated information can be expressed as an *a posteriori* likelihood function. It is essential that the likelihood includes all measured data, and, together with the physical model for the detection probabilities, all experimental evidence. Thus, the likelihood is the optimum starting point for a complete tomographic analysis.

Ideally, the only fluctuating quantity in the tomographic measurement is the counted number of particles. The fluctuations produced by thermal sources such as nuclear reactors are well described by the Poissonian statistics, which was confirmed in several experiments (Rauch *et al.*, 1990; Zawisky *et al.*, 1994). Since the detections with different settings δ_α are independent, the joint probability of registering data $\mathbf{n}$ is simply a product

$$\mathcal{L} = \prod_\alpha \left(\bar{n}_\alpha^{n_\alpha} e^{-\bar{n}_\alpha}/n_\alpha!\right). \tag{118}$$

This is also the likelihood of the given value θ of the unknown phase shift.

In accordance with the ML principle, we will take the maximum likely phase as the inferred value of θ. Since the amplitude V and the total mean number of particles N are not under the experimenter's control and may vary from one pixel to another, these parameters should be estimated together with phase. Their values are found by maximizing function [Eq. (118)] or its logarithm. The latter in the case of uniformly distributed auxiliary phase shifts simplifies to

$$\log\mathcal{L} \propto \sum_\alpha n_\alpha \log\left[N + V\cos(\theta + \delta_\alpha)\right] - NL + \text{const.} \tag{119}$$

Now it is convenient to introduce new variables $x = V\cos\theta$ and $y = V\sin\theta$. We are looking for the point where the likelihood has zero slope: $\partial\mathcal{L}/\partial x = \partial\mathcal{L}/\partial y = \partial\mathcal{L}/\partial N = 0$. From Eq. (119) we determine the following extremal equations:

$$\sum_{\alpha} \frac{n_\alpha \mathbf{X}}{N + x\cos\delta_\alpha - y\sin\delta_\alpha} = 0, \quad \mathbf{X} = (\cos\delta_\alpha, \sin\delta_\alpha, 1). \tag{120}$$

In general, these equations must be solved numerically. Closed-form solution can be found only in some special cases such as $\alpha = 3$ and $\alpha = 4$.

A particularly simple solution exists for three auxiliary phases, when the maximum of the Poissonian likelihood in (118) coincides with the maximum of its Gaussian approximation,

$$\mathcal{L} \propto \exp\left[-\frac{1}{2\sigma^2}\sum_{\alpha}(n_\alpha - \bar{n}_\alpha)^2\right], \tag{121}$$

yielding

$$x = \frac{2}{L}\sum_{\alpha=0}^{2} n_\alpha\cos(-\delta_\alpha), \qquad y = \frac{2}{L}\sum_{\alpha=0}^{2} n_\alpha\sin(-\delta_\alpha), \qquad N = \frac{1}{L}\sum_{\alpha=0}^{2} n_\alpha. \tag{122}$$

These, going back to the original variables, can be written in the following compact form (Řeháček *et al.*, 1999)

$$V = 2|R|/L, \qquad e^{i\theta} = R/|R|, \tag{123}$$

where

$$R = \sum_{\alpha=0}^{2} n_\alpha e^{-i\delta_\alpha}. \tag{124}$$

This quantity can be interpreted as the first coefficient of the discrete Fourier transformation of the registered counts n_α (Walkup and Goodman, 1973).[1]

Therefore it is particularly useful to use three auxiliary phase shifts, for in that case, the optimal phase estimation is easily handled by means of the simple formula in Eq. (123).

B. Reconstruction Algorithm

In nPCT, phase-sensitive data $n_{j\alpha}$ are registered. Subscripts j and α label scans (i.e., pixels of the CCD camera and rotations of the sample) and

[1] In a sense, Eq. (123) is a generalization of the operational phase Eq. (53) of Noh, Fougères, and Mandel.

auxiliary phases, respectively. As each scan contributes likelihood [Eq. (121)] and different scans are independent observations, the total log-likelihood reads

$$\log \mathcal{L} \propto \sum_j \sum_\alpha (n_{j\alpha} - \bar{n}_{j\alpha})^2 + \text{const.}, \tag{125}$$

where the mean number of particles detected in the j-th projection is given by

$$\bar{n}_{j\alpha} = N_j + V_j \cos\big(\theta_j + \delta_\alpha + \theta_j^r\big). \tag{126}$$

Here θ_j is the total phase accumulated along the j-th projection, $\theta_j = \sum_i c_{ji}\mu_i$. Coefficients c_{ji} are the overlaps between the j-th projection and the i-th elementary cell of the reconstruction mesh, as before (see Figure 7), and θ_j^r are the reference phases describing the phase properties of the empty interferometer. The latter can be estimated from the same set of projections measured without the sample. Likelihood [Eq. (125)] is to be maximized over the distribution μ_i of the optical density of the sample.

In neutron phase imaging, μ is composed of the sum of all scattering length densities (Nb) of the isotopes contained in the sample:

$$\mu = -\lambda \sum_l N_l b_l = -\lambda \sum_l \frac{N_A \rho_l b_l}{A_l} \tag{127}$$

(see also Section III). Here N_l represents the number of isotopes l per unit volume, ρ_l the isotope density, N_A the Avogadro constant ($6.02214199(47) \times 10^{23}$ mol^{-1}), and A_l the atomic weight. Note that most isotopes have positive coherent scattering lengths b_l but some are known with $b_l < 0$. The existence of positive and negative phase shifts (in the latter case, the index of refraction is less than one) is a specialty of neutron optics and can be used for fading out unwanted phase contributions.

A necessary condition for the maximum of $\log \mathcal{L}$,

$$\frac{\partial \log \mathcal{L}}{\partial \mu_i} = 0, \quad \forall \mu_i, \tag{128}$$

yields on using Eqs. (125) and (126) the following set of extremal equations,

$$\mu_i = \mu_i \frac{\sum_j V_j c_{ji} \sin\theta_j \,\mathrm{Im}\{R_j\}}{\sum_j V_j c_{ji} \cos\theta_j \,\mathrm{Re}\{R_j\}}. \tag{129}$$

These can be solved numerically by repeated iterations.

1. *Reference Phase Measurement*

No interferometers are perfect. Already an empty interferometer shows a nonuniform transversal distribution of phase difference between its two arms. To remove this background phase the measurement is done in two steps: with and without the sample. The simplest way to subtract the background phase is to perform two separate phase reconstructions, then subtract the reconstructed background phase from the reconstructed phase of the sample. This procedure is simple, but not optimal. It is not difficult to see why. An inspection of Eq. (129) shows that the reconstructed indexes of refraction μ_i depend on the amplitudes V_j of the registered interference fringes. This is natural since the reconstruction is a synthesis of many phase measurements and phases measured under higher visibilities and neutron numbers are less affected by the noise and hence more credible. For the same reason the phase introduced by an empty interferometer is measured more accurately than the phase introduced by interferometer *and* sample. This additional knowledge should be incorporated into the reconstruction routine. Denoting $\theta = \theta_s + \theta_r$ the total phase measured with the sample, which is the sum of the reference phase and the phase introduced by the sample θ_s, and using Eqs. (123) and (124) in Eq. (121) we can rewrite the posterior distributions of θ and θ_r in the following compact form:

$$P(\theta) \propto e^{V\cos(\theta-\theta_{\mathrm{NFM}})} \tag{130}$$

$$P(\theta_r) \propto e^{V_r\cos(\theta_r-\theta_{r,\mathrm{NFM}})}. \tag{131}$$

NFM denotes Gaussian (semi-classical) phase estimates that maximize posterior distributions [Eqs. (130) and (131)], which are also known as von Mises normal distributions defined on the unit circle. As mentioned above, their widths are determined by the corresponding amplitudes. Since we are interested only in phase θ_s introduced by the sample alone, let us calculate its posterior distribution,

$$P(\theta_s) = \int\int P(\theta)P(\theta_r)\delta(\theta-\theta_r-\theta_s)\,d\theta_r\,d\theta. \tag{132}$$

The double integrations can be easily carried out, and the result expressed in terms of the Bessel function I,

$$P(\theta_s) \propto I_0\Big(\sqrt{V^2+V_r^2+VV_r\cos(\theta_s-\theta_{-,\mathrm{NFM}})}\Big), \tag{133}$$

where $\theta_{-,\mathrm{NFM}} = \theta_{\mathrm{NFM}} - \theta_{r,\mathrm{NFM}}$. Optical density of the sample can now be estimated by maximizing the posterior distribution Eq. (133) with respect to indexes μ_i. Such procedure accounts for the reference phases in an optimal way.

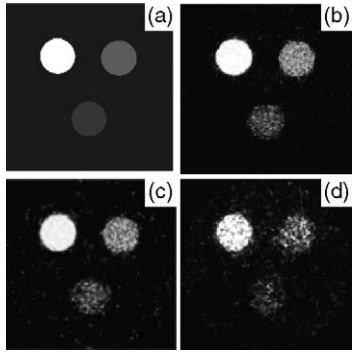

FIGURE 22. Simulated phase tomography with a weak neutron signal. The maximal accumulated θ_j in the three cylinders making up the object (a) are 150 degrees, 50 degrees and 30 degrees for white, light gray, and dark gray, respectively. The mean count numbers per pixel and visibilities are (b) $N = 450$, $V/N = 33\%$; (c) $N = 150$, $V/N = 33\%$; and (d) $N = 30$, $V/N = 33\%$.

C. Simulations

Figure 22 shows a simulation of a nPCT experiment with various intensities and visibilities of the illuminating beam. The artificial object was scanned from 31 different angles with a resolution of 81 pixels.

Case (d) is the most interesting one. Here the incident beam has such a low intensity that its Poissonian fluctuations are comparable to the intensity changes caused by the maximal phase shifts in the light gray and dark gray cylinders. The useful phase information is thus almost lost in the background noise, yet all three cylinders nicely show in the reconstruction.

Another example of the ML phase tomography is shown in Figure 23. The parameters of the simulated experimental setup are comparable to that of Figure 22, but now the maximal phase shift in the sample is well in excess of 4π radians. *A priori* knowledge about the shape and high index of refraction

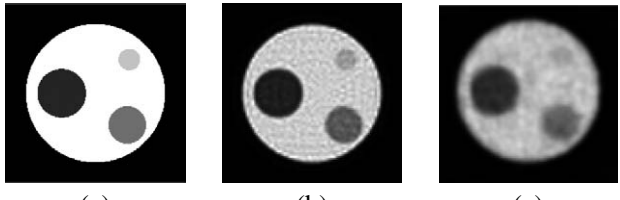

FIGURE 23. Simulated phase tomography with a weak neutron signal, $N = 150$ and $V/N = 33\%$. The maximal accumulated θ_j in the object is 4.2π rad. (a) The artificial object; the ratio of the index of refraction in the white, light gray, dark gray, and black cylinder is $1 : 0.8 : 0.5 : 0.2$. (b) ML reconstruction from 31 angles and 81 pixels. (c) ML reconstruction from 21 angles and 41 pixels.

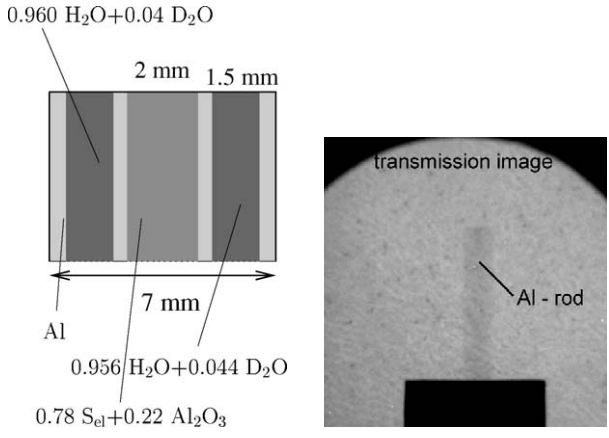

FIGURE 24. Side view of the measured sample: (a) schematic picture; (b) conventional transmission image.

of the white container could be easily incorporated into the reconstruction, and as a result the internal structure of the object was nicely resolved.

D. Applications of Neutron Phase Tomography in Isotope Analysis

A similar isotope gauge, a mixture of S33 + S34 and $H_2O + D_2O$ isotopes, has recently been investigated at the nPCT setup in the Institute Laue-Langevin in Grenoble (Zawisky *et al.*, 2004a) in order to test the method and verify its sensitivity and spatial resolution under realistic conditions.

The test object was an aluminum rod of 7 mm diameter with three cylinders drilled in, filled with different isotope mixtures (Figure 24(a)). The central cylinder was filled with the mixture of 78% of elemental sulphur and 22% of aluminum oxide. The two smaller side holes were filled with two different water mixtures: 96% H_2O+4% D_2O and 95.6% H_2O+4.4% D_2O. Notice that both the sulfur isotopes and the aluminum are nearly transparent to thermal neutrons and therefore invisible in conventional transmission tomography shown in Figure 24(b).

In contrast to this, a sensitivity in detecting nuclear density differences at a 1% level has been confirmed in the phase analysis, with a spatial resolution of 50 μm in the phase projections.

Tomographic reconstructions from the measured phase sensitive data are summarized in Figure 25. Panel (a) is a picture of the top of the sample showing its true geometry. For the reconstruction, 30 different projections

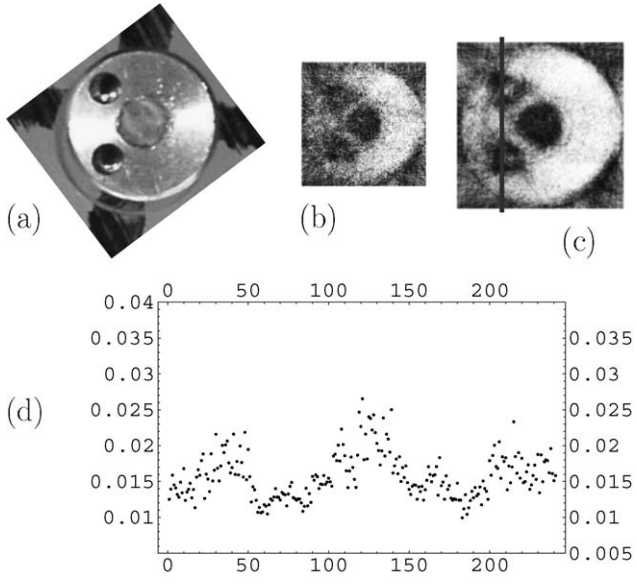

FIGURE 25. Experimental maximum-likelihood nPCT: (a) top view of the sample; (b) typical reconstruction of a single 50 μm thick slice; (c) the same as (b) but data from 10 adjacent slices were collected prior to reconstruction; (d) line profile of the reconstructed scattering density (in arbitrary units) along the direction indicated in (c).

were measured with the transversal resolution of about 150 pixels per the width of the aluminum rod. Intensity in the region of interest was extremely low, typically below 30 counts per pixel. Small number of projections together with low intensity and small visibility (caused by scattering effects) make the data inversion a challenge for any reconstruction technique.

Panel (b) in Figure 25 shows a typical ML reconstruction of a single 50 μm thick sample slice. Although the noise in the image is rather large, one can easily distinguish the geometry of the object. Still better results were obtained by using data averaged over 10 adjacent slices for the reconstruction (with the corresponding vertical resolution of 0.5 mm). In this way, the signal-to-noise ratio was somewhat increased. The resulting reconstruction is shown in Figure 25(c). The last panel (Figure 25[d]) shows the line profile of the reconstructed scattering density along the direction indicated by the vertical line in Figure 25(c). The average scattering density in the two water isotope mixtures differs only by 10%, well in accordance with the expected values from the sample preparation. This relates to a sensitivity of 4×10^{-3} in the detection of D_2O differences in the mass fraction.

Finally, let us stress that we applied our algorithm to raw measured data without any prior filtering. The appearance of some artifacts in the

reconstructed images (white specks inside the water cylinders) is probably caused by not considering scattering effects. However, on the whole, given the extreme experimental conditions and small number of measured projections, the reconstructions can be considered successful. Further enhancements can be expected after developing more accurate physical model of the experiment and applying appropriate filters prior to reconstruction.

E. Tomography of the Complex Refractive Index

Tomography of absorption index and phase shift may be accomplished simultaneously provided that the detected signal is sensitive to these values. For the purpose of numerical simulations, let us insert the sample in the arm of an ideal interferometer. Its presence will be manifested by the phase shift of interference fringes and the loss of the visibility. The position of interference fringes yields information about the real part of the index of refraction while the loss of visibility indicates the absorption.

Denoting the signal induced along the k-th path in the sample as

$$\bar{n}_j = \frac{1}{4}\left[1 + Q_j Q_j^* + Q_j + Q_j^*\right], \tag{134}$$

where the complex parameters are introduced as $q_i = \exp(-\mu_i^2 + i\phi_i^2)$, $Q_j = \prod_i (q_i)^{c_{ji}}$. Here the absorption ν_j^2 and phase shift ϕ_j^2 are explicitly constrained to positive values. The corresponding log-likelihood is

$$\log \mathcal{L} = \sum_j n_j \log \bar{n}_j - \sum_j \bar{n}_j, \tag{135}$$

where n_j are the corresponding detected values. Extremal equation $\partial \mathcal{L}/\partial q_i = 0$ then in complex notation reads

$$\sum_j \left[\frac{n_j}{\bar{n}_j} - 1\right]\left[Q_j^* Q_j + Q_j\right] c_{ji} = 0 \tag{136}$$

for each i. This equation may be solved by iterating the variables μ_j, ϕ_j in accordance with the equations

$$\mu_i^{(p+1)} = \mu_i^{(p)} - \sum_j \left[\frac{n_j}{\bar{n}_j} - 1\right]\left[2Q_j^* Q_j + Q_j + Q_j^*\right] c_{ji} \mu_i^{(p)} \tag{137}$$

$$\phi_i^{(p+1)} = \phi_i^{(p)} + 2i \sum_j \left[\frac{n_j}{\bar{n}_j} - 1\right]\left[Q_j - Q_j^*\right] c_{ji} \phi_i^{(p)}. \tag{138}$$

Numerical simulations demonstrate the feasibility of such a reconstruction.

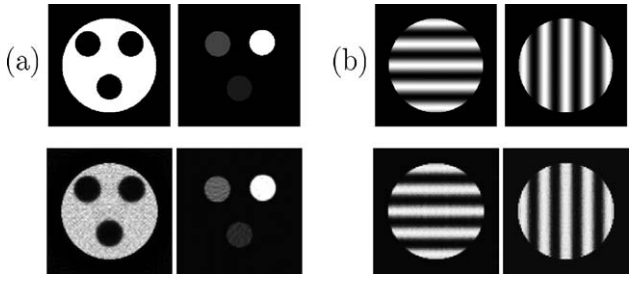

FIGURE 26. Simulated tomography of the complex index of refraction.

The proposed method for the reconstruction of the complex index of refraction can be illustrated by means of computer simulations. Figure 26 shows reconstructions from noiseless data in the limit of very large input intensities. The only source of reconstruction error in this case is the rather small discretized set of measurements. For our reconstruction we simulated measurement of 30 different scans (angles) with the spatial resolution of 100 pixels. Two different samples, Figures 26(a) and 26(b), were simulated. The upper row of Figure 26 shows the true distributions of the absorption index (on the left) and index of refraction (on the right). The bottom row shows the corresponding reconstructions. Sample (a) consists of material with either nonzero real refraction index or nonzero imaginary refraction index, but not both. Both distributions are piecewise constant. Sample (b) shows periodic ($\propto \cos^2$) variations of absorption and refraction with perpendicularly oriented wave vectors. The maximal values of refraction and absorption in both samples were set in such a way that the maximal absorption was about 50% of the input intensity and the maximal phase shift induced by the sample was about π rad. Despite the rather small number of used projections and pixels, the reconstructed profiles are very close to the true ones. This shows the robustness of our method with respect to binning and sampling.

Reconstruction of Figure 26(b) from noisy data is shown in Figure 27. Here, the calculated theoretical signal in Eq. (134) was used as a mean for a Poissonian random number generator. The intensity was set to 100

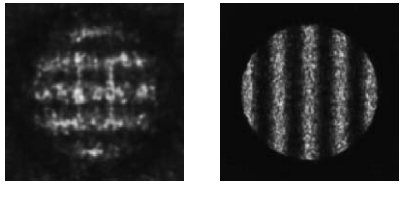

FIGURE 27. Simulated tomography of the complex index of refraction.

particles. The typical counts per pixel were in the range of 10–50 particles due to absorption and destructive interference. Such extremely weak signal exhibits strong fluctuations, which makes it a good test for any reconstruction method. The conditions during a real experiment would certainly be more favorable. From the result (Figure 27) it is apparent that the reconstruction of the absorption index is more sensitive to noise that the reconstruction of refraction index. This is not surprising as absorption enters our data only through the visibility, which is more difficult to estimate than a phase shift (Řeháček *et al.*, 1999).

F. Beyond Phase Tomography

Phase tomography discussed in the previous section is a simple example of quantum-process tomography. In this case, the process is a unitary operation that can be represented by a 2D rotation. The rotations vary in space, and the detected particles probe their spatial distribution via quantum interference.

Obviously, more complex probes are needed to "see" more complicated transformations. It would be logical to proceed the exposition with the case of spin $1/2$ systems whose Hilbert space could be associated with the 3D Bloch sphere. The synthesis of measurements—projections—is able to determine an unknown quantum state, and such procedure possesses all the features of quantum tomography of the internal spin state. The ML approach can be straightforwardly applied here. This was worked out explicitly by Hradil *et al.* (2000) for the representation of the spin using the polarization vector.

Because the magnetic momentum of particles is coupled to the magnetic field, spin state tomography can be used as a means (e.g., for nondestructive investigations of the magnetic domains of bulk materials). Here the beam of polarized neutrons goes through the specimen, interacting with its magnetic domains. Due to this interaction, the spin state of the neutrons changes, and this depolarization can be used for the visualization of the magnetic domains in the specimen, just as in the case of phase tomography. However, the probed operations are now represented by rotations in 3D space, which unlike 2D rotations in phase tomography, form a non-Abelian group of transformations. Consequently, the tensorial character of the corresponding depolarization observable together with the noncommutativity of rotation matrices makes the analysis rather involved. Although this is a challenging question with potential interesting applications, at present no analytical solution of this inverse scattering problem is known. To date, there are several approaches based on deterministic techniques, but the ML solution has not been devised yet.

VII. Three-Beam Interference and Which-Way Information in Neutron Interferometry

The next three sections are devoted to exploiting the genuine quantum properties of neutrons for imaging purposes. For example, the concept of wave particle duality reviewed in Section III.E tells us that the principal availability of information about the path a neutron takes in a Mach–Zehnder interferometer will destroy the interference. In principle, objects or fields placed inside the interferometer can act as (imperfect) which-way detectors. Thus, from the registered interference patterns one can learn something about the measured objects through their which-way detection capabilities.

Duality measurements are discussed in detail in this section. A more sophisticated scheme using the QZE is presented in Section VIII. Aside from duality effects, the loss of coherence can also be due to the interaction of particles with a noisy environment. The analysis of statistical fluctuations by means of neutron interferometry is considered in Section IX.

A. *Duality Measurement in the Two-Loop Interferometer*

The two-loop interferometer offers an elegant method of manipulating and simultaneously measuring the neutron's duality. Here the first interferometer loop can be used to manipulate the which-way information while the second loop serves for visibility measurements (Figure 28). The which-way tuning is achieved by the unitary transformations $e^{-i\alpha_1}$, $e^{-i\alpha_2}$ in the first interferometer loop, which modulates the intensity in path II,

$$\bar{I}_{\mathrm{II}}(\Delta\alpha) \propto \left[1 + V_i \cos(\Delta\alpha)\right]. \tag{139}$$

Then, according to Eqs. (64) and (65), predictability and visibility are solely modulated by $\Delta\alpha$. The intensity in path I is not affected by the phase shifts and remains always constant. Therefore I_{II} and P can be derived from the total count numbers in O+H simultaneously with the visibility measurements without disturbing the interference experiment.

It should be emphasized that no net momentum is transfered to the neutrons detected in output O, and no essential dephasing occurs in this specific arrangement of phase shifters. This demonstrates that the access to path information does not exclusively rely on the position-momentum uncertainty relation or on dephasing.

B. *Three Beam Interference*

In the two-loop interferometer three interfering beams are generated with different phases $\alpha_{1,2}$, $\gamma_{1,2}$. In the ideal two-loop interferometer again only the

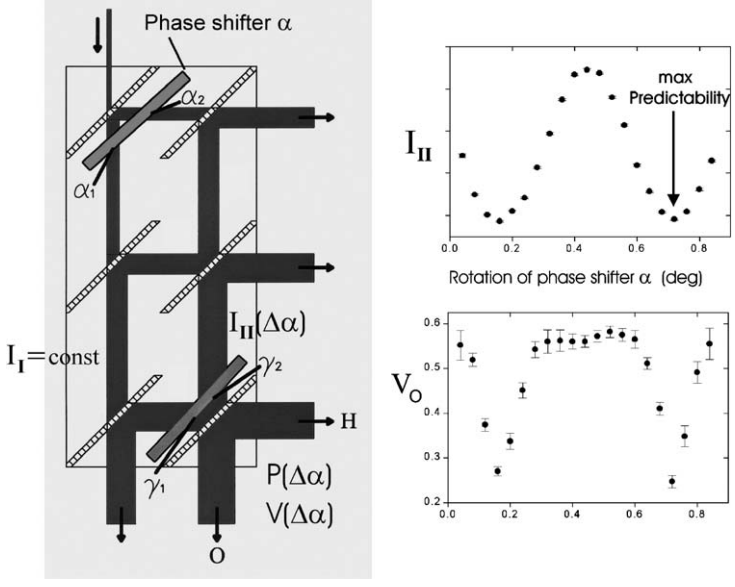

FIGURE 28. Simultaneous "interaction-free" measurement of duality. The first interferometer loop serves for intensity tuning in path II, which solely depends on the phase difference $\Delta\alpha = \alpha_1 - \alpha_2$ induced by the phase shifter α. The intensity in path I is not affected by such coherent phase manipulations. In the second interferometer loop, the visibility is affected by an intensity asymmetry $|I_{\rm I} - I_{\rm II}|$. Thus, predictability and visibility both depend solely on phase differences in the first loop. If $\Delta\alpha$ reaches 180 degrees, then $I_{\rm II}$ becomes zero, or reaches its minimum in the real experiment, and all neutrons detected in output O, H, must have taken path I. This path information reduces the visibility as shown in the right plot. $P(\Delta\alpha)$ and $V(\Delta\alpha)$ can be measured simultaneously at the output ports O, H without disturbing the quantum state inside the interferometer. The visibility is measured with the second phase shifter γ in loop 2 (Zawisky *et al.*, 2002).

O-beam can reveal full visibility ($V_{\rm O,max} = 1$) because the three interfering beams have the same amplitudes,

$$\begin{aligned} I_{\rm O} &= |rrtt|^2 \left| e^{-i(\alpha_1+\gamma_1)} + e^{-i(\alpha_2+\gamma_2)} + e^{-i(\alpha_1+\gamma_2)} \right|^2 \\ &= |rrtt|^2 \big(3 + 2\big(\cos(\Delta\alpha + \Delta\gamma) + \cos(\Delta\gamma) + \cos(\Delta\alpha)\big)\big) \\ &= |rrtt|^2 \big(3 + 2\cos(\Delta\alpha) + 4\cos(\Delta\alpha/2)\cos(\Delta\alpha/2 + \Delta\gamma)\big). \quad (140) \end{aligned}$$

$I_{\rm II,O}$ and consequently $V_{\rm O}$ are then modulated by phase differences $\Delta\alpha$,

$$V_{\rm O}(\Delta\alpha) = \frac{4\cos(\Delta\alpha/2)}{3 + 2\cos(\Delta\alpha)}. \quad (141)$$

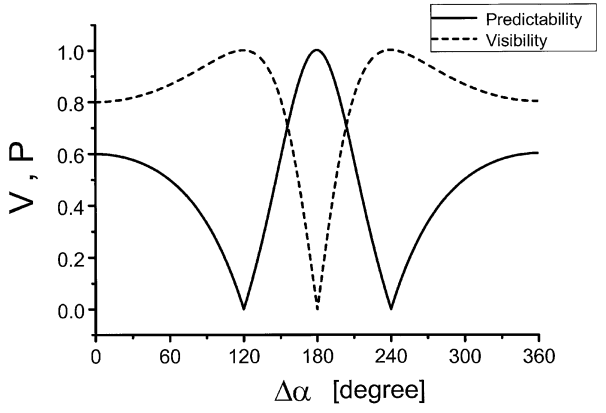

FIGURE 29. Coherent duality manipulations in the ideal two-loop interferometer by using three interfering beams. $P_O^2 + V_O^2 = 1$ is fulfilled for all $\Delta\alpha$ (Zawisky, 2004).

The predictability that the intensity detected in O comes either from path I or II is

$$P_O = \left| \frac{I_{I,O} - I_{II,O}}{\bar{I}_O} \right| = \left| \frac{1 - 2(1 + \cos \Delta\alpha)}{1 + 2(1 + \cos \Delta\alpha)} \right|. \tag{142}$$

Figure 29 shows the strict duality of visibility and predictability in the ideal two-loop interferometer where $P_O^2 + V_O^2 = 1$ holds for all $\Delta\alpha$. At $\Delta\alpha = 180$ degrees, the predictability reaches its maximum and V_O becomes zero. Then $I_{O,II}$ becomes zero and all intensity in O stems from path I. At $\Delta\alpha = 120$ and 240 degrees, the visibility reaches its maximum and all path information vanishes.

The duality experiments have been performed at the interferometer instrument S18 at ILL-Grenoble. The variation of $\Delta\alpha$ was achieved by an aluminum phase shifter whose beam attenuation is negligible. Furthermore, the small remaining absorption probability is equal in both beams and cannot influence the path information. The second nonabsorbing phase shifter $\Delta\gamma$ (silicon, thickness 5 mm, transmission 99.4%) allows the derivation of the visibility in the second interferometer loop, which directly enters the duality relation. It was found that the three path intensities are slightly differing, therefore the ideal model has to be modified:

$$\begin{aligned} I_O &= I_n + \left| A_1 e^{-i(\alpha_1+\gamma_1)} + A_2 e^{-i(\alpha_2+\gamma_2)} + A_3 e^{-i(\alpha_1+\gamma_2)} \right|^2, \\ I_O &= I_n + A_1^2 + A_2^2 + A_3^2 + 2A_1A_2 \cos(\Delta\alpha + \Delta\gamma) \\ &\quad + 2A_1A_3 \cos(\Delta\gamma) + 2A_2A_3 \cos(\Delta\alpha), \end{aligned} \tag{143}$$

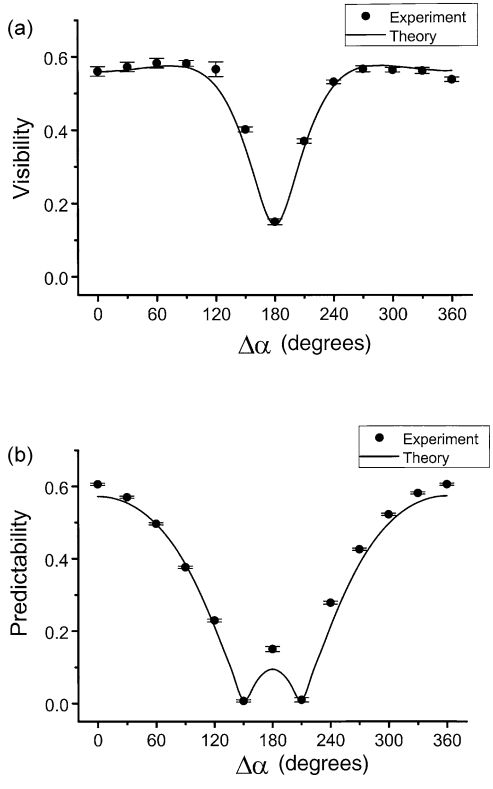

FIGURE 30. Coherent duality manipulations under realistic experimental conditions. (a) Reduced intrinsic visibilities V_i revoke the strong duality relation shown in Figure 29. However, the visibility is regained after a 2π phase cycle; this confirms that dephasing has no influence in this duality measurement. (b) The reduced predictability around $\Delta\alpha \approx 180$ degrees is caused by the presence of noninterfering intensity (Zawisky, 2004).

with empirical parameters for the noninterfering intensity $I_n = 1.786(35)$ and the amplitudes A_i [$A_1 = A_2 = 0.94(2)$, $A_3 = 1.12(2)$]. This more realistic model yields the following predictability (Figure 30):

$$P_{\mathrm{O}} = \left| \frac{I_n/3 - A_1^2 + A_2^2 + A_3^2 + 2A_2A_3\cos\Delta\alpha)}{I_n + A_1^2 + A_2^2 + A_3^2 + 2A_2A_3\cos\Delta\alpha)} \right|. \tag{144}$$

The reappearance of P and V after a full cycle of 360 degrees proves that dephasing plays no essential role in our duality measurements. The neutrons leave no imprints on the apparatus that can be used for which-way sorting.

C. Applications

It can be expected that the new possibilities of coherent beam manipulation will find useful applications (e.g., in experiments where an optimal intensity tuning is required in one interference loop, or in the context of interaction weak measurements where the interaction with a sample placed in beam II can notably be reduced by maintaining still reasonable visibilities). A remarkable feature of the two-loop interferometer is that the whole duality information becomes accessible simultaneously without any irreversible changes of the interferometer setup. In the two-loop interferometer beam II is in a superposition of two coherent beams; therefore path information should not superficially be misused as particle property. In fact, the particle aspect of the neutron did not show up in our duality experiments because no intensity measurements were performed inside the interferometer. The measured duality relation demonstrates that all neutron states contain which-way and visibility information because the extreme situations $P = 1 \Leftrightarrow V = 0$ and $P = 0 \Leftrightarrow V = 1$ is never realized in real experiments. A strict duality, $P^2 + V^2 = 1$, only appears in the ideal two-loop interferometer; experimentally we could achieve a maximum of 0.7 in the duality relation. The which-way tuning can be achieved by controlled coherent beam manipulations without changing the neutron's momentum and without essential dephasing.

The neutron's duality relates to all experiments where a sample is placed in one interfering beam. In phase tomography the attenuation of an interfering beam yields valuable information about the sample, for example, small-angle scattering caused by inhomogeneities yields information about the grain size and the sample structure. Interactions in the sample modify the transmission probability but also affect the visibility due to phase fluctuations in the sample. In the spirit of duality, all processes, which in principle can deliver which-way information, will necessarily reduce the visibility. Unfortunately, the opposite is not true, the simple existence of small visibility does not allow any which-way speculation, with the unrealistic exception that all other instrumental effects can be excluded.

VIII. Applications of Fundamental Quantum Effects in Imaging: Zeno Tomography

Let us discuss how the application of the principles at the basis of the QZE introduced in Section III.G can be of great assistance in tomography, when one is interested in minimizing the amount of radiation absorbed by the sample.

Under otherwise ideal conditions the shot noise associated with the discrete character of the illuminating beam sets an upper limit to the resolution

of absorption tomography; for instance, the shadow cast by a brain tumor might become totally lost in the noisy data. One possibility to overcome the fluctuations is to increase the intensity of the beam. However, in many situations, as in medicine for example, the intensity of the illuminating beam cannot be made arbitrarily high due to the damage provoked by the absorbed radiation.

A significant step toward an "absorption-free tomography" came from quantum theory. It was demonstrated, both theoretically (Elitzur and Vaidman, 1993; Hafner and Summhammer, 1997) and experimentally (Kwiat *et al.*, 1995), that *totally* transmitting and absorbing bodies can be distinguished without absorbing any particles, by using an interferometric setup. This idea is, in fact a clever implementation of the QZE, discussed in Section III.G, and hinges on the notion of interaction-free measurement, introduced in Section III.F. A classical measuring apparatus (here the black sample), placed in one arm of the interferometer, projects the illuminating particle into the other arm, destroying interference, freezing the evolution, and forcing the particle to exit through a different channel from what it would have chosen had both arms been transparent (white sample).

In practical applications, however, samples are normally neither black nor white: they are gray. It is important to understand whether application of the QZE, which turns out to be ideal for discriminating black and white, might also be advantageous for the more practical task of discriminating two gray bodies with different transmission coefficients. More specifically, we ask: is it possible to reduce the number of absorbed particles by QZE while preserving the resolution? We show that this is indeed possible, provided that the frequency of occurrences of the different levels of "gray" in the sample is not uniform (Facchi *et al.*, 2002). Closely related questions have been recently investigated by other authors (Krenn *et al.*, 2000; Mitchinson and Massar, 2001; Massar *et al.*, 2002). The Zeno setup, unlike the standard one, is endowed with two detection channels. As will be seen, this feature, if properly exploited, leads to even better performances in the Zeno case.

A. *Quantum Zeno Effect in a Mach–Zehnder Interferometer*

Consider the Mach–Zehnder interferometric (MZI) scheme with feedback displayed in Figure 31(a). A semitransparent object, whose transmission amplitude is τ (assumed real for simplicity) is placed in the lower arm of the interferometer. The particle is initially injected from the left, crosses the interferometer L times, and is finally detected by one of two detectors. The two semitransparent mirrors M are identical and their amplitude transmission

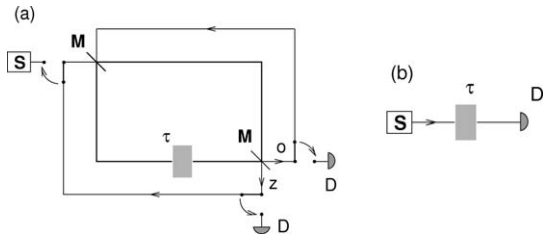

FIGURE 31. (a) Scheme of the Zeno interferometric setup. (b) Standard transmission experiment. S, Source; M, semi-transparent mirror; o, orthogonal channel; z, Zeno channel; D, detector.

and reflection coefficients are

$$c \equiv \cos\theta_L, \qquad s \equiv \sin\theta_L \quad (\theta_L = \pi/4L), \tag{145}$$

respectively. Notice that both coefficients depend on L, the number of "loops" in the MZI.

The incoming state of the particle (coming from the source at initial time) is

$$|\text{in}\rangle = \begin{pmatrix} 1 \\ 0 \end{pmatrix} \tag{146}$$

and we call "Zeno" and "orthogonal" channels the extraordinary $\binom{1}{0}$ and ordinary $\binom{0}{1}$ channels of the MZI, respectively. The total effect of the interferometer is

$$V_\tau = BA_\tau B, \quad B = \begin{pmatrix} c & -s \\ s & c \end{pmatrix}, A_\tau = \begin{pmatrix} 1 & 0 \\ 0 & \tau \end{pmatrix}. \tag{147}$$

In general,

$$B = \exp(-i\theta_L\sigma_2), \qquad BB^\dagger = B^\dagger B = 1, \tag{148}$$

where σ_2 is the second Pauli matrix, while A_τ is not unitary (if $\tau < 1$ there is a probability loss). The final state, after the particle has gone through L loops, reads

$$|\text{out}\rangle = V_\tau^L|\text{in}\rangle = (BA_\tau B)^L|\text{in}\rangle. \tag{149}$$

1. *White Sample*

The choice of the angle θ_L in Eq. (145) is motivated by our requirement that if $\tau = 1$ ("white" sample, i.e., no semitransparent object in the MZI) the particle ends up in the "orthogonal" channel:

$$V_{\tau=1}^L = B^{2L} = e^{-i2L\theta_L\sigma_2} = e^{-i\pi\sigma_2/2} = -i\sigma_2, \tag{150}$$

so that

$$|\text{out}\rangle = V_{\tau=1}^{L}|\text{in}\rangle = \begin{pmatrix} 0 \\ 1 \end{pmatrix}. \tag{151}$$

This is easy to understand: each loop "rotates" the particle's state by $2\theta_L = \pi/2L$ and after L loops the final state is "orthogonal" to the initial one [Eq. (146)].

2. *Black Sample*

Let us now look at the case $\tau = 0$, corresponding to a completely opaque ("black") object in the MZI. We obtain

$$V_{\tau=0}^{L} = B\left(A_0 B^2\right)^L B^{-1} = B\cos^L 2\theta_L \begin{pmatrix} 1 & -\tan 2\theta_L \\ 0 & 0 \end{pmatrix} B^{-1}$$
$$\overset{L\to\infty}{\longrightarrow} \begin{pmatrix} 1 & 0 \\ 0 & 0 \end{pmatrix} \equiv \mathcal{V}_{\tau=0}. \tag{152}$$

This yields QZE:

$$|\text{out}\rangle = \mathcal{V}_{\tau=0}|\text{in}\rangle = |\text{in}\rangle = \begin{pmatrix} 1 \\ 0 \end{pmatrix}. \tag{153}$$

In the infinite L limit, the initial state is "frozen" and the particle ends up in the Zeno channel.

3. *Gray Sample*

What happens if $0 < \tau < 1$? The computation is straightforward but lengthy and yields a final expression that is elementary but complicated. However, we are mainly interested in the large L limit, where V_τ^L can be approximated as follows:

$$V_\tau^L = \begin{pmatrix} 1 - \frac{\pi^2}{8L}\frac{1+\tau}{1-\tau} & \mathrm{O}(L^{-1}) \\ \mathrm{O}(L^{-1}) & \tau^L[1 + \mathrm{O}(L^{-1})] \end{pmatrix} + \mathrm{O}(L^{-2}). \tag{154}$$

This is an interesting result: indeed

$$\mathcal{V}_\tau \equiv \lim_{L\to\infty} V_\tau^L = \begin{pmatrix} 1 & 0 \\ 0 & 0 \end{pmatrix}, \quad 0 \le \tau < 1 \tag{155}$$

analogously to Eq. (152). This shows that even for a semitransparent object, with transmission coefficient $\tau \neq 1$, a *bona fide* QZE takes place and the particle ends up in the Zeno channel with probability 1:

$$|\text{out}\rangle = \mathcal{V}_\tau|\text{in}\rangle = |\text{in}\rangle, \quad \tau \neq 1. \tag{156}$$

B. Distinguishing Different Shades of Gray

A question arises (Mitchinson and Massar, 2001; Massar *et al.*, 2002): is it possible to distinguish different values of τ (different "shades" or "levels" of gray) by the technique outlined above? This is not a simple task, for after a large number of loops L, the particle ends up in the orthogonal channel only if $\tau = 1$ [see Eq. (151)]. By contrast, for any value of $\tau \neq 1$, the particle ends up in the Zeno channel [see Eq. (156)] *irrespective* of the particular value of τ. However, the asymptotic correction in the (1, 1) element of V_τ^L in Eq. (154) is τ dependent: the details of the convergence to the limit as defined in Eqs. (155) and (156) depend on the grayness of the sample. By exploiting this feature, we shall now show that it is indeed possible to resolve different gray levels by QZE, within a given statistical accuracy.

We start by observing that if one performs a standard transmission experiment, by shining a particle beam on a semitransparent object in order to measure the transmission coefficient τ (see Figure 31[b]), the detection and absorption probabilities read

$$p'_d(\tau) = \tau^2, \qquad p'_a(\tau) = 1 - \tau^2. \tag{157}$$

The statistic is binomial.

On the other hand, if the Zeno configuration sketched in Figure 31(a) is used, the final state of the particle after L loops in the MZI is, from Eq. (154),

$$V_\tau^L \begin{pmatrix} 1 \\ 0 \end{pmatrix} = \begin{pmatrix} u_z \\ u_o \end{pmatrix} = \begin{pmatrix} 1 - \frac{\pi^2}{8L}\frac{1+\tau}{1-\tau} + \mathrm{O}(L^{-2}) \\ \mathrm{O}(L^{-1}) \end{pmatrix}, \tag{158}$$

where u_z and u_o are the amplitudes in the Zeno and orthogonal channels, respectively. Both these quantities are real. Let $(0 \leq \tau < 1)$

$$\begin{aligned} p_z(\tau) &= u_z^2 = 1 - \frac{\pi^2}{4L}\frac{1+\tau}{1-\tau} + \mathrm{O}\big(L^{-2}\big), \\ p_o(\tau) &= u_o^2 = \mathrm{O}\big(L^{-2}\big), \quad \text{and} \\ p_a(\tau) &= 1 - p_z(\tau) - p_o(\tau) = \frac{\pi^2}{4L}\frac{1+\tau}{1-\tau} + \mathrm{O}\big(L^{-2}\big) \end{aligned} \tag{159}$$

be the probabilities that the particle is detected in the Zeno, orthogonal channel, or is absorbed by the semitransparent object, respectively. We assume that a fixed number of particles N is sent in the MZI during an experimental run. In this situation, the distribution of particles in the Zeno, orthogonal, or absorption channels follows a *trinomial* statistics with probabilities [Eq. (159)].

C. Reconstruction

Now we will construct a protocol and show that using QZE can achieve a resolution that is *superior* to the "ordinary" resolution obtained in a standard transmission experiment. Notice that $p_a(\tau)$ in Eq. (159), unlike $p'_a(\tau)$ in Eq. (157), is an *increasing* function of τ. Therefore, with respect to absorbed particles, the Zeno tomographic image (for sufficiently large L) yields a kind of negative of the standard absorption tomographic image. This can be given a rather intuitive explanation: indeed, the absorption probability in Eq. (159) reduces to the same form as the standard one of Eq. (157), that is,

$$p_a(\tau) = 1 - \left(\tau_{\text{eff}}^{\text{Ze}}\right)^2, \tag{160}$$

by introducing an "effective" transmission coefficient

$$\tau_{\text{eff}}^{\text{Ze}} = \sqrt{1 - p_a}. \tag{161}$$

For example, if we take $\tau_1 = 0.98$, $\tau_2 = 0.99$ and choose $L = 12000$, then, according to Eq. (159), we get $\tau_{\text{eff1}}^{\text{Ze}} \approx 0.99$ and $\tau_{\text{eff2}}^{\text{Ze}} \approx 0.98$. The two gray levels are *interchanged* by the Zeno apparatus. If most of the sample has transmission coefficient τ_2, the absorbed energy is reduced by using the Zeno setup.

A more precise comparison of the performances of the Zeno and standard techniques can be given in the framework of decision theory. For simplicity let us focus on distinguishing only two gray levels τ_1 and τ_2 ($\tau_1 < \tau_2$) corresponding to hypotheses H_1 and H_2 that occur in the sample with frequencies

$$P_0(H_1) = \alpha, \qquad P_0(H_2) = 1 - \alpha. \tag{162}$$

The probability of making an error in identifying the gray level of a given pixel is

$$P_e = \alpha P(H_2|H_1) + (1 - \alpha) P(H_1|H_2), \tag{163}$$

where $P(H_i|H_j)$ is the probability of choosing H_i when H_j is true. This probability depends on the total number of particles N, as well as on the decision strategy adopted. The corresponding mean number of absorbed particles is

$$N_a = N\big[\alpha p_a(\tau_1) + (1 - \alpha) p_a(\tau_2)\big]. \tag{164}$$

The error P_e of any reasonable strategy decreases with N, while the total number of absorbed particles N_a increases linearly with N. The objective is to find the strategy minimizing P_e given N_a.

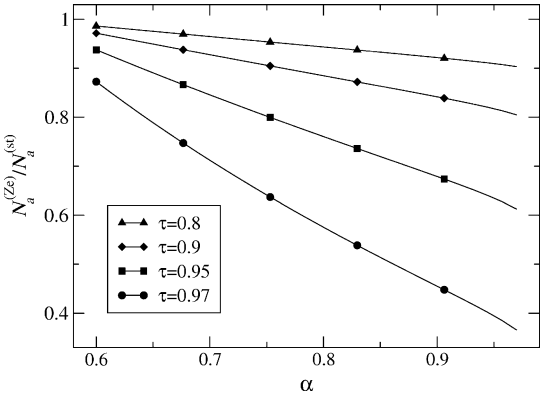

FIGURE 32. Ratio of the number of absorbed particles in the Zeno ($N_a^{(\mathrm{Ze})}$) and standard ($N_a^{(\mathrm{st})}$) setup. The smaller the ratio in the graph, the less irradiation in the Zeno apparatus (for the same resolution). $P_e = 0.5\%$; $\tau_1 = \{0.8, 0.9, 0.95, 0.97\}$; $\tau_2 = \tau_1 + 0.02$; $L = 2000$.

For the Zeno setup, two decision strategies can be formulated. When the number of loops L is very large, there are almost no particles exiting via the ordinary channel $n_o \approx 0$ and hence our decision will be based on the number of absorbed particles n_a. If n_a is smaller than or equal to a decision level n_a^d, then H_1 is chosen; otherwise H_2 is chosen. Details of finding optimal n_a^d can be found in Facchi *et al.* (2002).

The performances of this *binomial protocol* and standard absorption setup are compared in Figure 32, where the ratio of their number of absorbed particles is shown as a function of α for a few different gray levels. Notice that the exposition of the sample can be significantly reduced if the distribution of gray levels in the sample is not uniform. For instance, a reduction factor of 2.5 is obtained when the sample consists of 97% of dense material and only 3% of the less absorbing one, $\alpha = 0.97$. Such parameters would be typical for structural analyses. A small structural defect (crack) inside a thin sample would typically show small contrast ($\tau_2 - \tau_1 \ll 1$) with the surrounding almost transparent ($\tau_1 \approx 1$) material, while its area would be small compared to the area of the sample ($\alpha \approx 1$).

The above simple binomial decision strategy is, however, not the optimum one. Unavoidable losses and other imperfections of real experimental devices set a strict limit on the maximum number of loops that can be achieved in a laboratory. In such cases the ordinary channel can no longer be ignored. The statistics of the experiment are then trinomial, and the data consist of the two component vector (n_z, n_o) of the numbers of particles counted in the Zeno and ordinary output channels, respectively. The optimal decision will be based on *both* these numbers.

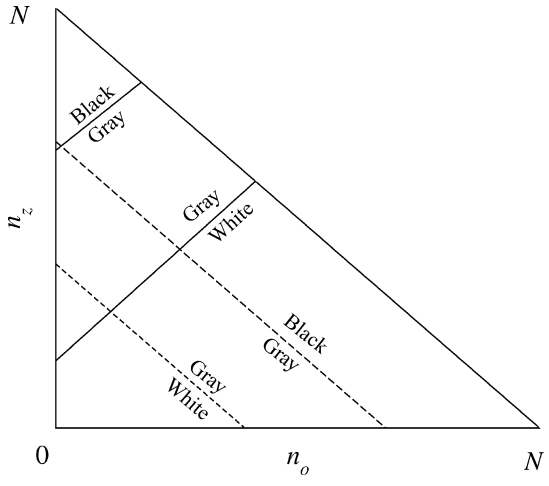

FIGURE 33. Typical decision levels of the binomial (dashed lines) and trinomial (solid lines) decision strategies when $a \approx 1$. This figure corresponds to the simulation shown in the last row of Figure 35(c), where $M = 3$, the triangle is divided into $M = 3$ regions, and the three gray shades are labeled as white, gray, and black, respectively.

As was shown in Facchi *et al.* (2002), there is a one-parametric family of optimal decision vectors (n_z^d, n_o^d),

$$n_z^d - a(\tau_1, \tau_2) n_o^d = b(\tau_1, \tau_2, \alpha), \tag{165}$$

where a and b are coefficients. In a 2D representation, each possible experimental outcome (n_z, n_o) is represented by a point lying inside the triangle $\{0 \le n_o + n_z \le N\}$ shown in Figure 33. Equation (165) divides this triangle into two regions. All experimental outcomes that fall within the same region issue the same decision. In the general case of M different gray levels, there are $M - 1$ Eqs. (165) defining $M - 1$ in general nonparallel lines dividing the square into M strip-like regions. This is shown in Figure 33 for $M = 3$.

An interesting situation arises when the coefficient a in Eq. (165) becomes close to unity. In that case, the decision level is the line $n_z^d - n_o^d = \text{const}$. Let us recall that the decision levels of the binomial strategy based on the number of absorbed particles only, read $n_a^d = \text{const.}$, or, equivalently, $n_z^d + n_o^d = \text{const}$. Hence, if L, τ_1, and τ_2 are such that $a \approx 1$, the decision levels of the binomial and trinomial decision strategies will become *orthogonal* to each other. This is shown in Figure 33. Under such conditions further gain in the precision of the Zeno apparatus can be expected compared to standard absorption tomography. This regime was chosen for our computer simulations of the following section.

FIGURE 34. The object to be reconstructed: a cell of *Giardia lamblia*, one of the most primitive eukaryotes. The original picture has been reduced for simplicity to three levels of gray: white, gray and black, occurring with frequencies $\alpha_w = 0.02$, $\alpha_g = 0.07$, and $\alpha_b = 0.93$ respectively.

D. Simulations

We have seen that the Zeno technique can reduce the level of absorption without losing resolution (compared to the standard technique. Alternatively, the Zeno setup can yield an improved resolution, while keeping the absorption at the same level of the standard setup.) The object in Figure 34 is a cell of *Giardia lamblia*, a protist, one of the most primitive eukaryotes. *Giardia* has been called a "missing link" in the evolution of eukaryotic cells from prokaryotic cells. The number of gray levels in the figure has been reduced to three to make the analysis simpler: white, gray, and black, $\tau_w = 0.99$, $\tau_g = 0.96$, $\tau_b = 0.8$, occurring with frequencies $\alpha_w = 0.02$, $\alpha_g = 0.07$, and $\alpha_b = 0.93$, respectively. Figure 35 shows the results of a numerical simulation, performed with the standard and Zeno methods, the latter for $L = 10$ and $L = 165$, for different numbers of absorbed particles N_a. In each frame the standard and the two Zeno reconstructions are compared, together with the pixels that have been misinterpreted. Figure 35 confirms the expectation based on the asymptotic formulas in Eq. (159): in general, provided that the object contains a small fraction of more transparent pixels and a larger fraction of more absorbing material, the Zeno setup yields a better resolution for a given irradiation. Clearly, a significant improvement with respect to standard absorption tomography is achieved for as few as $L = 10$ loops. The improvement is very large for $L = 165$.

The number of absorbed particles increases from (a) to (d) in Figure 35. Observe that in (a) the standard reconstruction fails completely, while the outline and basic shape of the object can be recognized already in the Zeno reconstruction with $L = 10$. In (c) the Zeno reconstructions are quite good, while standard tomography does not detect white pixels in the object. When the intensity of the illuminating beam is increased further, in frame (d), all the reconstructed images become visually hard to tell from the sample, but the error rates of the Zeno apparatuses are still much better (by a factor of 3 or more), as shown by the number of misinterpreted pixels.

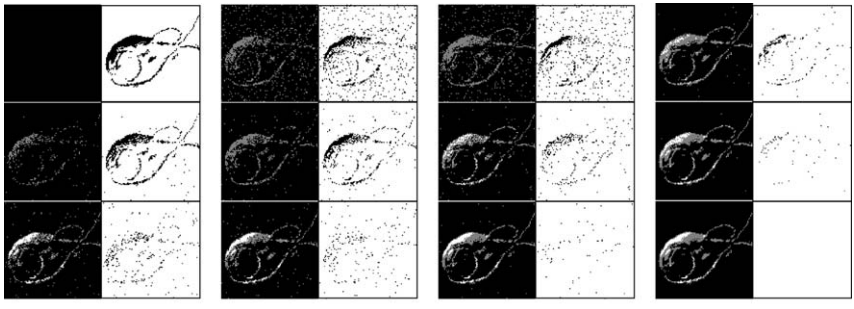

FIGURE 35. Comparison of standard and Zeno tomographic techniques. In each frame: top left = reconstruction by standard technique; top right = misinterpreted pixels by the standard technique; center left = reconstruction by Zeno technique with $L = 10$; center right = misinterpreted pixels by the Zeno technique with $L = 10$; bottom left = reconstruction by Zeno technique with $L = 165$; bottom right = misinterpreted pixels by the Zeno technique with $L = 165$. The mean number of absorbed particles per pixel (irradiation) is $N_a = 1.7, 2.3, 4$, and 13 for frames (a), (b), (c), and (d) respectively. We used $\tau_w = 0.99$, $\tau_g = 0.96$, and $\tau_b = 0.8$. The sample consists of 10,000 ($= 100 \times 100$) pixels, where white, gray, and black occur with frequencies $\alpha_w = 0.02$, $\alpha_g = 0.07$, and $\alpha_b = 0.93$, respectively.

The distribution of misinterpreted pixels merits comment. Clearly, in all the cases analyzed, this distribution is not uniform. In general, when the distribution of gray levels in the sample is not uniform, any reconstruction technique tends to perform better in the "background," while making more mistakes in the region where the "structure" is present. The improvement due to the Zeno method becomes apparent particularly in Figures 35(b) and (c). In these cases, interestingly, the standard method yields more mistakes in the background; this is an unpleasant feature, if one is interested in detecting small irregular structures in a more or less uniform background. The features of the distribution of misinterpreted pixels require more careful study and their comprehension might lead to additional ideas.

Any increase in the number of loops L in the interferometer makes the difference between standard and Zeno tomography even greater. Clearly, this is more demanding in terms of experimental realization.

E. Discussion

We have shown that a quantum Zeno tomography is possible and performs better than standard tomography if a given prior knowledge about the distribution of grays in the sample is available. This is a common situation in

radiography, where one is often interested in detecting a small structure in a uniform background, for instance, in the analysis of small structural defects.

In our numerical simulations we have illustrated some situations in which the resolution is improved by the Zeno method, for a *given number of absorbed particles*. Alternatively, for a *given resolution*, the Zeno method performs better, absorbing fewer particles. This can be interesting in applications, for instance, if one wants to limit the damage provoked by the absorption of radiation without losing in resolution.

It is obvious from Figure 32 that an even larger improvement is possible for almost transparent samples, provided that α is close to unity. This means that there is *no fundamental limit* on the improvement that can be achieved over the standard setup; in other words, there is no "optimal" configuration.

Additional issues deserve careful study: for instance, the effects due to a Poissonian beam (total number of incoming particles N not fixed) and a complex transmission coefficient τ.

Let us also comment on experimental feasibility. Figure 35 shows that an experimental test of the Zeno tomographic technique should not be as difficult as one might think: simulations have been performed for as few as $L = 10$ loops in the interferometer, giving better results than the standard method. It is reasonable to believe that a Zeno setup with a much larger number of loops can be built for ultraviolet (UV) light (highly absorbed by some biological samples). Also, by changing the light wavelength, one could efficiently "observe" different regions of the sample (or slightly different samples). Moreover, the experimental configuration we have proposed (photons in a MZI, as in Figure 31) is certainly not the only conceivable one. Phase imaging and tomography have been demonstrated for both X-rays and neutrons (Dubus *et al.*, 2002). More specific to this, Rauch and collaborators, with the VESTA apparatus (Jericha *et al.*, 2000; Rauch, 2001), have been able to keep *neutrons* in a 1-meter long perfect-crystal storage system ("resonator") for a few seconds, so that the neutrons bounce back and forth between two mirrors *several thousand* times. This would lead us to the full asymptotic ($L \gg 1$) regime considered in Figure 32 and the last row of Figure 35, where the Zeno method can perform much better.

IX. Interferometry and Decoherence: Sensitivity to Fluctuations

Decoherence is an interesting phenomenon, related to the long-standing issue of irreversibility. Currently, it discloses challenging perspectives in the light of new technologies and related physical applications. There is a widespread consensus (Giulini *et al.*, 1996; Namiki *et al.*, 1997; Zurek,

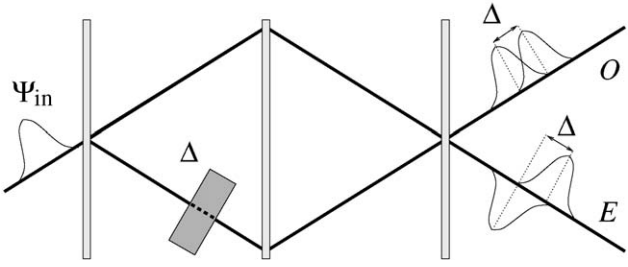

FIGURE 36. Scheme of a Mach–Zehnder interferometer.

1991) about the meaning of decoherence, viewed as the loss of quantum mechanical coherence of a physical system in interaction with other systems ("environment"). However, a *quantitative* definition of decoherence is subtle and involves conceptual pitfalls (Facchi *et al.*, 2001a; Mariano *et al.*, 2001). In addition, it always depends on the experimental configuration. An interesting quantity in this context is the square of the density matrix (Watanabe, 1939). Apart from lacking idempotency for mixed states, this quantity enjoys other interesting features (Manfredi and Feix, 2000), but also yields results that are at variance with naive expectations based on entropy (Facchi *et al.*, 2001a; Mariano *et al.*, 2001).

We consider here two different definitions of decoherence: the first is operational and stems from an analysis of the visibility in quantum (as well as classical, as we will see) interference experiments (Facchi *et al.*, 2003). We stress that these experiments are routinely performed in neutron optics (Bonse and Rauch, 1979; Badurek *et al.*, 1988, 2000b; Rauch and Werner, 2000b; Rauch *et al.*, 1996). The second definition is based on the idempotency defect of the density matrix and is, in this sense, less operational.

In both cases, decoherence displays an "anomalous" behavior, both as a function of the features of the fluctuations and the incoming state. Some concrete examples will be considered and discussed. Our analysis will focus on neutron optics and hinge on an approach based on the analysis of statistical fluctuations (Namiki and Pascazio, 1990, 1991; Kono *et al.*, 1996; Rauch and Suda, 1995, 1997; Rauch *et al.*, 1999).

A. Fluctuations in Neutron Optics

Let us start our analysis by considering a neutron beam that crosses an MZI, as schematically shown in Figure 36. A phase shifter Δ is placed in the lower arm of the interferometer, and $|\psi_{\text{in}}\rangle$ is the initial wave packet.

We neglect wave-packet dispersion effects, so that the outgoing states in the ordinary and extraordinary channels are

$$\begin{aligned} |\psi_O\rangle &= \frac{1}{2}\big[1 + e^{\frac{i}{\hbar}\hat{p}\Delta}\big]|\psi_{\text{in}}\rangle, \\ |\psi_E\rangle &= \frac{1}{2}\big[1 - e^{\frac{i}{\hbar}\hat{p}\Delta}\big]|\psi_{\text{in}}\rangle, \end{aligned} \tag{166}$$

respectively. We focus on the ordinary channel, the analysis for the extraordinary one being identical. Define the operator

$$\widehat{O}(\Delta) = \frac{1}{2}\big[1 + e^{\frac{i}{\hbar}\hat{p}\Delta}\big], \tag{167}$$

that accounts for the state evolution in the ordinary channel, and consider the output density matrix

$$\hat{\rho}_O \equiv |\psi_O\rangle\langle\psi_O| = \widehat{O}(\Delta)|\psi_{\text{in}}\rangle\langle\psi_{\text{in}}|\widehat{O}(\Delta)^\dagger = \widehat{O}(\Delta)\hat{\rho}_{\text{in}}\widehat{O}(\Delta)^\dagger, \tag{168}$$

where $\hat{\rho}_{\text{in}}$ is the density matrix of the incoming state. The trace of $\hat{\rho}_O$ yields the relative frequency of neutrons in the ordinary channel.

Suppose now that the phase shift Δ fluctuates according to a probability law $w(\Delta - \Delta_0)$, where Δ_0 is the average phase (operationally defined as the phase that is measured—or inferred (Řeháček *et al.*, 1999)—in an interferometric experiment). Therefore

$$\int d\Delta w(\Delta) = 1, \qquad \int d\Delta w(\Delta)\Delta = 0. \tag{169}$$

The trace of the average density matrix is

$$\operatorname{Tr}\overline{\hat{\rho}_O} = \operatorname{Tr}\int d\Delta w(\Delta - \Delta_0)\widehat{O}(\Delta)\hat{\rho}_{\text{in}}\widehat{O}(\Delta)^\dagger = \operatorname{Tr}\big(\hat{\rho}_{\text{in}}\overline{\widehat{O}(\Delta)^\dagger\widehat{O}(\Delta)}\big), \tag{170}$$

where the bar denotes the average over the distribution $w(\Delta - \Delta_0)$. One obtains, after some algebra,

$$\overline{\widehat{O}(\Delta)^\dagger\widehat{O}(\Delta)} = \frac{1}{2}\left(1 + \overline{\cos\frac{\hat{p}\Delta}{\hbar}}\right). \tag{171}$$

Consider now the Fourier transformation of the probability density of the fluctuations

$$\begin{aligned} \Omega(p) &\equiv \int d\Delta w(\Delta) e^{\frac{i}{\hbar}p\Delta} \\ &= \int d\Delta w(\Delta)\cos\frac{p\Delta}{\hbar} + i\int d\Delta w(\Delta)\sin\frac{p\Delta}{\hbar} \\ &= C(p) + iS(p), \end{aligned} \tag{172}$$

where C and S are, respectively, the real and the imaginary part of Ω:

$$C(p) = \mathrm{Re}\,\Omega(p), \tag{173}$$

$$S(p) = \mathrm{Im}\,\Omega(p). \tag{174}$$

In Eq. (171) we can write

$$\overline{\cos\frac{\hat{p}\Delta}{\hbar}} = \int d\Delta w(\Delta-\Delta_0)\cos\frac{\hat{p}\Delta}{\hbar} = \cos\frac{\hat{p}\Delta_0}{\hbar}C(\hat{p}) - \sin\frac{\hat{p}\Delta_0}{\hbar}S(\hat{p}). \tag{175}$$

For simplicity, we consider symmetric distribution functions, that is $w(\Delta) = w(-\Delta)$. Therefore

$$S(\hat{p}) = 0, \qquad C(\hat{p}) = \Omega(\hat{p}) \tag{176}$$

and Eq. (171) becomes

$$\overline{\widehat{O}(\Delta)^\dagger\widehat{O}(\Delta)} = \frac{1}{2}\left[1 + \Omega(\hat{p})\cos\frac{\hat{p}\Delta_0}{\hbar}\right]. \tag{177}$$

We notice, incidentally, that the same results are obtained with a different setup (Badurek *et al.*, 2000b): consider a polarized neutron that interacts with a magnetic field perpendicular to its spin. Due to the longitudinal Stern–Gerlach effect (Mezei, 1988; Golub *et al.*, 1994), its wave packet is split into two components that travel with different speeds and are therefore separated in space. After a projection onto the initial spin state, the resulting final state is slightly different from that considered in the preceding equations; we need to replace $|\psi_O\rangle$ (and analogously $|\psi_E\rangle$) in Eq. (166) with

$$|\psi_O\rangle \longrightarrow |\psi'_O\rangle = \widehat{O}'(\Delta)|\psi_{\mathrm{in}}\rangle, \tag{178}$$

where

$$\widehat{O}'(\Delta) = \frac{1}{2}\left[e^{-\frac{i}{2\hbar}\hat{p}\Delta} + e^{\frac{i}{2\hbar}\hat{p}\Delta}\right], \tag{179}$$

and Δ is in this case the spatial separation between the two wave packets corresponding to the two spin components. By averaging over Δ it is easy to show that one obtains again Eq. (177).

By inserting the average operator in Eq. (177) into Eq. (170) one finally determines

$$\mathrm{Tr}\,\overline{\hat{\rho}_O} = \frac{1}{2}\left[1 + \left\langle\Omega(\hat{p})\cos\frac{\hat{p}\Delta_0}{\hbar}\right\rangle\right], \tag{180}$$

where $\langle\cdots\rangle = \mathrm{Tr}[\hat{\rho}_{\mathrm{in}}\cdots]$ denotes the expectation value over the initial state $\hat{\rho}_{\mathrm{in}}$. On the other hand, the momentum distribution is easily shown to be

$$P_O(p) = \langle p|\overline{\hat{\rho}_O}|p\rangle = \mathrm{Tr}\big(|p\rangle\langle p|\overline{\hat{\rho}_O}\big) = \frac{1}{2}P_{\mathrm{in}}(p)\left[1 + \Omega(p)\cos\frac{p\Delta_0}{\hbar}\right], \tag{181}$$

where

$$P_{\mathrm{in}}(p) = \langle p|\hat{\rho}_{\mathrm{in}}|p\rangle. \tag{182}$$

We now introduce the *visibility* of the interference pattern (in the ordinary channel)

$$\mathcal{V}(p) \equiv \frac{P_O(p)_{\mathrm{MAX}} - P_O(p)_{\mathrm{min}}}{P_O(p)_{\mathrm{MAX}} + P_O(p)_{\mathrm{min}}} = \big|\Omega(p)\big|, \tag{183}$$

where $P_O(p)_{\mathrm{MAX}}$ [$P_O(p)_{\mathrm{min}}$] is the maximum [minimum] value assumed by $P_O(p)$ when Δ_0 varies. By the very definition [Eq. (172)], one can verify that $0 \leq \mathcal{V}(p) \leq 1$. Notice that, according to this definition, the visibility is a function of momentum p and yields a measure of the fringe visibility of a post-selected beam of momentum p as a function of the phase shift Δ_0 (Badurek *et al.*, 2000b; Kaiser *et al.*, 1992; Jacobson *et al.*, 1994). Equivalently, it is a measure of the "local" spectral visibility, under the assumption of a slowly varying wave envelope, and so it corresponds to (the absolute value of) the amplitude of the cosine function in Eq. (181). By using Eqs. (172) and (183), it can be inferred that the visibility is the modulus of the Fourier transformation of the distribution of the shifts Δ and is therefore a quantity that is closely related to the physical features of the phase shifter. In this way we can easily relate the visibility of the interference pattern (and, as we will see below, the decoherence) to the "environmental" fluctuations. Note that a completely equivalent definition of the spectral visibility [Eq. (183)], which is nevertheless more symmetric and makes use also of the extraordinary channel, reads

$$\mathcal{V}(p) = \max_{\Delta_0}\frac{|P_O(p) - P_E(p)|}{P_O(p) + P_E(p)} = \max_{\Delta_0}\left|\Omega(p)\cos\frac{p\Delta_0}{\hbar}\right| = \big|\Omega(p)\big|, \tag{184}$$

where the momentum distribution of the extraordinary channel is given by

$$P_E(p) = \frac{1}{2}P_{\mathrm{in}}(p)\left[1 - \Omega(p)\cos\frac{p\Delta_0}{\hbar}\right], \tag{185}$$

whence $P_O(p) + P_E(p) = P_{\mathrm{in}}(p)$. The spectral visibility in the form of Eq. (184) leads to a straightforward generalization that is at the basis of an operational definition of decoherence.

B. An Operational Definition of Decoherence

Let us endeavor to provide a quantitative definition of decoherence based on the definition of visibility given in the previous subsection. We start from the relative frequency of particles detected in the ordinary and extraordinary

channels:

$$\begin{aligned}\mathcal{N}_O(\Delta_0) &= \mathrm{Tr}\,\overline{\hat{\rho}_O} = \frac{1}{2}\left[1 + \left\langle \Omega(\hat{p})\cos\frac{\hat{p}\Delta_0}{\hbar}\right\rangle\right],\\ \mathcal{N}_E(\Delta_0) &= \mathrm{Tr}\,\overline{\hat{\rho}_E} = \frac{1}{2}\left[1 - \left\langle \Omega(\hat{p})\cos\frac{\hat{p}\Delta_0}{\hbar}\right\rangle\right].\end{aligned} \tag{186}$$

Their difference is

$$\mathcal{N}_O(\Delta_0) - \mathcal{N}_E(\Delta_0) = \left\langle \Omega(\hat{p})\cos\frac{\hat{p}\Delta_0}{\hbar}\right\rangle, \tag{187}$$

and one can define a *generalized visibility* (Facchi *et al.*, 2003)

$$\begin{aligned}\mathcal{V} &= \max_{\Delta_0}\left|\mathcal{N}_O(\Delta_0) - \mathcal{N}_E(\Delta_0)\right| = \max_{\Delta_0}\left|\left\langle \Omega(\hat{p})\cos\frac{\hat{p}\Delta_0}{\hbar}\right\rangle\right|\\ &= \max_{\Delta_0}\left|\int dp\, P_{\mathrm{in}}(p)\Omega(p)\cos\frac{p\Delta_0}{\hbar}\right|.\end{aligned} \tag{188}$$

It is apparent that Eq. (188) is the straightforward generalization of the spectral visibility [Eq. (184)], because obviously $\mathcal{N}_O + \mathcal{N}_E = 1$. It represents a *global* feature of the outgoing state, in contrast with the local character of Eq. (184). Notice, however, that when $P_{\mathrm{in}}(p') = \delta(p' - p)$ (incoming monochromatic beam of momentum p), the generalized visibility [Eq. (188)] reduces to the standard "local" visibility [Eq. (183)]:

$$\begin{aligned}\mathcal{V} &= \max_{\Delta_0}\left|\int dp'\delta(p' - p)\Omega(p')\cos\frac{p'\Delta_0}{\hbar}\right|\\ &= \max_{\Delta_0}\left|\Omega(p)\cos\frac{p\Delta_0}{\hbar}\right| = \mathcal{V}(p).\end{aligned} \tag{189}$$

This is a consistency check, because a spectral postselection is equivalent to injecting an incoming monochromatic beam.

In general, one obtains

$$\mathcal{V} \le \max_{\Delta_0}\int dp\, P_{\mathrm{in}}(p)\left|\Omega(p)\right|\left|\cos\frac{p\Delta_0}{\hbar}\right| = \int dp\, P_{\mathrm{in}}(p)\mathcal{V}(p) = \left\langle \mathcal{V}(\hat{p})\right\rangle. \tag{190}$$

The generalized visibility yields the maximum "distance" between the intensities $\mathcal{N}_O$ and $\mathcal{N}_E$ and is bounded by the "local" visibility averaged over the momentum distribution of the incoming state.

Notice that $P_{\mathrm{in}}(p)$ is a nonnegative quantity, while $\Omega(p)$, because it is a Fourier transformation, is not. For this reason, in general, the $\max_{\Delta_0}$ does not enter into the integral sign in Eq. (188), so that Eq. (190) is a strict inequality. However, in the particular case $\Omega(p) \ge 0$, $\mathcal{V}$ saturates its upper bound, the

equality sign holds in Eq. (190), and Eq. (188) simplifies into

$$\mathcal{V} = \int dp\, P_{\text{in}}(p)\Omega(p) \quad (\Omega(p) \geq 0). \tag{191}$$

As is often expected, the most interesting cases are those situations in which $\Omega(p)$ is *not* always positive, giving rise to "anomalous" situations.

In order to understand the physical meaning of the generalized visibility, it is useful to look at the example of a fluctuation-free phase shifter, $w(\Delta) = \delta(\Delta)$, for which Eq. (172) yields $\Omega(p) = 1$, so that the generalized visibility [Eq. (188)] becomes

$$\mathcal{V} = \max_{\Delta_0} \left| \int dp\, P_{\text{in}}(p) \cos \frac{p\Delta_0}{\hbar} \right| = \int dp\, P_{\text{in}}(p) = 1, \tag{192}$$

for any incoming distribution P_{in}. This result follows also directly from Eq. (191). For instance, for an incoming Gaussian wave packet

$$P_{\text{in}}(p) = \sqrt{\frac{2\delta^2}{\hbar^2\pi}} \exp\left(-\frac{2\delta^2}{\hbar^2}(p - p_0)^2 \right), \tag{193}$$

the interference patterns $\mathcal{N}_O$ and $\mathcal{N}_E$ are derived as shown in Figure 37, where it is apparent that $\mathcal{V} = 1$.

If, on the other hand, the phase shifter fluctuates, the amplitude of the envelope function decreases and $\mathcal{V} < 1$. We therefore give an operational definition of decoherence, by defining a *decoherence parameter*:

$$\begin{aligned} \varepsilon \equiv 1 - \mathcal{V} &= 1 - \max_{\Delta_0} \left| \left\langle \Omega(\hat{p}) \cos \frac{\hat{p}\Delta_0}{\hbar} \right\rangle \right| \\ &= 1 - \max_{\Delta_0} \left| \int dp\, P_{\text{in}}(p)\Omega(p) \cos \frac{p\Delta_0}{\hbar} \right|. \end{aligned} \tag{194}$$

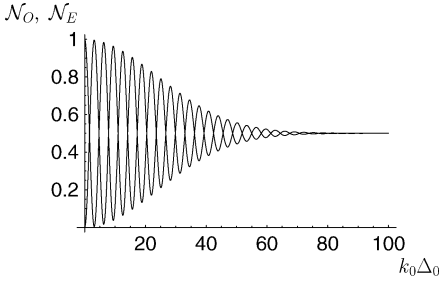

FIGURE 37. Relative frequencies of neutrons detected in the ordinary $\mathcal{N}_O$ and extraordinary $\mathcal{N}_E$ channel versus $k_0\Delta_0$ ($k_0 = p_0/\hbar$), for an incoming Gaussian wave packet [Eq. (193)] with $k_0\delta = 12$ and a fluctuation-free phase shifter. The two intensities differ in phase by π and their sum is 1. The generalized visibility [Eq. (188)] is 1.

Notice that, by Eq. (192), $\varepsilon = 0$ for a fluctuation-free phase shifter (quantum coherence perfectly preserved), whereas $\varepsilon \to 1$ when the magnitude of the fluctuations increases, $\Omega(p) \to 0$ and the envelope function in Figure 37 squeezes away all oscillations, eventually yielding $\mathcal{N}_O(\Delta_0) = \mathcal{N}_E(\Delta_0)$, independent of Δ_0. Observe also that $\mathcal{V}$ and ε are independent of the coherence of the initial state (namely, they do not depend on the off-diagonal terms of the density matrix). Conversely, they strongly depend on the momentum distribution of the initial state [Eq. (182)]. In this sense, they measure the *loss* of quantum coherence caused by a given physical setup, independent of the coherence of the incoming state.

It is important to stress that the above definition of decoherence is *operational*. First the relative frequencies of neutrons detected in the ordinary and extraordinary channels are measured as a function of Δ_0, both being measurable quantities. Then Eq. (188) is evaluated and ε is computed.

1. *Some Examples*

The decoherence parameter [Eq. (194)] depends on the product of the momentum distribution of the incoming beam times the spectrum of the phase-shifter fluctuations, $P_{\text{in}}(p) \times \Omega(p)$. These two ingredients affect ε at the same level. Therefore their role can be interchanged: by maintaining their product unaltered, there exist "dual" situations that give exactly the same decoherence parameter with very different kinds of statistical fluctuations and incoming states.

Noting the above remark, it is interesting to study some particular cases that can be treated analytically. Let the phases be distributed according to a Gaussian law with standard deviation σ

$$w(\Delta - \Delta_0) = \frac{1}{\sqrt{2\pi\sigma^2}} \exp\left(-\frac{(\Delta - \Delta_0)^2}{2\sigma^2}\right), \tag{195}$$

so that $\Omega(p) = \exp(-p^2\sigma^2/2\hbar^2)$ and the decoherence parameter reads

$$\begin{aligned} \varepsilon &= 1 - \max_{\Delta_0} \left| \int dp\, P_{\text{in}}(p) \exp\left(-\frac{p^2\sigma^2}{2\hbar^2}\right) \cos\left(\frac{p\Delta_0}{\hbar}\right) \right| \\ &= 1 - \int dp\, P_{\text{in}}(p) \exp\left(-\frac{p^2\sigma^2}{2\hbar^2}\right). \end{aligned} \tag{196}$$

For the Gaussian wave packet [Eq. (193)], one determines

$$\varepsilon = 1 - \sqrt{\frac{\delta^2}{\delta^2 + \sigma^2/4}} \exp\left(-\frac{\delta^2}{\delta^2 + \sigma^2/4} \frac{\sigma^2 k_0^2}{2}\right), \tag{197}$$

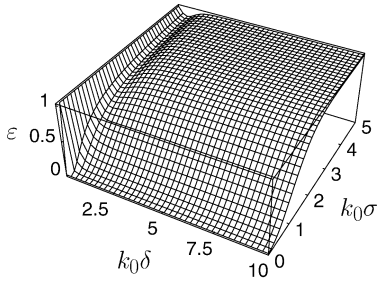

FIGURE 38. Decoherence parameter ε [Eq. (197)] versus width δ of the Gaussian wave packet and standard deviation σ of the fluctuating shifts ($k_0 = p_0/\hbar$).

with $k_0 = p_0/\hbar$. This is exact and is shown in Figure 38. At fixed δ the decoherence parameter [Eq. (197)] increases with σ, although the details of its behavior are strongly dependent on the spatial width of the packet δ. This behavior agrees with expectation: decoherence ε increases with the magnitude σ of the fluctuations.

For a monochromatic beam [$P_{\text{in}}(p') = \delta(p - p')$]

$$\varepsilon_k = 1 - e^{-\frac{k^2\sigma^2}{2}}, \tag{198}$$

with $k = p/\hbar$. This is shown in Figure 39(a) and can be obtained from Eq. (197) in the $\delta \to \infty$ limit. Notice that high momenta are more fragile against fluctuations (Rauch and Suda, 1995, 1997; Rauch *et al.*, 1999). Moreover, when the distribution of the shifts is Gaussian, ε_k and equivalently $\mathcal{V}(p)$ are monotonic functions; they both depend "smoothly" on σ.

Let now the phase shifts be distributed according to the law (Facchi *et al.*, 2001a; Mariano *et al.*, 2001)

$$w(\Delta - \Delta_0) = \frac{1}{\pi} \frac{1}{\sqrt{2\sigma^2 - (\Delta - \Delta_0)^2}}, \tag{199}$$

for $|\Delta - \Delta_0| \leq \sqrt{2}\sigma$ and 0 otherwise, with standard deviation $(\int \Delta^2 w(\Delta)\, d\Delta)^{1/2} = \sigma$. From an experimental perspective this is more convenient and easier to reproduce than the Gaussian distribution in Eq. (195). Indeed, Eq. (199) follows from a phase $\Delta(t) = \Delta_0 + \sqrt{2}\sigma \sin t$, where t ("time") is a parameter, uniformly distributed between 0 and 2π, namely, $w(\Delta) = \int_0^{2\pi} dt\, \delta(\Delta - \sqrt{2}\sigma \sin t)/2\pi$. (One can require $\sqrt{2}\sigma \leq \Delta_0$, in order that $\Delta(t)$ be positive—and the term $\sqrt{2}\sigma \sin t$ be regarded as a "small" fluctuation around the average value. However, strictly speaking, this is not necessary from a mathematical point of view.) From Eqs. (199) and (172) the

following is derived:

$$\Omega(p) = \int_{-\sqrt{2}\sigma}^{\sqrt{2}\sigma} \frac{d\Delta}{\pi} \frac{e^{i\frac{p\Delta}{\hbar}}}{\sqrt{2\sigma^2 - \Delta^2}} = \int_{-\pi/2}^{\pi/2} \frac{dt}{\pi} \exp\left(i\frac{\sqrt{2}p\sigma}{\hbar}\sin t\right) = J_0\left(\frac{\sqrt{2}p\sigma}{\hbar}\right), \tag{200}$$

where J_0 is the Bessel function of order zero. The decoherence parameter in Eq. (194) reads

$$\varepsilon = 1 - \max_{\Delta_0}\left|\int dp\, P_{\text{in}}(p) J_0\left(\frac{\sqrt{2}p\sigma}{\hbar}\right)\cos\left(\frac{p\Delta_0}{\hbar}\right)\right| \tag{201}$$

and for a monochromatic beam one obtains ($k = p/\hbar$)

$$\varepsilon_k = 1 - \max_{\Delta_0}\left|J_0\left(\frac{\sqrt{2}p\sigma}{\hbar}\right)\cos\left(\frac{p\Delta_0}{\hbar}\right)\right| = 1 - \left|J_0\left(\sqrt{2}k\sigma\right)\right|. \tag{202}$$

This function is shown in Figure 39(b): observe that decoherence is *not* a monotonic function of the noise σ in Eq. (199).

A comparison between Figures 39(a) and 39(b) is interesting. In both cases, fragility at high momenta $p = \hbar k$ is observed. However, the behavior of decoherence in Figure 39(b) is somewhat anomalous and against naive expectation. For a given k, there are situations where decoherence ε *decreases by increasing* the strength of the fluctuations σ. Note also that we are considering incoming monochromatic beams, whence, according to Eqs. (189) and (194),

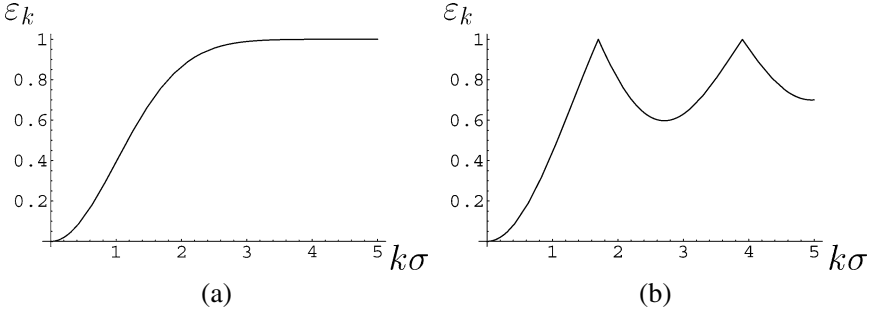

FIGURE 39. (a) Decoherence parameter ε_k (198) versus $k\sigma$, for a monochromatic beam interacting with a shifter fluctuating according to Eq. (195). (b) Decoherence parameter ε_k (202) versus $k\sigma$, for a monochromatic beam interacting with a shifter fluctuating according to Eq. (199).

$\varepsilon_k = 1 - \mathcal{V}(\hbar k)$ and the decoherence parameter is strictly related to the standard visibility of the interference pattern. Therefore, in the anomalous regions, an increase in visibility is observed by increasing the fluctuations of the phase shifter, a phenomenon somewhat similar to stochastic resonance (Benzi *et al.*, 1981, 1983). This is true not only for monochromatic beams, but also for narrow distributions (packets) in momentum space.

These anomalous results are not entirely surprising compared with other known results in classical optics. The visibility of a classical interference experiment can be expressed as the Fourier transformation of the spectral distribution of a quasi-monochromatic light source, and it displays some "anomalies" even in cases that are different from our "Gaussian" example in Eq. (193). See Born and Wolf's (1999) book and Facchi *et al.* (2003).

C. Wigner Function in the Ordinary Channel

In the previous subsections we proposed a definition of decoherence based on the visibility of the quantum interference pattern. As seen, this definition has some unexpected features, somewhat at variance with expectation. However, alternative definitions of decoherence are possible, based on the density matrix and on the Wigner function, whose definition and properties were reviewed in Section III.H. For a squeezed or a Gaussian state, one obtains essentially Eq. (86)

$$W(x,k) = \frac{1}{\pi}\exp\left[-\frac{(x-x_0)^2}{2\delta^2}\right]\exp\left[-2\delta^2(k-k_0)^2\right], \tag{203}$$

where x and $p = \hbar k$ are the position and momentum of the particle and δ is the squeezing parameter. Consider now a neutron wave packet that is split and then recombined in an interferometer, with a phase shifter Δ placed in one of the two routes. The Wigner function in the ordinary channel (transmitted component) is readily computed:

$$\begin{aligned} &W_{\mathrm{O}}(x,k,\Delta) \\ &\quad= \frac{1}{4\pi}\exp\left[-2\delta^2(k-k_0)\right]\left[\exp\left(-\frac{(x-x_0+\Delta)^2}{2\delta^2}\right)\right. \\ &\quad\left.+\exp\left(-\frac{(x-x_0)^2}{2\delta^2}\right)+2\exp\left(-\frac{(x-x_0+\frac{\Delta}{2})^2}{2\delta^2}\right)\cos(k\Delta)\right]. \end{aligned} \tag{204}$$

This result is slightly different from Eq. (88) because the phase shifter is now placed in only one of the two routes (see Figure 36). Again, for $\Delta \neq 0$, the above expression is not normalized to unity (some neutrons end up in the extraordinary channel—reflected component). For $\Delta = 0$ (no phase shifter), Eq. (203) is recovered.

D. Alternative Definition of Decoherence

We look at a particular case and assume that the shifts Δ fluctuate around their average Δ_0 according to the Gaussian law [Eq. (195)]. The average Wigner function is stated as

$$\overline{W}(x,k) = \int d\Delta w(\Delta) W(x,k,\Delta) \tag{205}$$

and represents a partially mixed state. Essentially, this Wigner function represents the whole ensemble of neutrons in an experimental run. For the double Gaussian state [Eq. (204)], obtained when a neutron beam crosses an interferometer, the average Wigner function in the ordinary channel is stated as

$$\begin{aligned}\overline{W}_{\mathrm{O}}(x,k) = {} & \frac{\exp[-2\delta^2(k-k_0)^2]}{4\pi} \\ & \times \left\{ \exp\left[-\frac{x^2}{2\delta^2}\right] + \sqrt{\frac{\delta^2}{\delta^2+\sigma^2}} \exp\left[-\frac{(x+\Delta_0)^2}{2(\delta^2+\sigma^2)}\right] \right. \\ & + 2\sqrt{\frac{\delta^2}{\delta^2+\frac{\sigma^2}{4}}} \exp\left[-\frac{(x+\frac{\Delta_0}{2})^2 + k^2\delta^2\sigma^2}{2(\delta^2+\frac{\sigma^2}{4})}\right] \\ & \left. \times \cos\left(k\frac{2\delta^2\Delta_0 - x\sigma^2}{2(\delta^2+\frac{\sigma^2}{4})}\right) \right\},\end{aligned} \tag{206}$$

where we set $x_0 = 0$ for simplicity. Its momentum marginal (the momentum distribution function) can be computed analytically and is of interest, because it displays fragility at high momenta (Badurek *et al.*, 2000b; Rauch and Suda, 1995, 1997; Rauch *et al.*, 1999):

$$P(k) = \sqrt{\frac{\delta^2}{2\pi}} \exp\left[-2\delta^2(k-k_0)^2\right]\left[1 + \exp\left(-\frac{k^2\sigma^2}{2}\right)\cos(k\Delta_0)\right]. \tag{207}$$

The average Wigner function in Eq. (206) is shown in Figure 40. A strong (exponential) suppression of interference is observed at high values of k. Notice that the oscillating part of the Wigner function is bent toward the negative x-axis. This is due to the x-dependence of the cosine term in Eq. (206) that entails different frequencies for different values of x.

The loss of quantum coherence is clearly visible in Figure 40 as the level of noise σ increases. An attempt can be made to corroborate this qualitative conclusion by introducing a quantitative notion of decoherence based on the Wigner function; however, as we shall see later, the same kind of difficulties

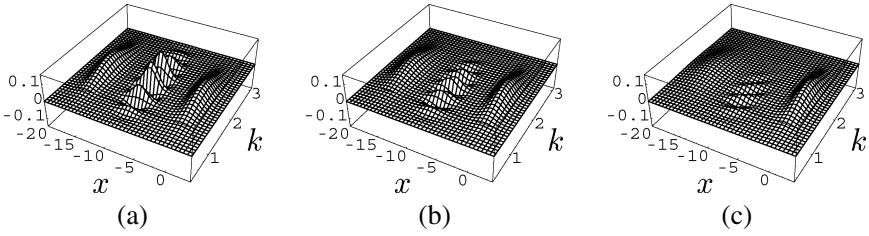

FIGURE 40. Wigner function in the ordinary channel Eq. (206) for different values of the standard deviation σ in Eq. (195). From left to right, $\sigma = 0, 0.9, 1.8$ Å. We set $x_0 = 0$, $k_0 = 1.7$ Å^{-1}, $\delta = 1.1$ Å, $\Delta_0 = 16.1$ Å. Position x and momentum k are measured in Å and Å^{-1}, respectively. Notice the strong suppression of interference at large values of momentum, both in (b) and (c). The interference term in Eq. (206) depends on x and the oscillating part of the Wigner function is bent toward the negative x-axis.

are encountered as in Section IX.B. First recall that there is an interesting relation between the square of the Wigner function and the square of the density matrix:

$$\int dx\, dk W(x,k)^2 = \frac{\mathrm{Tr}\,\hat{\rho}^2}{2\pi}. \tag{208}$$

It is therefore possible to define an alternative decoherence parameter (Facchi *et al.*, 2001a; Mariano *et al.*, 2001), that takes into account the coherence properties of the neutron ensemble

$$\varepsilon = 1 - \frac{\mathrm{Tr}\,\hat{\rho}^2}{(\mathrm{Tr}\,\hat{\rho})^2} = 1 - \frac{2\pi \int dx\, dk \overline{W}(x,k)^2}{(\int dx\, dk \overline{W}(x,k))^2}. \tag{209}$$

This quantity measures the degree of "purity" of a quantum state: it is maximum when the state is maximally mixed ($\mathrm{Tr}\,\hat{\rho}^2 < \mathrm{Tr}\,\hat{\rho}$) and vanishes when the state is pure ($\mathrm{Tr}\,\hat{\rho}^2 = \mathrm{Tr}\,\hat{\rho}$). In the former case, the fluctuations of Δ are large and the quantum mechanical coherence is completely lost, whereas in the latter case, Δ does not fluctuate and the quantum mechanical coherence is perfectly preserved. The parameter in Eq. (209) was introduced within the framework of the so-called many Hilbert space theory of quantum measurements (Namiki *et al.*, 1997) and yields a quantitative estimate of decoherence. The related quantity $\mathrm{Tr}\,\hat{\rho} - \mathrm{Tr}\,\hat{\rho}^2$ was first considered by Watanabe in 1939. A quantity related to ε was also introduced to derive a quantitative estimate of information for a quantum system (Brukner and Zeilinger, 1999).

It is also noteworthy that the notion of decoherence just introduced is based on the square of the density matrix (or Wigner function) and therefore is

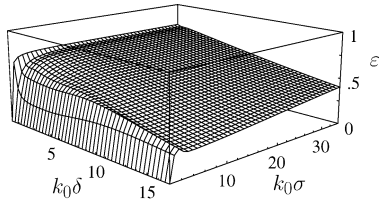

FIGURE 41. Decoherence parameter versus coherence length of the wave packet δ and standard deviation of the fluctuation σ for a double Gaussian wave packet [Eq. (204)] in the ordinary channel of an MZI. We set $k_0\Delta_0 = 27.4$. The decoherence parameter is not a monotonic function of σ for every value of δ. Notice that ε never reaches unity ($\varepsilon \leq 3/4$); this is due to the fact that only one Gaussian (in one branch of the interferometer) undergoes statistical fluctuations (see [Eq. (206)] and Figure 40).

not accessible to a direct measurement procedure. In this sense, it is less "operational" than that discussed in Section IX.B.

The decoherence parameter in Eq. (209) is shown in Figure 41 as a function of the coherence length of the wave packet δ in Eq. (204) and the standard deviation of the fluctuations σ. It is *not* a monotonic function of σ for all values of δ. Again, as in Section IX.B, there are situations in which a larger noise yields a more coherent wave packet (according to a given definition). The behavior of ε has a nontrivial dependence both on the fluctuations (σ) and on the wave packet properties (k_0 and δ).

E. Entropy

The conclusions of the previous subsections can be corroborated and put on a somewhat sounder basis by computing the entropy of the distribution of the shifts according to the formula

$$S = -\int d\Delta w(\Delta) \log w(\Delta). \tag{210}$$

This quantity yields an estimate of the collective "degree of disorder" of the distribution of the shifts $w(\Delta)$. General conclusions can be drawn about the behavior of S as a function of a parameter σ characterizing the width of the distribution. For instance, let $w(\Delta;\sigma)$ be the symmetric distribution with the properties in Eq. (169), with σ as its standard deviation. By assuming that the distribution function w depends only on the single dimensional parameter σ, then it must scale according to

$$w(\Delta;\sigma) = \frac{1}{\sigma} w\left(\frac{\Delta}{\sigma}; 1\right). \tag{211}$$

Therefore

$$\begin{aligned} S(\sigma) &= -\int d\Delta w(\Delta;\sigma)\log w(\Delta;\sigma) \\ &= -\int \frac{d\Delta}{\sigma} w\left(\frac{\Delta}{\sigma};1\right)\log\left[\frac{1}{\sigma}w\left(\frac{\Delta}{\sigma};1\right)\right] \\ &= -\int d\Delta' w(\Delta';1)\log w(\Delta';1) + \int d\Delta' w(\Delta';1)\log\sigma \\ &= S(1)+\log\sigma, \end{aligned} \tag{212}$$

where $S(1)$ is independent of σ and depends only on the form of the distribution function. $S(\sigma)$ is clearly an increasing function of σ.

For example, the Gaussian distribution in Eq. (195) yields the following (Suda, 1995):

$$S(\sigma) = \log\sigma + \frac{1}{2}\log(2\pi e), \tag{213}$$

whereas the "sine" distribution in Eq. (199) yields

$$S(\sigma) = \log\sigma - \frac{1}{2}\log 2. \tag{214}$$

Therefore the behavior of the decoherence parameter ε as a function of the entropy S of the shifts is qualitatively equivalent to its behavior as a function of the standard deviation σ. Indeed, Figures 38, 39, and 41 would differ only for a logarithmic scale on the abscissas. As shown above, in general, the two quantities S and ε do not necessarily agree; in other words, the loss of quantum mechanical coherence is not necessarily larger when the neutron beam interacts with fluctuating shifts of larger entropy.

X. Quantum Tomography of Neutron Wave Packets

The previous sections were devoted to the different aspects of neutrons that can be used for imaging and sensing. As has been shown, various objects or fields can be characterized via their actions on particular degrees of freedom of the particles used. We have considered the influence of the environment on the neutron number, phase, and interference and the ability of the environment to act as a which-way detector. Most generally, the process of imaging can be described as follows. The particles used for imaging are prepared in an initial quantum state. The objects or fields we want to characterize then interact with the particles, which results in an overall transformation of the input state. Finally, the output particles are measured and the transformation we are interested in is inferred from the result of this measurement. This problem

is usually underdetermined and only certain aspects of the transformation are accessible based on the collected data. Obviously, in order to completely specify the general transformation of a quantum state, repeated measurements must be used with different known input states. But even in neutron optics, where the input state of neutrons cannot be easily controlled an improvement of imaging can be expected, provided simple final measurements are replaced by the complete tomography of the output neutrons. The following text describes a setup for tomography of spatial degrees of freedom neutrons.

A. Experimental Setup for the Complete Tomography of Neutrons

The set of measurements that can be done on neutrons to determine their quantum state is severely limited by the very low time resolution of the available detectors. In quantum optics, this obstacle can be overcome by mixing the weak input field with a strong local oscillator. By changing the phase ϕ of the oscillator, the spectral decompositions of all quadratures can be measured as

$$\widehat{X}_\phi = \hat{x}\cos\phi + \hat{p}\sin\phi, \tag{215}$$

where $\hat{x}$ and $\hat{p}$ are the canonically conjugated operators of position and momentum. Of course, no such local oscillators exist for neutrons. However, massive particles experience a transformation of the type in Eq. (215) in the course of free evolution: $\hat{x}(t) = \hat{x} + (\hat{p}/m)t$, where m is the mass. Thus, free evolution of the wave packet followed by a position-sensitive measurement yields information about a subset of quadratures $\widehat{X}_\phi$, $\phi \in [0, \pi/2]$. For example, Kurtsiefer *et al.* (1997) used free evolution for the reconstruction of transversal motional states of helium atoms. Here we are interested in the *longitudinal* degrees of freedom. Since neutron detectors have very bad time resolution, free evolution *alone* cannot be used to generate a tomographically complete set of measurements.

Feasible measurements on thermal neutrons consist of (1) measurements of the contrast and phase of interference fringes in an interferometric setup (see Figure 42, without momentum kick), and (2) spectral analysis of the neutron beam using an adjustable Bragg-reflecting crystal plate together with a position-sensitive detector. This set of observables is *not* tomographically complete because the measurable (complex) contrast of the interference pattern (Rauch and Werner, 2000a) ($\hbar = 1$),

$$\Gamma(\Delta x) = \langle\psi|e^{i\Delta x\hat{p}}|\psi\rangle = \int |a(p)|^2 e^{i\Delta x\hat{p}}dp, \tag{216}$$

where $a(p) = \langle p|\psi\rangle$ is not sensitive to the phase of $a(p)$ and no information about quadratures other than p is available.

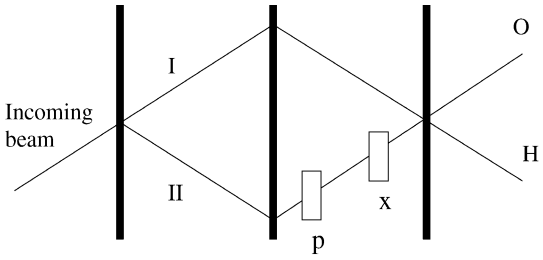

FIGURE 42. Scheme of a perfect-crystal neutron interferometer. The incoming beam is split at the first crystal plate, reflected at the middle plate, and recombined again at the third plate. The detector is placed in beam O where the visibility is higher due to the same number of reflections/transmissions. In addition to a position shift Δx routinely used in neutron experiments, a momentum kick Δp has been added in path II to make the interferometric measurement tomographically complete; see text for details.

Obviously, the situation would be different if both the position (phase) *and* the momentum of the incoming wave packet could be shifted inside the interferometer. Such a thought experiment is shown in Figure 42. In that case, the Wigner function describing the ensemble of measured neutrons would be related to the measured contrast

$$\Gamma(\Delta p, \Delta x) = \mathrm{Tr}\{\hat{\rho} e^{i\Delta p \hat{x}} e^{i\Delta x \hat{p}}\} = \int e^{i(\Delta p)x} \langle x|\hat{\rho}|x + \Delta x\rangle \, dx \quad (217)$$

by a simple integral transformation

$$W(x, p) = \int\int e^{-i\frac{uv}{2} + iux + ivp} \Gamma(-u, v) \, du \, dv, \quad (218)$$

where $u = \Delta p$, $v = \Delta x$ and $\hat{\rho}$ is the density matrix.

Although this thought experiment appears simple, its experimental realization, according to Figure 42, would be rather difficult. Large momentum kicks acquired by the neutron in the lower arm would change its de Broglie wavelength and spoil the Bragg reflection at the last crystal plate. Therefore we now propose a modified scheme that can substitute the interferometric setup of Figure 42.

B. Setup

In the scheme shown in Figure 43, the incoming neutrons polarized in the $+z$ direction, $|\Psi\rangle = |\psi\rangle|z_+\rangle$, where ψ denotes the spatial degrees of freedom, first propagate freely through a distance L, undergoing a unitary operation $U_1 = \exp[-i\hat{p}^2 L/(2p_0)]$. In the following, we assume that the input wave packets are quasi-monochromatic, $\sigma_p \ll p_0$, with a central momentum p_0.

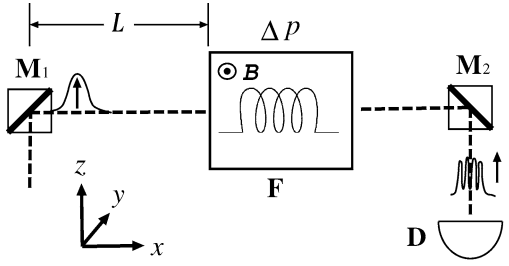

FIGURE 43. Setup for the tomography of motional states of neutrons. M_1, M_2, Magnetic mirrors; L, region of free propagation; B, static magnetic field controlling the momentum kick Δp; F, box containing a static magnetic field (aligned along $+y$) and an radiofrequency (RF) coil; D, detector. The arrows denote the polarization of neutrons after reflections from magnetic mirrors.

This condition guarantees that the action of the radiofrequency (RF) coil is practically equivalent to a momentum "kick." After the region of free propagation, the neutrons are let through an RF coil placed in a static magnetic field polarized along the $-y$ direction (see Figure 43). As a result of the interaction between the neutron and the coil, the y_+ (y_-) component of the input state will be accelerated (decelerated). Assuming that the region of interaction is short, so that the dispersion of the wave packet of the neutron can be neglected in the coil, in the quasi-monochromatic approximation, the net momentum transfer can be described by the effective unitary operator,

$$U_2 = e^{i\Delta p\hat{x}/2}|y_+\rangle\langle y_+| + e^{-i\Delta p\hat{x}/2}|y_-\rangle\langle y_-|, \tag{219}$$

where

$$\Delta p = \frac{2\mu Bm}{p_0}. \tag{220}$$

Prior to detection, the particles are polarized along the $+z$ direction again to erase the which-way information stored in the polarization degree of freedom. The probability of a neutron being detected is given by the norm of the transmitted component,

$$P = \mathrm{Tr}\{\Pi(\Delta p, \Delta x)\hat{\rho}\}, \tag{221}$$

where $\hat{\rho}$ refers only to the spatial degrees of freedom and

$$\begin{aligned}\Pi(\Delta p, \Delta x) &= \langle z_+|U_1^\dagger U_2^\dagger|z_+\rangle\langle z_+|U_2U_1|z_+\rangle &(222)\\ &= 1/2 + e^{i\frac{L}{2p_0}\hat{p}^2}e^{i\Delta p\hat{x}}e^{-i\frac{L}{2p_0}\hat{p}^2}/4 + \text{h.c.}\\ &= 1/2 + e^{i\Delta p(\hat{x}+L\hat{p}/p_0)}/4 + \text{h.c.} &(223)\\ &= 1/2 + e^{i\Delta x\hat{p}}e^{i\Delta p\hat{x}}e^{-i\Delta x\Delta p/2}/4 + \text{h.c.}, &(224)\end{aligned}$$

where we denoted

$$\Delta x = \frac{\Delta p L}{p_0} = \frac{2\mu B m L}{p_0^2}. \tag{225}$$

C. Radon Inversion

Notice, that the positive operator-valued measure elements in Eq. (223) can also be restated in terms of quadrature operators,

$$\widehat{\Pi}(\Delta p, \Delta x) = (1/4)\left(1 + e^{i\omega \widehat{X}_\theta}\right) + \text{h.c.}, \tag{226}$$

where (in fixed units)

$$\widehat{X}_\theta = \cos\theta \hat{x} + \sin\theta \hat{p}, \qquad \tan\theta = \frac{\Delta x}{\Delta p} = \frac{L}{p_0}, \tag{227}$$

and $\omega = \sqrt{\Delta x^2 + \Delta p^2}$. Thus, for a fixed θ, the data contain information about the characteristic function of the quadrature $\widehat{X}_\theta$,

$$P(\Delta p, \Delta x) = 1/2 + \text{Re}\left\{C_{X_\theta}(\omega)\right\}/2, \tag{228}$$

$$\left\langle C_{X_\theta}(\omega)\right\rangle = \int P_{X_\theta}(x) e^{i\omega x}\, dx. \tag{229}$$

By changing L one changes the quadrature measured, while ω, which depends on both L and B, determines the observed spatial frequency of the probability distribution of this quadrature. The observed quadratures range from $\hat{x}$ (for $L = 0$) to $\hat{p}$ (for $L \to \infty$). From the measurement of $C_{X_\theta}(\omega)$, the "shadows" $P_{X_\theta}(x)$ of the Wigner function can be obtained by the Fourier transformation, which in turn yield the Wigner function by an inverse Radon transformation described in Section III.J.

Since the contrast $\Gamma(\Delta p, \Delta x)$ is essentially the Fourier transformation of the Wigner function $W(x, p)$ [see Eq. (218)], the largest values of Δp and Δx are related to the smallest resolved details in x and p, respectively. Namely, (reinserting $\hbar$),

$$(\Delta p)_{\text{MAX}} = \hbar/(\delta x)_{\text{min}}, \qquad (\Delta x)_{\text{MAX}} = \hbar/(\delta p)_{\text{min}}, \tag{230}$$

where $(\delta x)_{\text{min}}$ and $(\delta p)_{\text{min}}$ denote the x and p resolutions. Eqs. (220) and (225) yield

$$(\delta x)_{\text{min}} = \frac{\hbar}{2\mu m}\frac{p_0}{B_{\text{MAX}}}, \qquad (\delta p)_{\text{min}} = \frac{p_0}{L}(\delta x)_{\text{min}}. \tag{231}$$

For a neutron of wavelength $\lambda_0 = 0.37$ nm (Badurek *et al.*, 2000b), assuming the reasonable values $L_{\text{MAX}} = 1$ m and $B_{\text{MAX}} = 0.1$ T, one gets $(\delta x)_{\text{min}} = 60$ μm and $(\delta p)_{\text{min}} = \hbar \times 10^6$ m^{-1}.

D. Statistical Inversion

The procedure outlined above, based on the direct inversion formula in Eq. (218), has several drawbacks. (1) Realistic data are always noisy. In that case, formula (218) can yield unphysical results, such as the Wigner representation of a nonpositive definite operator. (2) The Wigner function in Eq. (218) depends on the measured data indirectly through the complex degree of coherence Γ, which itself has to be estimated with the help of an auxiliary position shifter. This intermediate step is, certainly, not necessary as all available information about the Wigner function of the incoming neutrons is contained in the raw data measured without any auxiliary position shift. To avoid these problems, we propose use of the ML quantum state reconstruction (Hradil, 1997; Řeháček *et al.*, 2001; Paris and Řeháček, 2004). The main advantages of this method compared with the above direct inversion are as follows. (1) Asymptotically, for large data samples it provides the best performance available. (2) Any prior information about the measured neutrons and the known statistics of the experiment can be used to increase the accuracy of the reconstruction. (3) The existing physical constraints can be easily incorporated into the reconstruction. Most notably, this technique guarantees the positivity of the reconstructed density operator. (4) It can be applied directly to raw counted data.

Assuming that the statistics of the experiment are Poissonian, the ML reconstruction consists in minimizing the Kullback–Leibler distance (relative entropy) between the measured data $f(\Delta x, \Delta p)$ and the renormalized theoretical probabilities $P(\Delta x, \Delta p)/\sum P$, of Eq. (228). This problem is a quantum generalization of the ML transmission tomography discussed in Section V. As shown by Hradil (1997) and Řeháček *et al.* (2001), the ML density matrix can be obtained as a fixed point of the iterations of a nonlinear operator map. In this point the likelihood functional must be stationary. Decomposing the density matrix as follows: $\hat{\rho} = \hat{A}^\dagger \hat{A}$, this condition reads,

$$\frac{\partial}{\partial \hat{A}} \log \mathcal{L}\big(\hat{A}^\dagger \hat{A}\big) = \frac{\partial}{\partial \hat{A}} \sum_j f_j \frac{p_j}{\sum_{j'} p_j} = \widehat{R}\hat{A}^\dagger - \widehat{G}\hat{A}^\dagger = 0, \qquad (232)$$

where

$$\widehat{R} = \sum_j \frac{f_j}{p_j} \widehat{\Pi}_j, \qquad \widehat{G} = \frac{\sum_{j'} f_{j'}}{\sum_{j''} p_{j''}} \sum_j \widehat{\Pi}_j, \qquad (233)$$

and the parameters Δx and Δp have been discretized and replaced by a collective index $j \equiv \{\Delta x_j, \Delta p_j\}$. Multiplying the last equality of Eq. (232) by A and rearranging we get the expression for the i-th iteration of the ML

state:

$$\hat{\rho}^i = \widehat{G}^{-1}\widehat{R}\hat{\rho}^{i-1}\widehat{R}\widehat{G}^{-1}. \tag{234}$$

A good starting point is the maximally mixed state $\hat{\rho}^0 = \hat{1}/d$. This algorithm was applied to computer-generated data to test the realistic performance of the proposed setup in Figure 43.

E. Simulation

As follows from the parameter estimates given after Eq. (231), the proposed tomography scheme using thermal neutrons will likely have sufficient resolution in momentum. On the other hand, even for well-monochromatized thermal beams, the resolution in position is expected to be several orders of magnitude worse than typical coherence lengths. The simulations in Figure 44 illustrate the effect of the restricted range of Δp on the reconstruction. Consider first a measurement of a minimum uncertainty Gaussian wave packet that is in the moving frame parameterized by its coherence length, $|\Psi_G\rangle \propto \int \exp(-k^2 l_{\text{coh}}^2)|k\rangle\, dk$. Provided the apparatus has a sufficient spatial resolution, $\delta x_{\min} < l_{\text{coh}}$, a faithful reconstruction is readily obtained (upper left panel of Figure 44). More realistic measurement with $\delta x_{\min} \gg l_{\text{coh}}$ would obviously yield the Wigner function smoothed out substantially along the x axis. However, the states measured in a real experiment will not be minimum uncertainty states. Instead, the experimenter deals with time-evolved states

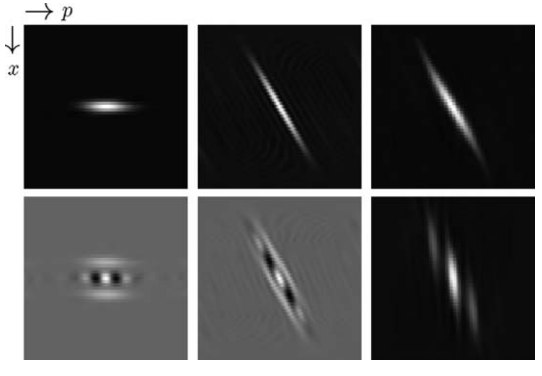

FIGURE 44. Reconstructed Wigner functions of Gaussian states (upper row) and superpositions of Gaussian states ("cats;" lower row) from simulated data. A 50 × 50 matrix of Δx and Δp shifts was used for the ML inversion. Left column: reconstructed original states; middle column: reconstructed time-evolved states; right column: reconstructed time-evolved states with reduced resolution, $\delta x_{\min}/l_{\text{coh}} \approx 10$. In each frame, the regions lighter than the edges represent positive values. The regions darker than the edges represent negative values.

$|\Psi(T)\rangle = U(T)|\Psi_G\rangle \propto \int \exp(ik^2T - k^2l_{\rm coh}^2)|k\rangle\, dk$ that are strongly affected by dispersion. As a consequence, the wave packet spread δT very soon becomes larger than the resolution limit, $\delta T = \sqrt{l_{\rm coh}^2 + T^2/l_{\rm coh}^2} \gg \delta x_{\rm min}$, and good reconstruction can be achieved with a realistic apparatus. Compare the upper middle and upper right panels in Figure 44, which show reconstructions with sufficient and reduced but more realistic resolutions of $\delta x_{\rm min} \approx l_{\rm coh}/2$ and $\delta x_{\rm min} \approx 10 l_{\rm coh}$, respectively.

Imaging of nonclassical states is a much more delicate problem. Let us consider superpositions of spatially separated Gaussian states (Schrödinger cats), $|\Psi_{\rm cat}\rangle \propto [1 + U(\Delta)]|\Psi_G\rangle = \int [1 + \exp(ik\Delta)]|\Psi_G\rangle$. Such states can be prepared, for example, by means of a double-loop perfect-crystal interferometer (Baron *et al.*, 2003). As shown by Badurek *et al.* (2000b), the preparation of thermal neutron cat states with separations exceeding the corresponding coherence lengths of the individual components, $\Delta \gg l_{\rm coh}$, is possible. Provided the apparatus has sufficient resolution, the nonclassical character of this state is manifested by the negative regions of the reconstructed Wigner function (lower left panel of Figure 44). Taking into account the vacuum dispersion, $|\Psi_{\rm cat}(T)\rangle = U(T)|\Psi_{\rm cat}\rangle$, the ordering of the relevant parameters will likely proceed as follows: $l_{\rm coh} \ll \Delta \ll \delta x_{\rm min} \ll \delta T$. As simulations show, a realistic measurement whose position resolution is much worse than the coherence lengths of the individual cat state components tends to wipe out the negative regions of the reconstructed Wigner function (compare the lower middle and lower right panels of Figure 44). On the other hand, the primary features of such exotic states, such as their non-Gaussian character and the global spatial properties (of which little is known today), should still be accessible to a realistic wave packet tomography. To resolve more subtle quantum interference effects of the order of the coherence length, more refined experimental techniques may be needed. An idea could be to replace thermal neutrons by ultracold neutrons, for which much larger momentum shifts Δp (and thus much smaller $\delta x_{\rm min}$) can be obtained.

XI. CONCLUSIONS

The purpose of this chapter was to provide an overview of recent important improvements in imaging techniques for thermal neutron beams. On one hand, we have shown that a statistically correct data handling can significantly enhance well-known imaging methods, such as transmission tomography. Sometimes, especially in imaging, where coherent effects play a major role, this enhancement becomes crucial. Due to the extremely low coherent intensities of present thermal neutron sources, phase-contrast tomography with

thermal neutrons would hardly be possible without extracting all available information on the object and the neutron beam itself.

On the other hand, we introduced some novel imaging methods that are based on the genuinely quantum properties of neutrons. We have shown how quantum interference and repeated measurements, hinging on the QZE, can be used for the purpose of a safer neutron radiography. In a similar spirit, the fast decoherence of nonclassical neutron states in an interferometer, together with a complete quantum-state tomography, can be used to achieve a highly sensitive quantum imaging of fields and noise. These last techniques are still an experimental challenge today, but one can realistically hope that in the near future they will significantly push forward the limits of imaging with thermal neutron beams.

ACKNOWLEDGMENTS

We gratefully acknowledge support by the Bilateral Research Program between Italy and the Czech Republic PH1 on "Decoherence and Quantum Measurements," by Project MSM6198959213 of the Czech Ministry of Education, and by the East–West program of the Austrian Academy of Sciences.

REFERENCES

Akhiezer, A.I., Berestetsky, V.B. (1965). *Quantum Electrodynamics*. Interscience, New York.

Allman, B.E., McMahon, P.J., Nugent, K.A., Paganin, D., Jacobson, D.L., Arif, M., Werner, S.A. (2000). *Nature* **408**, 158.

Altenmüller, T.P., Schenzle, A. (1994). *Phys. Rev. A* **49**, 2016.

Badurek, G., Rauch, H., Zeilinger, A., Bauspiess, W., Bonse, U. (1976). *Phys. Rev. D* **14**, 1177.

Badurek, G., Rauch, H., Zeilinger, A. (1988). *Matter Wave Interferometry*. North-Holland, Amsterdam.

Badurek, G., Buchelt, R.J., Leeb, H. (2000a). *Physica B* **276**, 588.

Badurek, G., Rauch, H., Suda, M., Weinfurter, H. (2000b). *Optics Communications* **179**, 13.

Balzer, C., Huesmann, R., Neuhauser, W., Toschek, P.E. (2000). *Opt. Comm.* **180**, 115.

Barnett, S.M., Pegg, D.T. (1996). *Phys. Rev. Lett.* **76**, 4148.

Baron, M. (2005). *Messung von Quantenzuständen im Neutroneninterferometer*. Ph.D. thesis, Vienna University of Technology.

Baron, M., Rauch, H., Suda, M. (2003). *J. Opt. B: Quantum and Semiclass. Opt.* **5**, S241.
Bauspiess, W., Bonse, U., Rauch, H. (1978). *Nucl. Instr. and Meth.* **157**, 495.
Beckmann, F., Bonse, U., Busch, F., Günnewig, O. (1997). *J. Comput. Assist. Tomogr.* **21**, 539.
Beige, A., Hegerfeldt, G. (1996). *Phys. Rev. A* **53**, 53.
Benzi, R., Sutera, A., Vulpiani, A. (1981). *J. Phys. A* **14**, L453.
Benzi, R., Sutera, A., Parisi, G., Vulpiani, A. (1983). *SIAM J. Appl. Math.* **43**, 565.
Berry, M. (1995). In: Greenberger, D.M., Zeilinger, A. (Eds.), *Fundamental Problems in Quantum Theory*, vol. 755. Ann. N.Y. Acad. Sci., New York, p. 303.
Blanchard, Ph., Jadczyk, A. (1993). *Phys. Lett. A* **183**, 272.
Bohr, N. (1983). Discussion with Einstein on epistemological problems in atomic physics. In: Wheeler, J.A., Zurek, W.H. (Eds.), *Quantum Theory and Measurement*. Princeton University Press, Princeton.
Bonse, H., Rauch, H. (Eds.) (1979). *Neutron Interferometry*. Clarendon, Oxford.
Bonse, U., Hart, M. (1965). *Appl. Phys. Lett.* **6**, 155.
Bonse, U., Nusshardt, R., Busch, F., Pahl, R., Kinney, J.H., Johnson, Q.C., Saroyan, R.A., Nichols, M.C. (1991). *Journal of Materials Science* **26**, 4076.
Born, M., Wolf, E. (1999). *Principles of Optics*, 7th ed. Cambridge University Press, Cambridge.
Brukner, Č., Zeilinger, A. (1999). *Phys. Rev. Lett.* **83**, 3354.
Carruthers, P., Nieto, M.M. (1968). *Rev. Mod. Phys.* **40**, 411.
Chizhov, A.V., De-Renzi, V., Paris, M.G.A. (1998). *Phys. Lett. A* **237**, 201.
Cimmino, A., Opat, G.I., Klein, A.G., Kaiser, H., Werner, S.A., Arif, M., Clothier, R. (1989). *Phys. Rev. Lett.* **63**, 380.
Colella, R., Overhauser, A.W., Werner, S.A. (1975). *Phys. Rev. Lett.* **34**, 1472.
Cook, R.J. (1988). *Phys. Scr. T* **21**, 49.
Dempster, A.P., Laird, N.M., Rubin, D.B. (1977). *J. R. Statist. Soc. B* **39**, 1.
Dicke, R.H. (1981). *Am. J. Phys.* **49**, 925.
Dicke, R.H. (1986). *Found. Phys.* **16**, 107.
Dubus, F., Bonse, U., Biermann, T., Baron, M., Beckmann, F., Zawisky, M. (2002). *SPIE Proc.* **4503**, 259.
Dubus, F., Bonse, U., Zawisky, M., Baron, M., Loidl, R. (2005). First phase-contrast tomography with thermal neutrons. In: *Proc. 7th World Conference on Neutron Radiography, Rome 2002*, ISBN 88-8286-199-6, p. 263; short version published in: *IEEE Transactions on Nuclear Science* **52**, 364.
Elattari, B., Gurvitz, S.A. (2000). *Phys. Rev. A* **62**, 032102.

Elitzur, A.C., Vaidman, L. (1993). *Found. Phys.* **23**, 987.
Englert, B.G. (1996). *Phys. Rev. Lett.* **77**, 2154.
Facchi, P., Pascazio, S. (2000). *Phys. Rev. A* **62**, 023804.
Facchi, P., Pascazio, S. (2001). In: Wolf, E. (Ed.), In: *Progress in Optics*, vol. 42. Elsevier, Amsterdam, p. 147.
Facchi, P., Mariano, A., Pascazio, S. (2001a). *Phys. Rev. A* **63**, 052108.
Facchi, P., Pascazio, S., Nakazato, H., Řeháček, J., Periňa, J. (2001b). *Phys. Lett. A* **279**, 117.
Facchi, P., Nakazato, H., Pascazio, S. (2001c). *Phys. Rev. Lett.* **86**, 2699.
Facchi, P., Hradil, Z., Krenn, G., Pascazio, S., Řeháček, J. (2002). *Phys. Rev. A* **66**, 012110.
Facchi, P., Mariano, A., Pascazio, S., Suda, M. (2003). *J. Opt. B: Quantum Semiclass. Opt.* **5**, S290.
Facchi, P., Tasaki, S., Pascazio, S., Nakazato, H., Tokuse, A., Lidar, D.A. (2005). *Phys. Rev. A* **71**, 022302.
Fischer, M.C., Gutiérrez-Medina, B., Raizen, M.G. (2001). *Phys. Rev. Lett.* **87**, 040402.
Fougères, A., Noh, J.W., Grayson, T.P., Mandel, L. (1994a). *Phys. Rev. A* **49**, 530.
Fougères, A., Torgerson, J.R., Mandel, L. (1994b). *Opt. Comm.* **105**, 199.
Ghose, P., Horne, D., Agarwal, G.S. (1992). *Phys. Lett. A* **168**, 95.
Giulini, D., et al. (1996). *Decoherence and the Appearance of a Classical World in Quantum Theory*. Springer, Berlin.
Goldberger, M.L., Seitz, F. (1947). *Phys. Rev.* **71**, 294.
Golub, R., Gähler, R., Keller, T. (1994). *Am. J. Phys.* **62**, 779.
Hafner, M., Summhammer, J. (1997). *Phys. Lett. A* **235**, 563.
Heitler, W. (1954). *The Quantum Theory of Radiation*, 3rd ed. Oxford University Press, Oxford.
Helstrom, C.W. (1976). *Quantum Detection and Estimation Theory*. Academic Press, New York.
Holland, M.J., Burnett, K. (1993). *Phys. Rev. Lett.* **71**, 1355.
Home, D., Whitaker, M.A.B. (1997). *Ann. Phys.* **258**, 237.
Hradil, Z., et al. (1996). *Phys. Rev. Lett.* **76**, 4295.
Hradil, Z. (1997). *Phys. Rev. A* **55**, 1561(R).
Hradil, Z., Summhammer, J., Badurek, G., Rauch, H. (2000). *Phys. Rev. A* **62**, 014101.
Inagaki, S., Namiki, M., Tajiri, T. (1992). *Phys. Lett. A* **166**, 5.
Ioffe, A., Vrana, M. (2002). *Appl. Phys. A* **74**, 314.
Itano, W.H., Heinzen, D.J., Bollinger, J.J., Wineland, D.J. (1990). *Phys. Rev. A* **41**, 2295.
Itano, W.H., Heinzen, D.J., Bollinger, J.J., Wineland, D.J. (1991). *Phys. Rev. A* **43**, 5168.

Jackiw, R. (1968). *J. Math. Phys.* **9**, 339.
Jacobson, D.L., Werner, S.A., Rauch, H. (1994). *Phys. Rev. A* **49**, 3196.
Jakob, M., Bergou, J.A. (2003). arXiv:quant-ph/0302075.
Janicke, U., Wilkens, M. (1995). *J. Mod. Optics* **42**, 2183.
Jericha, E., Schwab, D.E., Jäkel, M.R., Carlile, C.J., Rauch, H. (2000). *Physica B* **283**, 414.
Jones, K.R.W. (1991). *Annals of Phys.* **207**, 140.
Kaiser, H., Clothier, R., Werner, S.A., Rauch, H., Wölwitsch, H. (1992). *Phys. Rev. A* **45**, 31.
Kak, A.C., Slaney, M. (1987). *Principles of Computerized Tomographic Imaging*. Ed. by R.F. Cotellessa. IEEE Press.
Kendall, M.G., Stuart, A. (1961). *Advanced Theory of Statistics, vol 2*. Charles Griffin, London.
Koerner, S., Schillinger, B., Vontobel, P., Rauch, H. (2001). *Nucl. Instrum. Meth. A* **471**, 69.
Kofman, A.G., Kurizki, G. (2000). *Nature* **405**, 546.
Kono, N., Machida, K., Namiki, M., Pascazio, S. (1996). *Phys. Rev.* **54**, 1064.
Koshino, K., Shimizu, A. (2003). *Phys. Rev. A* **67**, 042101.
Krenn, G., Summhammer, J., Svozil, K. (2000). *Phys. Rev. A* **61**, 052102.
Kurtsiefer, Ch., Pfau, T., Mlynek, J. (1997). *Nature* **386**, 150.
Kwiat, P., Weinfurter, H., Herzog, T., Zeilinger, A., Kasevich, M. (1995). *Phys. Rev. Lett.* **74**, 4763.
Lane, A.M. (1983). *Phys. Lett. A* **99**, 359.
Lane, A.S., Braunstein, S.L., Caves, C.M. (1993). *Phys. Rev. A* **47**, 1667.
Loudon, R. (1973). *The Quantum Theory of Light*. Clarendon, Oxford.
Luis, A., Peřina, J. (1996). *Phys. Rev. Lett.* **76**, 4340.
Luis, A., Sánchez-Soto, L.L. (1998). *Phys. Rev. A* **57**, 781.
Luis, A., Sánchez-Soto, L.L. (2000). In: Wolf, E. (Ed.), *Progress in Optics*, vol. 41. Elsevier, Amsterdam.
Lukš, A., Peřinová, V. (1994). *Quant. Opt.* **6**, 125.
Lynch, R. (1995). *Phys. Reports* **256**, 368.
Maaß, P., Treimer, W., Feye-Treimer, U. (1992). *Impact of Computing in Science and Engineering* **4**, 250.
Mair, B.A., Rao, M., Anderson, J.M.M. (1996). *Inverse Problems* **12**, 965.
Manfredi, G., Feix, M.R. (2000). *Phys. Rev. E* **62**, 4665.
Mariano, A., Facchi, P., Pascazio, S. (2001). *Fortschr. Phys.* **49**, 1033.
Massar, S., Mitchison, G., Pironio, S. (2002). *Phys. Rev. A* **65**, 022110.
McMahon, P.J., Allman, B.E., Nugent, K.A., Jacobson, D.L., Arif, M., Werner, S.A. (2001). *Appl. Phys. Lett.* **78**, 1011.
Mezei, F. (1988). *Physica B* **151**, 74.
Misra, B., Sudarshan, E.C.G. (1977). *J. Math. Phys.* **18**, 756.
Mitchinson, G., Massar, S. (2001). *Phys. Rev. A* **63**, 032105.

Mizobuchi, Y., Ohtaké, Y. (1992). *Phys. Lett. A* **168**, 1.
Momose, A. (1995). *Nucl. Instr. and Methods A* **352**, 622.
Momose, A., Takeda, T., Itai, Y., Hirano, K. (1996). *Nature Med.* **2**, 473.
Nagels, B., Hermans, L.J.F., Chapovsky, P.L. (1997). *Phys. Rev. Lett.* **79**, 3097.
For a review, see Nakazato, H., Namiki, M., Pascazio, S. (1996). *Int. J. Mod. Phys. B* **10**, 247.
Namiki, M., Pascazio, S. (1990). *Phys. Lett. A* **147**, 430.
Namiki, M., Pascazio, S. (1991). *Phys. Rev. A* **44**, 39.
Namiki, M., Pascazio, S., Nakazato, H. (1997). *Decoherence and Quantum Measurements*. World Scientific, Singapore.
Nieto, M.M. (1993). *Phys. Scr. T* **48**, 5.
Noh, J.W., Fougères, A., Mandel, L. (1991). *Phys. Rev. Lett.* **67**, 1426.
Noh, J.W., Fougères, A., Mandel, L. (1992a). *Phys. Rev. A* **45**, 424.
Noh, J.W., Fougères, A., Mandel, L. (1992b). *Phys. Rev. A* **46**, 2840.
Noh, J.W., Fougères, A., Mandel, L. (1993). *Phys. Rev. Lett.* **71**, 2579.
Paris, M., Řeháček, J. (Eds.) (2004). *Quantum State Estimation. Lecture Notes in Physics*, vol. 649. Springer, Berlin.
Pascazio, S., Namiki, M. (1994). *Phys. Rev. A* **50**, 4582.
Pascazio, S., Namiki, M., Badurek, G., Rauch, H. (1993). *Phys. Lett. A* **179**, 155.
Pegg, D.T., Barnett, S.M. (1989). *Phys. Rev. A* **39**, 1665.
Peres, A. (1980). *Am. J. Phys.* **48**, 931.
Peres, A., Ron, A. (1990). *Phys. Rev. A* **42**, 5720.
Peřinová, V., Lukš, A., Peřina, J. (1998). *Phase in Optics*. World Scientific, Singapore.
Petraschek, D., Rauch, H. (1976). Grundlagen für ein Laue-Neutroneninterferometer, Teil 2: Theorie des Interferometers, AIAU 76401.
Petrosky, T., Tasaki, S., Prigogine, I. (1990). *Phys. Lett. A* **151**, 109.
Petrosky, T., Tasaki, S., Prigogine, I. (1991). *Physica A* **170**, 306.
Quabis, S., Dorn, R., Eberler, M., Glöckl, O., Leuchs, G. (2001). *Appl. Phys. B* **72**, 109.
Rauch, H. (2001). *Physica B* **297**, 299.
Rauch, H. (2004). *Physik Journal* **3**, 39.
Rauch, H., Petraschek, D. (1976). Grundlagen für ein Laue-Neutroneninterferometer, Teil 1: Dynamische Beugung, AIAU 74405b.
Rauch, H., Petraschek, D. (1978). In: Dachs, H. (Ed.), *Neutron Diffraction*, *Top. Curr. Phys.*, vol. 6. Springer, Berlin, p. 303.
Rauch, H., Suda, M. (1995). *J. Appl. Phys. B* **60**, 181.
Rauch, H., Suda, M. (1997). *Physica B* **241**, 157.
Rauch, H., Werner, S.A. (2000a). *Neutron Interferometry*. Oxford University Press, Oxford.

Rauch, H., Werner, S.A. (2000b). *Neutron Interferometry: Lessons in Experimental Quantum Mechanics*. Oxford University Press, Oxford.
Rauch, H., Treimer, W., Bonse, U. (1974). *Phys. Lett. A* **47**, 369.
Rauch, H., Summhammer, J., Zawisky, M., Jericha, E. (1990). *Phys. Rev. A* **42**, 3726.
Rauch, H., et al. (1996). *Phys. Rev. A* **53**, 902.
Rauch, H., Suda, M., Pascazio, S. (1999). *Physica B* **268**, 277.
Řeháček, J., Hradil, Z., Zawisky, M., Pascazio, S., Rauch, H., Peřina, J. (1999). *Phys. Rev. A* **60**, 473.
Řeháček, J., Peřina, J., Facchi, P., Pascazio, S., Mišta, L. (2000a). *Phys. Rev. A* **62**, 013804.
Řeháček, J., et al. (2000b). *Phys. Rev. A* **62**, 013804.
Řeháček, J., Hradil, Z., Dušek, M., Haderka, O., Hendrych, M. (2000c). *J. Opt. B: Quantum Semiclass. Opt.* **2**, 237.
Řeháček, J., Hradil, Z., Ježek, M. (2001). *Phys. Rev. A* **63**, 040303(R).
Řeháček, J., Hradil, Z., Zawisky, M., Treimer, W., Strobl, M. (2002). *Europhys. Lett.* **59**, 694.
Řeháček, J., Hradil, Z., Haderka, O., Peřina, J. Jr., Hamar, M. (2003). *Phys. Rev. A* **67**, 061801.
Renninger, M. (1960). *Z. Phys.* **158**, 417.
Royer, A. (1996). *Phys. Rev. A* **53**, 70.
Sanders, B.C., Milburn, G.J. (1995). *Phys. Rev. Lett.* **75**, 2944.
Schieve, W.C., Horwitz, L.P., Levitan, J. (1989). *Phys. Lett. A* **136**, 264.
Schillinger, B., Blümlhuber, W., Fent, A., Wegner, M. (1998). *Nucl. Instr. and Methods A* **424**, 58.
Schillinger, B., Lehmann, E., Vontobel, P. (2000). *Physica B* **276**, 59.
Schulman, L.S. (1998). *Phys. Rev. A* **57**, 1509.
Scully, M.O., Englert, B.-G., Walther, H. (1991). *Nature* **351**, 111.
Sears, V.F. (1989). *Neutron Optics*. Oxford University Press, Oxford.
Sears, V.F. (1992). *Neutron News* **3**, 26.
Shepp, L.A., Vardi, Y. (1982). *IEEE Trans. Med. Imag.* **1**, 113.
Suda, M. (1995). *Quantum Semiclass. Opt.* **7**, 901.
Summhammer, J., Rauch, H., Tuppinger, D. (1987). *Phys. Rev. A* **36**, 4447.
Susskind, L., Glogower, J. (1964). *Physics* **1**, 49.
Thun, K., Peřina, J. (1998). *Phys. Lett. A* **249**, 363.
Toschek, P.E., Wunderlich, C. (2001). *Eur. Phys. J. D* **14**, 387.
Treimer, W., Feye-Treimer, U. (1998). *Physica B* **241**, 1228.
Treimer, W., Maaß, P., Strothmann, H., Feye-Treimer, U. (1991). *Physica B* **17**, 532.
Vardi, Y., Lee, D. (1993). *J. R. Statist. Soc. B* **55**, 569.
Vardi, Y., Shepp, L.A., Kaufman, L. (1985). *Statist. Assoc.* **80**, 8.
Walkup, J.F., Goodman, J.W. (1973). *J. Opt. Soc. Am.* **63**, 399.

Watanabe, S. (1939). *Z. Phys.* **113**, 482.
Wilkinson, S.R., Bharucha, C.F., Fischer, M.C., Madison, K.W., Morrow, P.R., Niu, Q., Sundaram, B., Raizen, M.G. (1997). *Nature* **387**, 575.
Windisch, D., Becker, P. (1990). *Phys. Stat. Sol. A* **118**, 379.
Wunderlich, C., Balzer, C., Toschek, P.E. (2001). *Z. Naturforsch.* **56a**, 160.
Yurke, B., McCall, S.L., Klaude, J.R. (1986). *Phys. Rev. A* **33**, 4033.
Zawisky, M. (2004). *Foundations of Physics Letters* **17**, 561.
Zawisky, M., Rauch, H., Hasegawa, Y. (1994). *Phys. Rev. A* **50**, 5000.
Zawisky, M., et al. (1998). *J. Phys. A: Math. Gen.* **31**, 551.
Zawisky, M., Baron, M., Loidl, R., Rauch, H. (2002). *Nucl. Instr. and Meth. A* **481**, 406.
Zawisky, M., Bonse, U., Dubus, F., Hradil, Z., Rehacek, J. (2004a). *Europhys. Lett.* **68**, 337.
Zawisky, M., Bastürk, M., Řeháček, J., Hradil, Z. (2004b). *J. Nucl. Mater.* **327**, 188.
Zurek, W.H. (1991). *Phys. Today* **44**, 36.

FURTHER READING

Hillery, M., et al. (1984). *Phys. Rep.* **106**, 121.
Wigner, E. (1932). *Phys. Rev.* **40**, 749.